Delft University of Technology

Master's Thesis:

Predicting Wake-Induced Interactions of Tandem Flettner Rotors

Author:
Bora Uğurcan Ekizoğlu
boraugurcanlive.com

Supervisor:
Prof. Gabriel D. Weymouth
Co-supervisor:
Dr. Bernat Font
November 24, 2025

Acknowledgements

I would like to express my heartfelt gratitude to all the people who have supported, encouraged, and believed in me throughout this journey. Completing this thesis has been one of the most challenging and rewarding experiences of my academic life, and it would not have been possible without the presence of many remarkable individuals around me.

First, I would like to sincerely thank my supervisors for their continuous guidance, patience, and expertise. Their thoughtful feedback, constructive discussions, and encouragement helped me grow not only academically but also personally. I am deeply grateful for the trust they placed in me and for the freedom they gave me to explore, learn, and develop my own ideas. Their support made this work possible, and I feel truly fortunate to have had the opportunity to learn from them.

I owe my deepest gratitude to my parents, whose unconditional love and belief in me have carried me through every stage of my life. Their sacrifices, support, and constant reassurance gave me the strength to overcome many difficult moments. Nothing I achieve would be possible without them, and this milestone belongs to them as much as it does to me.

To my friends, thank you for being my source of balance and joy throughout this process. Your encouragement, humor, and companionship helped me especially during the most demanding phases of my thesis. I am lucky to have people who constantly reminded me to take breaks, to keep perspective, and to keep going when things felt overwhelming.

Finally, I would like to extend my appreciation to everyone who, in one way or another, contributed to this work or supported me during my studies. Each of you has played a part in helping me reach this point, and I am truly grateful. Thank you all for being a part of this journey.

Abstract: The growing demand for sustainable marine transportation has revived interest in Flettner rotors as auxiliary wind-assisted propulsion devices capable of significantly reducing fuel consumption and emissions. While the aerodynamic performance of single rotors has been widely studied, the complex wake-induced interactions between multiple rotors remain insufficiently understood, limiting reliable performance prediction for practical installations. This thesis investigates these wake interactions of tandem finite Flettner rotors through high-fidelity computational fluid dynamics (CFD) simulations supported by data-driven reduced-order modeling (ROM). The study begins with a validation campaign against benchmark experimental data from Shehata and Medina (2021) and numerical data from Liu et al. (2025) for rotating cylinders to ensure the reliability of the employed Biot–Savart boundary condition implementation in the WaterLily.jl CFD framework. The validated setup is then extended to perform a systematic parametric study of two interacting rotors by varying spin ratios (λ_1, λ_2) and incidence angle (θ) at a Reynolds number of $Re = 1000$. The simulations reveal distinct wake regimes governed by up-wash and down-wash interactions, demonstrating how the forces on both rotors change with induced interactions. Additionally, the results indicate that asymmetric spin-ratio combinations can locally enhance the aerodynamic efficiency of the system by mitigating wake interference. To analyze the vast three-dimensional flow database efficiently, Proper Orthogonal Decomposition (POD) is employed. The first few POD modes capture the dominant wake structures responsible for the majority of the flow energy, providing physical insight into the coherent vortical features and their parametric dependence. The POD coefficients serve as compact representations of the flow fields and are used to construct a machine-learning based reduced order model. A multi-layer perceptron (MLP) and a Bayesian regression (BR) model is trained to learn the nonlinear mapping between the global parameters $(\lambda_1, \lambda_2, \theta)$ and the corresponding POD coefficients. The resulting models are capable of predicting the time-averaged velocity and pressure fields for unseen parameter combinations with reasonable accuracy and low computational cost. The combined POD-ML framework demonstrates the feasibility of predicting complex wake-interaction behavior using limited high-fidelity data. While the models successfully reproduce dominant flow patterns and aerodynamic trends, their accuracy can be further improved by incorporating additional high Reynolds number data and broader parameter coverage. The thesis concludes that reduced-order modeling based on POD and machine learning provides a promising pathway toward fast, data-driven performance prediction tools for wind-assisted propulsion systems featuring multiple interacting Flettner rotors.

Thesis for the degree of MSc in Marine Technology in the specialization of Ship Hydromechanics

Predicting Wake-Induced Interactions of Tandem Flettner Rotors

By

Bora Uğurcan Ekizoğlu

Performed at

TU Delft

This thesis MT.25/26.013.M is classified as confidential in accordance with the general conditions for projects performed by the TUDelft.

26/11/2025

Company supervisors
Responsible supervisor:
E-mail:
Daily Supervisor(s):
E-mail:

Thesis exam committee
Chair/Responsible Professor: Prof. G.D. (Gabe) Weymouth
Staff Member: Prof. Dr. Ir. T.J.C. (Tom) van Terwisga
Staff Member: Dr. B. (Bernat) Font
Staff Member: Dr.ir. A. F. (Alberto Felipe) Rius Vidales

Author Details
Studynumber: 5955629

Contents

List of Figures

List of Tables

Nomenclature

Symbol	Definition	Unit
A	Singular value weighted POD coefficient matrix	$[-]$
a	Radius	$[m]$
a_1	Singular value weighted POD coefficient	$[-]$
AR	Aspect ratio	$[-]$
AE	Absolute error	$[-]$
BR	Bayesian regression	$[-]$
C	Correlation matrix	$[-]$
C_D	Drag coefficient	$[-]$
$\overline{C}_D$	Time-averaged drag coefficient	$[-]$
C_L	Lift coefficient	$[-]$
$\overline{C}_L$	Time-averaged lift coefficient	$[-]$
$C_{L,rms}$	Root mean square of the lift coefficient fluctuations	$[-]$
C_P	Pressure coefficient	$[-]$
$\overline{C_P}$	Averaged pressure coefficient	$[-]$
$\overline{C}_x$	Time-averaged x-force coefficient	$[-]$
$\overline{C}_y$	Time-averaged y-force coefficient	$[-]$
CFD	Computational fluid dynamics	$[-]$
D	Diameter	$[m]$
D_e	End-plate diameter	$[m]$
D_e/D	End-plate to diameter ratio	$[-]$
d	Dimension	$[-]$
DES	Detached eddy simulation	$[-]$
DMD	Dynamic mode decomposition	$[-]$
DNN	Deep neural network	$[-]$
DNS	Direct numerical simulation	$[-]$
e_k	Energy content of the POD mode	$[-]$
F	Force	$[N]$
F_D	Drag force	$[N]$
F_L	Lift force	$[N]$
FOM	Full order model	$[-]$
iLES	Implicit large eddy simulation	$[-]$
LES	Large eddy simulation	$[-]$
M	Degree of freedom of the simulations	$[-]$
ML	Machine learning	$[-]$
MLP	Multi-layer perceptron	$[-]$
MSE	Mean squared error	$[-]$
N	Number of snapshots	$[-]$
n	Number of revolutions	$[RPM]$
NN	Neural network	$[-]$
$\overline{P}$	Time-averaged pressure	$[Pa]$
P/D	Centre-to-centre pitch ratio	$[-]$
$p(\lambda_1, \lambda_2, \theta)$	Global parameter of the snapshot	$[-]$
POD	Proper orthogonal decomposition	$[-]$
$q(\overline{u}_x, \overline{u}_y, \overline{u}_z, \overline{P})$	Physical quantity of the flow field	$[m/s$ & $Pa]$

Symbol	Definition	Unit
RANS	Reynolds-averaged Navier–Stokes	$[-]$
RDMD	Recursive dynamic mode decomposition	$[-]$
Re	Reynolds number	$[-]$
RMSE	Root mean squared error	$[-]$
ROM	Reduced order model	$[-]$
SVD	Singular value decomposition	$[-]$
U	Velocity	$[m/s]$
U_∞	Incoming flow speed	$[m/s]$
$\overline{u}_x$	Time-averaged streamwise velocity component	$[m/s]$
$\overline{u}_y$	Time-averaged cross-stream velocity component	$[m/s]$
$\overline{u}_z$	Time-averaged spanwise velocity component	$[m/s]$
URANS	Unsteady Reynolds-averaged Navier–Stokes	$[-]$
X	Snapshot matrix	$[-]$
x_i	Snapshot value	$[-]$
A	Singular value weighted POD coefficient matrix	$[-]$
ϵ	Kernel width	$[-]$
η	Aerodynamic efficiency	$[-]$
Γ	Circulation strength	$[m^2/s]$
Λ	Eigenvalue matrix	$[-]$
λ	Spin ratio ($\lambda = n\pi D/60U_\infty$)	$[-]$
λ_i	Eigenvalues	$[-]$
ν	Kinematic viscosity	$[m^2/s]$
Ω	Angular velocity	$[1/s]$
ω	Vorticity	$[1/s]$
$\overline{\omega}$	Time-averaged vorticity	$[1/s]$
$\overline{\omega}_z$	Time-averaged z-vorticity	$[1/s]$
Φ	Spatial POD mode matrix	$[-]$
ϕ_i	Spatial POD mode	$[-]$
Ψ	POD coefficient matrix	$[-]$
ψ_i	POD coefficient	$[-]$
Σ	Singular value matrix	$[-]$
σ_i	Singular value	$[-]$
θ	Angle of incidence	$[deg.]$
π	Pi number	$[-]$
∇	Wetted surface area	$[m^2]$
$\mathcal{L}^{(q)}(\Upsilon)$	Loss function	$[-]$
$\mathcal{T}$	Number of training data-points	$[-]$
$\mathcal{V}$	Number of validation data-points	$[-]$

1 Introduction

Flettner rotors have emerged as a promising technology for wind-assisted marine propulsion, offering significant potential to reduce fuel consumption and greenhouse gas emissions. Flettner rotors have garnered interest as an effective technology for harnessing wind power to generate propulsion in the past and they have been increasingly popular again in recent years for marine applications to cut down fuel consumption and consequently cut down NO_x and CO_2 emissions (Seddiek and Ammar, 2021). Talluri et al. (2018) conclude the implementation of Flettner rotors in commercial vessels may reduce fuel consumption by up to 20% if coupled with with correct route selection. Their practical implementation on commercial vessels typically involves the installation of multiple rotors on a limited deck area, where aerodynamic interactions between the rotors can substantially affect the overall system (Chen et al., 2023). Despite the growing number of vessels employing such systems, the aerodynamic coupling and wake-induced interactions between rotors remain poorly understood and are often oversimplified in performance prediction models. Current analytical and semi-empirical approaches frequently neglect the unsteady nature of the rotor wake or apply simplified correction factors to account for the reduction in apparent wind speed and incidence angle experienced by downstream rotors (Lindstad et al., 2022). These simplifications introduce considerable uncertainty in predicting the actual thrust and power characteristics of multi-rotor configurations and to improve the accuracy and reliability of these predictions, it is essential to gain a deeper understanding of the underlying flow physics governing wake-induced interaction between the rotors on deck (Tillig and Ringsberg, 2020).

Unfortunately, there are not many experimental or numerical studies primarily focusing on wall-mounted finite Flettner rotors. However, the wake fields of wall-mounted static circular and square cylinders as well as wake interactions between tandem wall-mounted static cylinders are thoroughly investigated by both experimental and numerical studies as these geometries can represent a wide range of engineering structures (Li et al., 2024). The wake structures of infinite tandem and standalone rotating or static cylinders as well as the effect of these interactions on the dynamic forces acting on these bodies has been investigated in detail. The numerical studies on tandem rotors are mostly in lower Re range between $Re = 20$ to $Re = 300$, which roughly corresponds to laminar boundary layer characteristics, and for two or three dimensional ($2d$ or $3d$) infinite cylinder geometries Behara et al. (2022). This is mainly due to relatively simpler nature of the flow and the time intensity of higher Re flow simulations. There are also studies investigating the wake structures and flow fields around wall-mounted finite rotating cylinders but they are mainly interested in low aspect ratio (AR) cylinders and the connection between the wake structures and dynamic forces acting on these structures are somewhat left underexplored.

This thesis aims to address this gap through high-fidelity numerical simulations combined with data-driven modeling. By systematically investigating the influence of spin ratio and angle of incidence on the wake structures and aerodynamic forces of tandem Flettner rotors, the study seeks to establish a physically consistent basis for reduced-order modeling. It is important to note that the focus of this work is to develop and validate the methodology for a data driven surrogate model rather than reproducing the exact operating conditions of commercial rotor-assisted propulsion systems. The ultimate objective is to contribute to the development of predictive tools that enable the efficient design and optimization of such systems under realistic operating conditions.

A Proper Orthogonal Decomposition (POD) analysis, which is a widely recognized, powerful data-driven technique for extracting dominant flow features from large datasets, on the time-averaged flow field data generated for a global parameter space will be performed. Building on this analysis, the feasibility of a POD-based reduced-order model (ROM) using machine learning (ML) for efficient prediction of the flow fields and and aerodynamic forces under varying conditions will be explored to to address the following research questions.

- How do the wake structures and aerodynamic forces of finite tandem Flettner rotors vary with changes in angle of incidence (α) and spin ratio (λ)?
- To what extent can Proper Orthogonal Decomposition (POD) applied to the time-averaged flow fields provide an effective and compact representation of the dominant flow features across the global parameter space?
- Can a reduced-order model (ROM) combining POD of the time-averaged flow fields with machine learning (ML) accurately predict the wake interactions and aerodynamic force coefficients for varying global parameters?

1.1 Main parameters

The experiments of Bordogna et al. (2020) investigated the dependency of aerodynamic forces to the rotor spacing, apparent wind angle and Re on each rotor. Parameters were altered systematically and the aerodynamic force coefficients were plotted depending on the change of parameters as well as the velocity field behind the rotors. An attempt to correlate the change of the velocity field between two cases (single rotor and tandem rotors) were made. However, the velocity field contour plots were not provided with high resolution. Note that the Re was defined depending on the cylinder diameter (D) and the incoming flow speed (U_∞) as $Re = U_\infty D/\nu$ where, ν is the kinematic viscosity of the fluid. This definition is widely used in the literature and is also adopted for the present study. Chen et al. (2023) investigated the effect of same parameters as Bordogna et al. (2020) but also included the effect of the end plate diameter (D_e) on the aerodynamic forces acting on both cylinders, however they did not include any correlation between velocity fields and/or wake structures on the aerodynamic forces. Additionally, for both of these experimental studies, the rotation rate was altered but antisymmetric rotation rate cases were not included in the experiment matrix. These recent wind-tunnel experiments on tandem Flettner rotors by Bordogna et al. (2020) and Chen et al. (2023) indicate that the wake interactions between such rotors are highly complex due to the unsteady and turbulent nature of the high Reynolds number ($Re \geq 10^5$) flow in the near wake region of the rotors and highly dependent on the changes in the global parameters defining the flow regime and rotor geometry. However, the extent of the effect the changes in these global parameters on the resulting wake fields and aerodynamic forces are somewhat left underexplored.

The present study aims to fill this gap by parametrically investigating how wake interactions and dynamic forces evolve with changes in the global parameters of the system, and by examining the physical correlations between these resulting wake fields and forces. Specifically, finite tandem Flettner rotors will be addressed. The correlation between the aerodynamic forces and the wake structures created by these rotors will be investigated by parametrically studying the the resulting time-averaged flow fields depending on the change in the global parameters of the system. The selected global parameters are the angle of incidence (θ) and spin ratio

(λ) of each rotor. Additionally, the possibility of increasing the aerodynamic efficiency by inducing asymmetric rotation rate between the rotors will also be included in this study. Here, the spin ratio is defined as the ratio between the inflow velocity and the peripheral velocity of the cylinder ($\lambda = n\pi D/60U_\infty$), where n is the number of revolutions per minute (RPM) of the cylinder. To the author's knowledge, such a parametric study has not been conducted before to correlate the wake interaction and the aerodynamic forces alongside the possibility of increasing the aerodynamic efficiency of the system by introducing asymmetric rotation rates on the cylinders. The latter is inspired by vertical axis wind turbine arrays for which the effect of different layouts, rotation directions and speeds on the aerodynamic efficiency has been investigated thoroughly by means of experiments and simulations and administering different tip velocities proved to be promising for increasing the efficiency of these arrays (Sahebzadeh et al., 2022; Ahmadi-Baloutaki et al., 2016; Parker and Leftwich, 2016; Azadani, 2023; Craig et al., 2016).

Primarily, the relevant conditions and parameters for the present study have to be determined. The most important parameter in that regard is perhaps the Re range that the rotors are expected to experience, as it mainly governs the flow characteristics. Predicting or determining the Re includes determining the apparent wind speed range that is likely to be encountered by a commercial vessel and the dimensions of the Flettner rotors that are likely to be installed on such a vessel. Another important parameter is the spacing between the rotors as the main scope of the study is tandem rotors and the wake-induced interaction is highly dependent on the spacing between these rotors. In order to determine the dimensions of a full scale Flettner rotor, the data from a wide range of sources has been investigated, including previous and current vessels equipped with rotors, companies that produce modular rotors, papers presenting experimental and numerical studies on rotors. Numerical studies are not particularly helpful in that manner as they usually use non-dimensionalized length scales based on the rotor diameter (D). Nevertheless, they are still helpful to understand the non-dimensional parameters such as the aspect ratio (AR), spin ratio (λ) and the ratio between the diameter of the end plate and rotor diameter (D_e/D). The end-plates are generally used on Flettner rotors to counteract the effects of tip vortices and downwash from free ends (Thouault et al., 2012). Chen et al. (2023) state, these end-plates can also increase the lift produced by the rotors while decreasing the drag, thus can increase the aerodynamic efficiency. This behavior is governed by the the D_e/D ratio which makes it imperative to get an idea on the range of this parameter in current application beforehand. They also state that the AR and λ are directly connected to the lift generated by a spinning cylinder and there is an optimum value for these parameters to obtain the best aerodynamic efficiency depending on the Re. Badalamenti and Prince (2008), Bordogna et al. (2020) and Gully et al. (2010) state that the most common value for D_e/D is 2 in maritime industry, because the torque needed to spin the rotor grows rapidly after this value and it counteracts the benefits of the increased aerodynamic efficiency as the power required to spin the rotor increases with the torque needed to spin it.

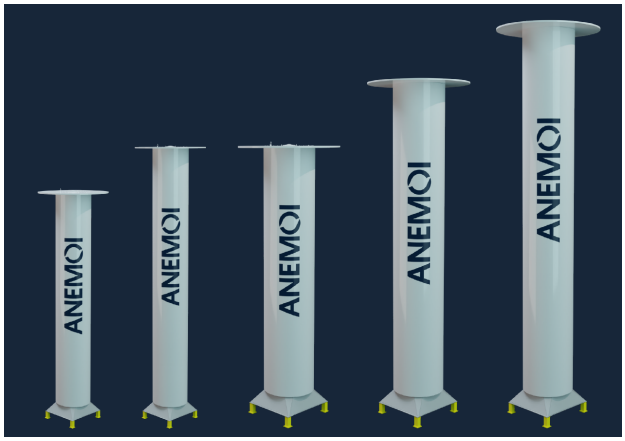

Figure 1: Available modular Anemoi rotors retrieved from product brochure (Anemoi, 2025). Rotor types from left to right: Anemoi 2, Anemoi 3, Anemoi 4, Anemoi 5 and Anemoi 6.

Figure 2: TR Lady equipped with "Anemoi 4" type rotors (Anemoi, nd).

Figure 3: Camellia Dream equipped with "Norsepower 6" type rotors (Norsepower, nd).

Figure 4: Dietrich Oldendorff equipped with "Norsepower 3" type rotors (Norsepower, nd).

The dimensions and/or non-dimensional parameters for each commercial rotor inspected during the literature review are presented in Table 3 and the reference from which the data is obtained is presented in Table 2. The intended operational conditions for the rotors are indicated in Table 4. These tables are color coded to classify how the data in each cell is obtained. If the data in the particular cell is explicitly provided in the corresponding reference, the cell is coded "green". If the data in the cell is obtained through visual observation from available pictures, the cell is coded "blue". If the data in the cell is obtained by secondary means such as calculations using other type of explicit data in the corresponding reference, the cell is coded "purple". If no data could be obtained, the cell is coded "gray". Unfortunately, there is not much direct data on D_e/D ratio therefore, some of the data on D_e/D presented in Table 3 were obtained

through visual observation from available pictures of the particular vessels and/or rotors. Some of the pictures in question are also presented from Figure 1 through Figure 7. Depending on the accumulated data for Flettner rotors currently in use in the maritime industry, geometry for the present study is selected to be the same as "Anemoi 6" type rotor presented in Table 3.

Figure 5: M/V Annika Braren equipped with "Eco Flettner 1" type rotors (Eco-Flettner, nd).

Figure 6: M/V Fehn Pollux equipped with "Eco Flettner 1" type rotors (Eco-Flettner, nd).

Figure 7: Enercon ESHIP-1(VesselFinder, nd).

Table 2: References for the presented rotors.

Ship/Rotor Name	Data retrieved from:
Buckau (1924)	HRMM (nd), UoS (nd)
Barbara (1926)	UoS (nd)
E-Ship 1 (2010)	UoS (nd), Talluri et al. (2018)
Anemoi 1	Anemoi (nd)
Anemoi 2	Anemoi (nd)
Anemoi 3	Anemoi (nd)
Anemoi 4	Anemoi (nd)
Anemoi 5	Anemoi (nd)
Anemoi 6	Anemoi (nd)
Norsepower 1	Norsepower (nd)
Norsepower 2	Norsepower (nd)
Norsepower 3	Norsepower (nd)
Norsepower 4	Norsepower (nd)
Norsepower 5	Norsepower (nd)
Norsepower 6	Norsepower (nd)
Eco Flettner 1	Eco-Flettner (nd)
Eco Flettner 2	Eco-Flettner (nd)
Eco Flettner 3	Eco-Flettner (nd)

After determining the dimensions of the rotors, the next step in determining a realistic Re range is to determine the possible wind speeds and the ambient temperatures that similar Flettner rotors to the ones presented in Table 3 are expected to experience in operation. Case studies are mainly considered for the initial guess as they generally focus on the weather conditions of the shipping route that the vessel in question will sail. These studies are using the raw data from annual global wind and temperature measurements for the inspected shipping route to predict the weather conditions that are likely to be encountered by the vessel. There are two main approaches for this, one is to use some kind of probability density distribution such as Rayleigh or Weibull distribution and obtain a most probable mean value by weighing different wind speed ranges on the shipping route over a certain time period (Kuroda and Sugimoto, 2022; Lindstad et al., 2022; Mason et al., 2023). Other approach is to use the annual or monthly averaged wind speed data without using any type of weighing (Alkhaledi et al., 2023). The approach to determine a wind speed and ambient temperature range for the present study is to use an averaged value. For this purpose, the range presented for two different routes by Alkhaledi et al. (2023) is used as the data is presented with contour plots in most of the online databases for global winds and the numerical values are not explicitly made available for the public. Additionally, most of the databases present wind speed and direction data in a similar way and they wary only in terms of the measurement techniques and the density of the presented data, which is not particularly important as the main focus for the present study does not encompass determining highly realistic wind speed values for different operational scenarios. Somewhat representative values would suffice to determine a realistic Re range. This, the wind speed (V) range is selected based on the average value between the upper and lower bounds of the best fitting Beaufort wind scales to the average wind speed data in Table 6 resulting in a wind speed range between 10-19 m/s (MetOffice, nd).

Having an idea on the ambient temperature is essential as it governs the change in kinematic viscosity of the air, however small changes in the ambient temperature are not highly important as the change in kinematic viscosity is relatively small for small changes in temperature (Cengel and Cimbala, 2013). Consequently, a constant value for kinematic viscosity corresponding to a constant ambient temperature is adopted. Alkhaledi et al. (2023) state that the maximum

temperatures for Marseille-Algeria and Tangier-Southampton routes in the winter season were less than $15°C$ and $21°C$ respectively. $15°C$ was chosen as it is roughly representative for the mean temperatures in winter conditions. In Cengel and Cimbala (2013), the kinematic viscosity (ν) of air is given to be $1.470 \times 10^{-5} m^2/s$ at $15°C$.

Table 3: Parameters of present Flettner rotors in commercial use or in literature. Color code: (Green) explicitly provided data; (Blue) observed data; (Purple) calculated data; (Gray) no data.

Ship/Rotor Name	Height $[m]$	Diameter (D) $[m]$	Speed [RPM]	End plate diameter $(D_e)[m]$	D_e/D	AR
Buckau (1924)	15	3	135	3.9	1.3	5
Barbara (1926)	17	4	150	5.2	1.3	4.25
E-Ship 1 (2010)	27	4	-	8	2	6.75
Anemoi 1	16	2	-	3	1.5	8
Anemoi 2	21	3.5	-	7	2	6
Anemoi 3	24.5	3.5	-	7	2	7
Anemoi 4	24	5	185	10	2	4.8
Anemoi 5	30	5	-	10	2	6
Anemoi 6	35	5	-	10	2	7
Norsepower 1	18	4	225	6	1.5	4.5
Norsepower 2	20	4	225	8	2	5
Norsepower 3	24	4	225	6	1.5	6
Norsepower 4	28	4	225	6	1.5	7
Norsepower 5	30	5	180	7.5	1.5	6
Norsepower 6	35	5	180	7.5	1.5	7
Eco Flettner 1	18	3	280	6	2	6
Eco Flettner 2	24	4	210	8	2	6
Eco Flettner 3	31	5	165	10	2	6.2

Table 4: Operational conditions of present Flettner rotors in commercial use or in literature. Color code: (Green) explicitly provided data; (Blue) observed data; (Purple) calculated data; (Gray) no data.

Ship/Rotor Name	Max continuous thrust $[kN]$	Operational wind speed $[m/s]$	Survival wind speed $[m/s]$
Buckau (1924)	-	-	-
Barbara (1926)	-	-	-
E-Ship 1 (2010)	-	-	-
Anemoi 1	-	-	-
Anemoi 2	-	-	-
Anemoi 3	-	-	-
Anemoi 4	-	-	-
Anemoi 5	-	-	-
Anemoi 6	-	-	-
Norsepower 1	175	0 - 35	70
Norsepower 2	-	-	-
Norsepower 3	175	0 - 35	70
Norsepower 4	205	0 - 35	70
Norsepower 5	300	0 - 35	70
Norsepower 6	350	0 - 35	70
Eco Flettner 1	78	0 - 30	50
Eco Flettner 2	139	0 - 30	50
Eco Flettner 3	147	0 - 30	50

Table 5: Re range for the rotors presented in Table 3.

Diameter (D) $[m]$	Wind speed (V) $[m/s]$	Re
2	10	1.36E+06
2	12.5	1.70E+06
2	15.5	2.11E+06
2	19	2.59E+06
3	10	2.04E+06
3	12.5	2.55E+06
3	15.5	3.16E+06
3	19	3.88E+06
3.5	10	2.38E+06
3.5	12.5	2.98E+06
3.5	15.5	3.69E+06
3.5	19	4.52E+06
4	10	2.72E+06
4	12.5	3.40E+06
4	15.5	4.22E+06
4	19	5.17E+06
5	10	3.40E+06
5	12.5	4.25E+06
5	15.5	5.27E+06
5	19	6.46E+06

A Re range is calculated using the diameter range of the rotors presented in Table 3 and the wind speed (V) and the kinematic viscosity (ν) assumptions. The calculated Re range is presented in Table 5, which suggests a realistic Re range for the real scale Flettner rotors would be between $10^6 - 10^7$. Note that the wind speed is assumed to be However, depending on the limitations and the scope of the present study, the Re range is selected to be more moderate. Detailed discussion on the motivation behind the adopted Re range is provided in Section 2.2. Note that the estimated wind speeds are assumed to be equal to the apparent wind speed and the vessel speed is not considered in the calculated Re range since the scope of the study does not include reproducing realistic operating conditions for Flettner rotors.

Table 6: The mean wind speed in three different seasons for the voyages of Marseille - Algeria and Tangier - Southampton obtained from (COGOW) database Alkhaledi et al. (2023).

Navigation routes	Season	Mean wind speed $[knots]$	Mean wind speed $[m/s]$
Marseille-Algeria	Mid-season	14	7.202
	Summer	10.3	5.298
	Winter	17.5	9.002
Tangier-Southampton	Mid-season	15	7.716
	Summer	14	7.202
	Winter	17	8.745

The spacing between the rotors are mainly dependent on the restrictions imposed by the deck layout of the vessel that the rotors will be installed on (Kume et al., 2022), (Chen et al., 2023). Since the deck layout for each vessel changes significantly, it is hard to determine a certain range for the spacing between the rotors. However, Chen et al. (2023) stated that for most practical applications the centre to centre spacing between the rotors, which is non-dimensionalized by the the diameter of the rotor (P/D) throughout this study, is generally between 4-10 and they investigated a range of P/D between 5-10. Bordogna et al. (2020) has investigated a similar P/D range between 3-15. Kume et al. (2022) has conducted wind tunnel

experiments and computational fluid dynamics (CFD) study on a model ship with rotors. They used five rotor models where the P/D ranged approximately between 9.5-11 where, they used deck layout and the recommendations from the manufacturer of the vessel they investigate to determine the position of each rotor. Considering that the research questions laid out in Section 1 mainly concern the wake-induced interactions between the rotors and that these interactions are expected to be higher for closer P/D as also stated by Chen et al. (2023), a value closer to the lower range investigated by the studies summarized in this paragraph is adopted. This choice is also somewhat consistent with ships installed with closer spaced Flettner rotors as the ships in Figures 2, 4 & 7. Thus, the selected P/D for the present study is 3.

2 Literature Review

The purpose of this literature review is to situate the present study within the broader context of research on Flettner rotors, rotating bluff-body aerodynamics, wake interactions, and reduced-order modeling techniques. Although the use of Flettner rotors in marine propulsion has gained renewed attention, detailed investigations of wake-induced interaction effects, particularly for finite, tandem configurations remain limited. This section therefore synthesizes the existing experimental and numerical studies on rotating cylinders, tandem-body wake dynamics, and data-driven order reduction and flow field prediction methods such as Proper Orthogonal Decomposition (POD) and machine learning (ML). By outlining the current state of knowledge and identifying the gaps most relevant to rotor wake interactions, the review provides the foundation and motivation for the methodology adopted in this thesis.

2.1 Possible dataset generation methods

The fundamental flows around a standalone cylinder and multiple cylinders are divided into two main categories in this study as experimental and numerical studies. These two main categories are then inspected in three categories as finite cylinders, infinite cylinders and Flettner rotors. The difference between studies on finite and infinite cylinders is that the latter model a cylinder throughout the whole span-wise direction, while the former model a finite or a wall-mounted finite cylinder that does not cover the whole computational domain or test section. The studies on Flettner rotors are considered as a special category where these studies implement a wall mounted finite cylinder in the computational domain or in the experiment chamber with end-plates. Note that for each of these categories both rotating and static, as well as standalone and tandem cases are investigated.

The general parameters for the experimental studies considered in this literature review are listed in Table 7. The type of the study is also specified in the same table according to the categorization explained in the previous paragraph. The experimental studies cover a wide range of geometries for a wide range of Re numbers except tandem rotating finite cylinders case. There is also a lack of data in the lower Re range that the present study is interested which is between $500 - 3900$. This is mainly due to the low incoming flow speeds needed to be achieved either in wind or water tunnel test sections for these low Re numbers depending on the geometric scale implemented. There is also a similar problem for higher Re flows due to the limitations of flow speeds and ambient pressures that can be achieved in wind tunnel test sections (Roshko, 1961).

Specifically, experimental studies concerning tandem flettner rotors or tandem rotating cylinders are quite few, furthermore the results from these experiments are not sufficient for conducting the intended parametric POD study. The objective of the parametric POD is to extract the dominant structures from the flow field data to analyze how these structures depend on the global parameters and how do they effect the aerodynamic forces on the rotors. The time-averaged flow field data of the fully developed flow around the rotors will be investigated for this purpose. The POD algorithm typically requires the flow field data to to be arranged in a certain type in a spatially discretized manner with exact numerical values (Shehata and Medina, 2022). To that regard, a systematic sweep is needed for the determined global parameters and the time-averaged flow field data has to be obtained for each parameter change. Furthermore, the possibility of coupling the decomposed flow field data from the POD analysis with a machine learning (ML) algorithm to predict the resulting flow field and aerodynamic forces for the global parameters outside the dataset will be investigated. Such a machine learning algorithm requires relatively large amount of high quality flow field data. Experimental studies present relatively poor results for the averaged flow field measurements depending on the methods and the instrument type used in the experiments. The resolution of the measurements are not as high as the resolution that can be achieved with CFD, and there can be missing spots in the flow field due to the shadow region created by the presence of the body depending on the measurement technique (Aksoy et al., 2024). Such data is not sufficient for both parametric POD and machine learning. Additionally, to the author's knowledge, there is no readily available data generated from experiments which covers a parametric sweep of the global parameters that will be investigated in this study. There is also no experimental study investigating the effect of different rotation rates on the wake-induced interactions of tandem rotors. Thus, it is decided to generate the training dataset by means of numerical simulations.

One upside of the experimental studies is that they produce accurate results for the dynamic forces and pressures on the body as well as the time averaged velocities behind the body on $2d$ slices in the $3d$ experimental domain. This high quality data can be used to validate the numerical results obtained from the simulations. For the sake of brevity, the experiments presented in Table 7 are not discussed thoroughly in this section. However, the experiments of Shehata and Medina (2021) and Shehata and Medina (2022) are discussed in Section 3.1 as they will be utilized for validation purposes.

The general parameters for the numerical studies considered in this literature review are listed in Table 8. Considering the lack of available data from both numerical and experimental studies on tandem Flettner rotors/rotating cylinders in literature, there is a need to generate a sufficient dataset to parametrically investigate the wake-induced interactions. This task requires high number of simulations depending on the number of parameters, the required size of the dataset to obtain a converged POD analysis and a sufficient training set for the ML algorithm. The implemented method for generating such data needs to be both fast and accurate as the quality of the results of the POD and ML algorithm depends on both the size and the quality of the dataset. For the sake of brevity, not all numerical studies presented in Table 8 are explained in this section. However, these studies are generally utilized to understand the ability of the available numerical methods in terms of their convenience for the task of generating a dataset for the present study.

Table 7: Main parameters from experimental studies. Color code: (Green) explicitly provided data; (Blue) observed data; (Purple) calculated data; (Gray) no data.

	Type of study	AR	λ	Centre to centre pitch ratio (P/D)	Re	Angle of incidence (θ)
(Norberg, 1994)	Static cylinders (infinite)	53 - 480	-	-	50 - 4E+04	0
(Prasad and Williamson, 1997)		40 - 80	-	-	350 - 3E+03	0
(Wei and Smith, 1986)		14.726 - 33.858	-	-	1.2E+03 - 1.1E+04	0
(Kourta et al., 1987)		13	-	-	2E+3 - 6E+4	0
(Lin et al., 1995)		10.9 - 21.9	-	-	1E+03 - 1E+04	0
(Ong and Wallace, 1996)		48.951	-	-	3900	0
(West and Apelt, 1982)		4.0 - 10	-	-	1E+04 - 1E+05	0
(West and Apelt, 1993)		10	-	-	1E+04 - 2.5E+05	0
(Higuchi et al., 1989)		5 - 8	-	-	8E+04 - 2E+05	0
(Cantwell and Coles, 1983)		29.29	-	-	1.4E+05	0
(Roshko, 1961)		5.63	-	-	1E+06 - 1E+07	0
(Dargahi, 1989)	Static cylinders (finite)	3.34	-	-	8.4E+03 - 4.6E+4	0
(Park and Lee, 2000)		6 - 17.3	-	-	2E+04	0
(Rostamy et al., 2012)		3 - 9	-	-	4.2E+04	0
(Sumner et al., 2015)		3 - 9	-	-	4.2E+04	0
(Fox and West, 1993)		4 - 30	-	-	4.4E+04	0
(Adaramola et al., 2006)		3 - 9	-	-	6E+04	0
(Sumner et al., 2004)		3 - 9	-	-	6E+04	0
(Xu and Zhou, 2004)	Tandem static cylinders (infinite)	40	-	1 - 1.15	800 - 4.2E+04	0
(Alam, 2014)		24.49	-	1.1 - 4.5	9.7E+03 - 6.5E+04	0
(Li and Sumner, 2009)		9	-	1.125 - 5	2.4E+04	0 - 90
(Maryami et al., 2022)		20.91	-	1.2 - 6	3E+04	0
(Tsutsui, 2012)		1.5	-	1.2	3.8E+04 - 1.3E+05	0
(Alam et al., 2003a)		6.122	-	0.1 - 1.2	5.5E+04	90
(Alam and Meyer, 2011)		6.122	-	0.1 - 5	5.52E+04	0 - 180
(Alam et al., 2003b)		8.163	-	0.1 - 8	6.5E+04	0
(Zhang and Melbourne, 1992)		8	-	1.25 - 10	1.1E+05	0
(Schewe and Jacobs, 2019)		-	-	1.56	2E+05 - 6E+06	0 - 20
(Woyciekoski et al., 2020)	Tandem static cylinders (finite)	3 - 4		1.26	2E+03 - 4.81E+03	90
(Li and Sumner, 2009)		9		1.125 - 5	2.4E+04	0
(Luo et al., 1996)		4 - 8		1.64 - 5	3.33E+04	0
(Dol et al., 2008)	Rotating cylinder (infinite)	18.8	0 - 2.7	-	2E+03 - 9E+03	0
(Aksoy et al., 2024)		12	0 - 1.57	-	2.5E+03 - 1E+04	0
(Lam, 2009)		11.549	0 - 2.5	-	3.6E+3 - 5E+3	0
(Diaz et al., 1983)		>50	0 - 2.5	-	9E+03	0
(Liu et al., 2023)		10	0 - 2	-	4.6E+04 - 2.7E+05	0
(Ma et al., 2022)		10	0 - 2	-	4.6E+04 - 5.10E+05	0
(Shehata and Medina, 2021)	Rotating cylinder (finite)	0.5 - 1	0 - 3	-	1000	0
(Shehata and Medina, 2022)		0.5 - 1	0 - 3	-	1000	0
(Kumar et al., 2011)	Tandem rotating cylinders (infinite)	40	0 - 5	1.8 - 7.5	100 - 500	90
(Kume et al., 2022)	Flettner rotors	7	1.47	9.47 - 13.34	1.86E+04	0
(Chen et al., 2023)		3.5 - 6	0 - 4.5	5 - 10	9.33E+04 - 3.15E+05	0 - 360
(Bordogna et al., 2020)		5	0 - 2	3 - 15	1E+05	15 - 180
(Bordogna et al., 2019)		3.73	0 - 5	-	1.8E+05 - 1E+06	0

Table 8: Main parameters from numerical studies. Color code: (Green) explicitly provided data; (Blue) observed data; (Purple) calculated data; (Gray) no data.

	Type of study	AR	λ	Centre to centre pitch ratio (P/D)	Re	Angle of incidence (θ)
(Ma et al., 2000)	DNS Static cylinder (infinite)	-	-	-	500 - 5000	0
(Dong et al., 2006)		9 - 2	-	-	3900 - 1E+04	0
(Aljure et al., 2017)		2π	-	-	5000	0
(Dong and Karniadakis, 2005)		20	-	-	1E+04	0
(Liu, 2024)	DNS Static cylinder (finite)	4 - 12	-	-	60 - 800	0
(Jester and Kallinderis, 2003)	DNS Tandem static cylinders (infinite)	-	-	1.5 - 3	80 - 1000	0 - 90
(Mittal et al., 1997)		-	-	2.5 - 5.5	100 - 1000	0 - 90
(Padrino and Joseph, 2006)	DNS Rotating cylinder (infinite)	-	3 - 5	-	200 - 1000	0
(Aljure et al., 2015)		2	0 - 5	-	5000	0
(Massaro et al., 2024)	DNS Rotating cylinder (finite)	-	0 - 3	-	3000	0
(Behara et al., 2022)	DNS Tandem rotating cylinders (infinite)	8	0 - 2	2.5 - 7.5	180 - 500	0
(Ma et al., 2000)	LES Static cylinder (infinite)	-	-	-	500 - 5000	0
(Breuer, 1998)		π	-	-	3900	0
(Fan et al., 2024)		π	-	-	3900	0
(Franke and Frank, 2002)		-	-	-	3900	0
(Kravchenko and Moin, 2000)		-	-	-	3900	0
(Prsic et al., 2014)		4	-	-	3900 - 1.31E+04	0
(Jordan and Ragab, 1998)		-	-	-	5600	0
(Breuer, 2000)		1 - π	-	-	1.4E+05	0
(Lehmkuhl et al., 2014)		0.5π	-	-	2.5E+05 - 6.5E+05	0
(Catalano et al., 2003)		-	-	-	5E+5 - 1E+6	0
(Afgan et al., 2007)	LES Static cylinder (finite)	6 -10	-	-	2E+04	0
(Krajnović, 2011)		6	-	-	2E+04	0
(Fröhlich and Rodi, 2004)		2.5	-	-	4.2E+04	0
(Afgan et al., 2011)	LES Tandem static cylinders (infinite)	4	-	1 - 5	3000	90
(Chang et al., 2024)		6.4	-	3	3900	0
(Kitagawa and Ohta, 2008)		1	-	2 - 5	2.2E+04	0
(Wu et al., 2020)		2	-	1.5 - 4	1.4E+05	0 - 90
(Palau-Salvador et al., 2008)	LES Tandem static cylinders (finite)	2.5	-	2	1500	0
(Cheng et al., 2018)	LES Rotating cylinder (infinite)	3	0 - 2	-	5000	0
(Liu et al., 2023)		6.667	0 - 2	-	8.1E+04	0
(Karabelas, 2010)		20	0 - 2	-	1.4E+05	0
(Gopalan and Jaiman, 2015)	DES Tandem static cylinders(infinite)	3	-	1.4 - 3.7	1.66E+05	0
(Uzun and Hussaini, 2012)		6	-	3.7	1.66E+05	0
(Stringer et al., 2014)	RANS Static cylinder (infinite)	-	-	-	40 - 1E+6	0
(Atlar et al., 2010)		-	-	-	4.13E+04	0
(Thouault et al., 2012)	RANS Rotating cylinder (infinite)	1.3 - 5.1	0 - 3.4	-	2.9E+04 - 9.6E+04	0
(Karabelas et al., 2012)		-	2 - 8	-	5E+5 - 5E+6	0

Direct numerical simulations (DNS) offer high fidelity results, but they can be highly time demanding depending on the complexity of the system and the Re. Provided that the Re range in the present study will be in the turbulent flow range and the case for tandem rotating cylinders presents a relatively complex geometry, the time cost of generating a dataset with DNS is expected to be quite high. Massaro et al. (2024) conducted DNS on a wall mounted rotating cylinder and stated that for the dynamic case of a rotating cylinder, the simulation setup is highly complex and the simulation time is relatively high. Thus, DNS is considered to be unfeasible for conducting high number of separate simulations for relatively complex and highly dynamic case of tandem Flettner rotors.

For RANS/URANS approaches, predicting the turbulent characteristics and flow structures in the wake of a bluff body presents a problem, mainly resulting form averaging over the fluctuating components of the velocity and the modeling error resulting from the implemented wall functions and turbulence models. These models can offer significant improvements for the computational cost of the simulations, however they give poor results for the prediction of vortical structures in the wake of high-moderate Re bluff body flows and they are not able to capture the transitions in the boundary layer. Thouault et al. (2012) have conducted numerical end experimental studies on rotating cylinders with end plates and encountered a similar problem regarding the prediction of tip vortices emanated from the end plates. The models implemented in most RANS/URANS studies can be fine tuned to achieve sufficient convergence to the experimental measurements under certain assumptions, but fine tuning of the parameters in these models are highly case sensitive (Karabelas et al., 2012). Atlar et al. (2010) carried out RANS simulations of the flow around a static cylinder at $Re = 41300$ with five different turbulence models and investigated the dependence of the simulations to the implemented turbulence model. The results were highly dependent on the turbulence model and they state that the accuracy of the particular turbulence model is also highly dependent on the specific problem. Karabelas et al. (2012) carried out $2d$ RANS simulations of the flow past a rotating cylinder at Re between $5 \times 10^5 - 5 \times 10^6$. The validation case was conducted for a stationary cylinder at $Re = 1 \times 10^6$ because of the lack of data on rotating cylinders in open literature and shows acceptable correlation with the experimental data for pressure coefficient (C_P) on the cylinder surface (Karabelas et al., 2012). However, the correlation is not good for Reynolds stress which may indicate that the wake field prediction is not particularly accurate. Stringer et al. (2014) have carried out URANS simulations for a wide range of Re from 40 to 10^6. They state the URANS simulations fail to capture the mode transitions and turbulent characteristics of the flow for Re equal to or greater than 10^3. Considering the results of Thouault et al. (2012), Atlar et al. (2010), Karabelas et al. (2012) and Stringer et al. (2014), the RANS/URANS approach is highly dependent on the implemented turbulence model and wall function which makes it case-specific. Additionally, Catalano et al. (2003) indicates that the RANS simulations mainly fails to capture the turbulent characteristics of the flow field which would be highly influential for the wake-induced flow around tandem rotating cylinders. These models can be tailored to fit a specific flow case to give sufficient results, but this approach is not suitable for generating the relatively large dataset needed for the present study since this task requires numerous simulations with varying global parameters (e.g. Re, λ, α.) and RANS/URANS approach is expected to miss the transition of the wake field depending on different global parameters. Thus, RANS/URANS approaches are deemed insufficient for generating the flow field data.

For large eddy simulations (LES), dependency of the accuracy of the prediction of larger scale turbulent structures to the solutions in the near wall region is high as they are directly connected

to the accuracy in resolving the small scale eddies (Kravchenko and Moin, 2000). This effect in the near wake region becomes increasingly pronounced as the distance from the near wake region increases. The LES simulations are also highly dependent on the method implemented for resolving small scale eddies. Catalano et al. (2003) carried out LES with wall modeling for a static cylinder in the super-critical regime. A simple wall stress model was implemented to provide the LES with sufficient boundary conditions. Even though the implemented wall model would highly effect the wake region resolved by LES, a carefully tailored wall model for the specific case provided good quality results. For validation, they presented results for mean pressure distribution on the cylinder and stream-wise and span-wise averaged velocity profiles which achieved sufficient convergence to the experimental case. The rest of the studies listed under "LES static cylinder (infinite)" in Table 8 presented similar results to Catalano et al. (2003) for lower Re, that is closer to the Re range investigated in the present study. The validation cases for Kravchenko and Moin (2000) and Catalano et al. (2003) are given in Figures 9 & 8 respectively in order to present a rough estimate on the capability of LES simulations depending on changing Re. These studies were selected as a means of comparison for simplicity since averaged drag ($\overline{C_D}$) and lift ($\overline{C_L}$) coefficients are both highly dependent on the pressure changes over the surface of the body.

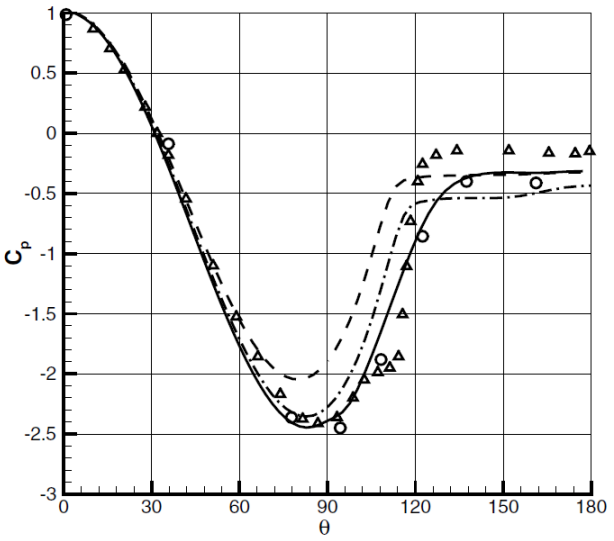

Figure 8: Mean pressure distribution on the cylinder: (−) LES at $Re = 1 \times 10^6$; (− − −) RANS at $Re = 1 \times 10^6$; (− · −) URANS at $Re = 1 \times 10^6$; (∘) experiment by Warschauer and Leene (1971) at $Re = 1.2 \times 10^6$ (spanwise averaged); (Δ) experiment by Falchsbart (in Zdravkovich, 1997) at $Re = 6.7 \times 10^5$ (Catalano et al., 2003).

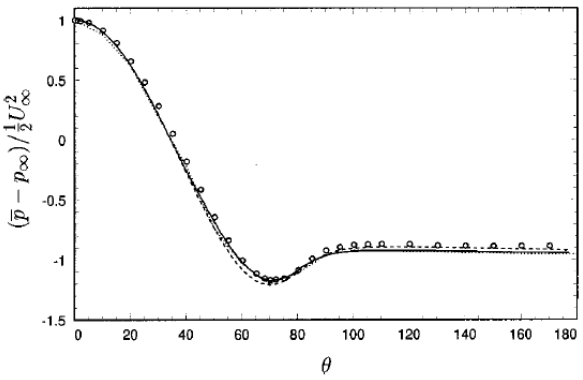

Figure 9: C_P distribution with respect to peripheral angle of the cylinder: (−) B-spline simulations; (− − −) central FD simulations of Mittal and Moin; (· · ·), upwind FD simulations of Beaudan and Moin; (∘) experiment of Norberg (Kravchenko and Moin, 2000).

(Catalano et al., 2003) also included RANS and URANS simulations for the validation case and it is clear from Figure 8 that the LES results converge better to the experimental measurements compared to both RANS and URANS results. Kravchenko and Moin (2000) present results on the Strouhal frequency of the vortex shedding phenomena, which is quite close to the experimental measurements, indicating that the LES simulations hold good potential in capturing the turbulent characteristics of the wake as well as the vortex shedding behavior. This is highly valuable for cases with tandem cylinders as the dynamic forces acting on the cylinder

submerged in the wake of the other will be highly effected by these turbulent flow structures in the wake of the upstream cylinder. Additionally, the wide Re range and the converged results of studies listed under "LES static cylinder" in Table 8 indicate that the LES simulations hold a potential to provide sufficiently accurate results for different Re values which is valuable for generating the dateset since Re is also one of the global parameters in this study. Moreover, Palau-Salvador et al. (2008) show good qualitative validation for LES on finite tandem static cylinders which is the closest geometrical case to the present study. Thus, it is concluded that the data generated from LES simulations will offer sufficient quality in training the ML algorithm.

In detached eddy simulations (DES) the near-wall domain is resolved by a RANS/URANS approach coupled with a wall function and a turbulence model. Then, for the flow region away from the wall, the approach is switched to LES. The possible accuracy problems in the near wall region can induce higher errors when resolving the large scale eddies away from the body. Furthermore, the approach taken for the switch between RANS/URANS can also highly amplify the errors in resolving the large scale eddies the far wake region (Gopalan and Jaiman, 2015). However, Gopalan and Jaiman (2015) also state that the computational cost can be significantly cut down owing to the computationally cheaper RANS/URANS approach at the near wall region compared to wall resolved LES or wall function coupled LES. Gopalan and Jaiman (2015) have carried out DES for tandem static cylinders for $Re = 1.66 \times 10^6$. They state the results for $\overline{C_D}$, root mean square of the lift coefficient ($C_{L,rms}$) and average pressure coefficient ($\overline{C_P}$) on the cylinder surface were poor for the downstream cylinder. They also present contour plots for the flow field between the two cylinders including velocity fields and turbulence properties, and compare these results to measurements from experiments. Even though the flow field results seem reasonable for the flow field in between the cylinders, there are some discrepancies especially in predicting the length of the wake of the upstream cylinder. There are no contour plots presented for the wake region behind the downstream cylinder, however the errors in the validation case for downstream cylinder indicate that this wake field is poorly predicted. The results of Gopalan and Jaiman (2015) suggest that DES would give even poorer approximations for rotating cylinders since the problem in predicting the wake field mainly originates from the poor near-wall region results from RANS/URANS approach. Thus, DES approach is deemed insufficient for the present study in terms of data quality even though it is expected to perform good in terms of reducing the time cost of the simulations.

2.2 Flow solver and Re range

The choice for the considered Re range in the present study is intertwined with the Re range investigated in previous experiments for Flettner rotors and wall mounted finite bluff bodies and the time cost of the simulations as well as the method and the solver implemented for the simulations. As shown in Table 7, the Re range investigated by the experiments for Flettner rotors and wall mounted finite bluff bodies are generally in the higher Re range which is closer to the realistic prediction presented in Section 1.1. Thus, a Re of 10^3 is adopted to investigate the interactions between the rotors in lower incoming wind speeds to contribute to the lack of data in the moderate Re range from the previous studies.

In Section 2.1, LES was selected as the computational method to generate the dataset, however package programs employing classical boundary conditions and body fitted spatial discretization techniques are still highly expensive in terms of pre-processing time. Considering that

the angle of incidence is also one of the selected global parameters, the domain size and the mesh divergence should be adjusted depending on the wake deflection from the rotors for different incidence angles. Either, each computational domain have to be in the same size as the case with the highest wake deflection, which considerably increases the computational time for dataset generation, or each domain has to be specifically tailored for each simulation. However, POD analysis requires each simulation in the dataset to have the same number of grid points and changing the domain size for each case and/or having a sufficiently large domain for each simulation and adjusting the mesh geometry the grid divergence accordingly for different inflow angles while keeping the same number of grid points across each domain is virtually impossible. Thus, a domain employing a uniform mesh will have to be used. Considering the amount of data needed and the required domain size for classical boundary conditions, this presents a bottleneck for the current project and facilitates the motivation behind selection of WaterLily.jl as the fluid solver (Weymouth and Font, 2025). WaterLily.jl employs an immersed boundary method, an implicit Large Eddy Simulation (iLES) approach, a uniform Cartesian Eulerian mesh and presents the possibility of employing Biot-Savart boundary conditions. These methods enable significant savings in pre-processing and in simulation time by allowing a much smaller domain size through the use of Biot-Savart boundary conditions compared to package programs employing classical boundary conditions and body-fitted meshes. The iLES approach further enhances efficiency by bypassing explicit subgrid-scale modeling while still capturing turbulence effects. Additionally, the uniform Cartesian grid structure allows for optimized GPU acceleration, resulting in a significant speed-up of up to 200 times compared to traditional CPU solvers, making WaterLily.jl highly suitable for the generation of the dataset for the present study allowing every simulation in the dataset to have the same size and arrangement resulting in a simpler pre-processing for POD and ML. However, the uniform Cartesian Eulerian mesh employed by WaterLily.jl presents a limitation on the maximum Re for the simulations which partially influences the choice for the lower Re of 10^3.

It is important to emphasize that the aim of the present work is not to reproduce full-scale Flettner rotor operating conditions, but to develop and validate a methodology for parametrically analyzing wake interactions, resultant forces and constructing a POD-ML based reduced-order model (ROM) framework. In this context, selection of a moderate Reynolds number does not limit the relevance of the approach. While the detailed flow features will inevitably differ at higher Re, the methodology for data generation, POD decomposition, and surrogate modeling, remains fully applicable. Therefore, the choice of $Re = 10^3$ should be understood as a pragmatic decision that enables efficient development and demonstration of the methodology, rather than as a constraint on its applicability to full-scale Flettner rotors.

2.3 Global parameter range

Although the present study employs a lower Re number than that of full-scale Flettner rotors, the selected ranges for the spin ratio (λ) and angle of incidence (θ) are chosen to remain representative of realistic operational conditions as well as to ensure high wake interaction between the rotors. Full-scale rotor systems typically operate within comparable ranges of λ and experience similar variations in apparent wind angle, meaning that the underlying aerodynamic mechanisms such as wake deflection, interaction strength, and lift asymmetry remain qualitatively consistent. Therefore, even though the Re is reduced for computational feasibility, the chosen parameter ranges preserve the physical relevance of the problem to some degree.

A range of spin ratios $\lambda_1, \lambda_2 \in [3, 4, 5]$, and incidence angles $\theta \in [0°, 15°, 30°]$ is selected for global parameter space. These ranges are well within the typical operating conditions of the rotors as stated by Kume et al. (2022) and Bordogna et al. (2019). Furthermore, this parameter range is also consistent with the data obtained for commercial rotors presented in Table 4.

2.4 Parametric proper orthogonal decomposition (POD)

POD is a mathematical technique widely used for extracting dominant modes or patterns from complex datasets. It is commonly applied in fluid dynamics, structural mechanics, and machine learning for dimensionality reduction and feature extraction. POD works by decomposing a set of correlated data (e.g., velocity fields, pressure distributions) into a set of orthogonal basis functions (modes) that best captures the energy of the system. The decomposition is typically performed using singular value decomposition (SVD) or eigenvalue decomposition of the correlation matrix (Taira et al., 2017). In the context of marine hydromechanics and CFD, POD is often used to identify dominant flow structures, reduce computational complexity in simulations, and develop reduced-order models (ROMs) (Taira et al., 2020). POD modes can be correlated to physical phenomena governing the flow and is able to reconstruct the flow data with most of it's modes truncated as the total energy in the flow field can be captured by the first few modes. This makes POD analysis highly advantageous for both analyzing complex wake-induced interactions and extracting dominant features to construct a reduced order model as truncated modes highly reduces the order of the reconstructed flow field data (Taira et al., 2017). The main question for the present study is that if POD can decompose the flow field data in a way that most of the energy of the flow field can be captured in the first few modes or not. If this cannot be achieved then both functions of POD is trivial as there will be too many modes present to explicitly identify the discrete physical phenomena occurring in the wake of the rotors and to sufficiently decrease the order of the flow field data.

The literature review revealed that the POD analysis is applicable for a wide range of geometries and Re. It is able to capture the distinct trends in complex wake-structures and turbulent flow characteristics. However, it can struggle while reconstructing less periodic behavior and smaller scale turbulent structures as the lower energy modes are generally truncated and are correlated with those structures (Yousif and Lim, 2021, 2022). Deep et al. (2022) conducted $2d$ POD analysis over a lower Re range between $100-125$ for flow around a cylinder with and without a splitter plate, showing that POD modes are able to successfully capture the change in the vortex shedding behavior and is not effected by the change in flow speed and the geometry of the problem. Even though this study was conducted for much lower Re range than the present study, it is a good indicator for the robustness of the POD analysis. Morton et al. (2018) carried out a similar $3d$ POD analysis for a wall mounted finite circular cylinder between the Re range of $10-400$, again showing that POD is able to capture the wake field characteristics for complex geometries and performs well under the changes in global parameters of the problem. Ping et al. (2020) conducted $2d$ POD analysis to study the suppression of the wake shedding behavior of an oscillating circular cylinder at $Re = 200$ by altering the oscillation frequency, showing that the POD analysis retained it's robustness under dynamic conditions as well. Stankiewicz (2022) compared POD, dynamic mode decomposition (DMD) and recursive dynamic mode decomposition (RDMD) for $2d$ tandem square cylinder cases for altering spacing and Re. The study show that POD method is the least sensitive one to the change in global and geometric parameters of the problem in terms of the time-averaged error of the

reconstructed flow field. Bai et al. (2019) conducted $3d$ POD analysis to study the correlation between the wake structures and the drag reduction for wavy cylinders by altering the geometry of the cylinder in $Re = 3 \times 10^3$ showing that the POD analysis is still robust for Re closer to the one that will be investigated for the present study. Yousif and Lim (2021) and Wang et al. (2014) carried out POD analysis for wall-mounted square cylinders at $Re = 9300$ and $Re = 12000$ respectively. Even though, the number of POD modes to capture the dominant dynamics of the flow were relatively higher for Yousif and Lim (2021) as they conducted POD over time and had to use more modes to sufficiently capture the energy contained in the small scale structures, the POD analysis was still able to sufficiently analyze and reconstruct the flow field data for high Re flows around $3d$ bodies.

It is evident from the literature research that the POD analysis is likely to be able to analyze the wake induced interactions between the wall mounted rotor geometry adopted for this study and to retain it's robustness for a systematic sweep over the global parameters. POD is also highly advantageous since it can greatly reduce the dimensionality of the reconstructed flow field and generates readily available data to be used as a training set for a ML algorithm (Abadía-Heredia et al., 2022). Thus, parametric POD analysis with method of snapshots over the time-averaged flow field data is adopted for the present study as time-averaging is expected to smooth out the small scale turbulence structures and reduce the error in the reconstructed flow field considering POD over time instances can struggle with those small scale structures. It is important to note that method of snapshots is a POD technique generated for datasets with much higher degrees of freedom than snapshots or data points and computationally advantageous over SVD. Note that for each of the studies discussed in the previous paragraph, the POD analysis was carried out for instantaneous flow fields, thus the snapshots were generated by extracting the flow field information at different time instances. The parametric POD adopted for the present study will utilize the steady state time-averaged flow field data and the snapshots will be obtained by parametrically sweeping over the global parameters. This approach is closer to the one adopted by Renganathan et al. (2020) to predict the time averaged flow field data around airfoils due to the change in several global or geometrical parameters. The required number of snapshots to obtain converged modes are generally higher for studies using POD over time due to the erratic nature of the POD coefficients for non-periodic flows. Renganathan et al. (2020) used similar global parameters to the present study for controlling free stream conditions, being the flow velocity and the angle of attack, and used significantly less snapshots to obtain converged results for parametric POD than the other studies implementing POD over time. However, they also parametrized the airfoil shape which resulted in the need of more data-points for a converged POD. In the end they used 90 data-points for their parametric POD analysis and they used 90% of those data-points as the training set for their prediction algorithm. Wu et al. (2019) used 20 data-points to obtain a converged POD analysis and again, used 90% of these data points for training their POD-based class-shape function transformation parametric optimizer. Lorente et al. (2013) used 20 data-points to obtain a converged POD analysis for the pressure distribution over the surface of an airfoil. Finally, Alonso et al. (2012) used RANS simulations to develop a POD-based reduced order model for the external flow around airfoils. Since they used steady RANS equations, the data they obtained is somewhat similar to time-averaged flow wield data. They obtained a converged POD analysis and a sufficient ROM with 35 data-points. The fundamentals of the parametric POD implemented for this study is quite similar to these studies. Thus, it is predicted that approximately 30 data-points (time-averaged simulations) will be enough to obtain a converged parametric POD.

2.5 Reduced order model (ROM) framework

There is a wide range of studies in the literature employing machine learning (ML) to predict flow fields around bluff bodies and aerodynamic/hydrodynamic lifting surfaces, as well as to estimate time-averaged or fluctuating force components acting on such bodies. Generally, two categories of flow-field prediction exist: (i) prediction of future flow states in time, and (ii) prediction of the time-averaged flow field. In the present study, the latter approach is adopted because the flow around the rotors is expected to be statistically steady, and the reconstruction error of the POD modes is expected to be reduced when using time-averaged snapshots, as discussed in Section 2.4. Additionally, ML-based temporal predictions are known to suffer from accumulating errors as the prediction horizon increases (Yousif and Lim, 2022; Lee and You, 2019; Eivazi et al., 2020). Since the objective here concerns steady forces and statistically steady flow fields, temporal prediction is unnecessary.

A deep neural network (DNN) in the form of a multilayer perceptron (MLP) is used in this work. DNNs have been successfully applied to various flow prediction tasks, from temporal flow forecasting to data-driven control, especially when combined with modal decomposition techniques (Min and Jiang, 2024; Li et al., 2022). A MLP is a fully connected feed-forward network that employs non-linear activation functions in its hidden layers, allowing it to approximate non-linear mappings in the training data. This architecture is selected for the present study due to its relatively simple structure, controllable number of parameters, and proven capability to learn nonlinear relationships. A sensitivity analysis will be conducted to examine the influence of the number of hidden layers, hidden-layer width, and choice of nonlinear activation functions on the MLP performance, in order to identify the most suitable network configuration.

ML-based ROMs built upon POD have been shown to perform well when trained on reduced-order flow field data. In such methods, POD coefficients serve as training targets, and the predicted coefficients are subsequently used to reconstruct the fields through linear superposition of the spatial POD modes (Renganathan et al., 2020). Previous POD-ML or DMD-ML ROM studies from Renganathan et al. (2020) and Eivazi et al. (2020) indicate that the number of snapshots required for a converged decomposition is typically sufficient for training the ML model, regardless of whether the snapshots originate from instantaneous or time-averaged flow fields. Therefore, it is assumed that approximately 30 high-quality simulations will provide an adequate dataset for training the MLP. In case this dataset proves insufficient, a probabilistic prediction model based on Bayesian linear regression will also be examined.

Hereafter, the term POD-ML refers to the ML framework used to predict the time-averaged flow field and force coefficients via POD-based reduced order modeling. It is important to emphasize that the goal of this thesis is not to exhaustively compare ML architectures or identify the most accurate surrogate model. Since POD already provides a natural dimensionality-reduction framework and an efficient way to generate compact training datasets, the objective is to explore that if a simple surrogate model is sufficient to obtain satisfactory flow-field predictions. The development of a highly specialized POD-ML architecture is therefore out of the scope of this study. The main objective is to parametrically investigate the physical relationship between rotor-wake interactions and to be able to predict the resulting aerodynamic forces with a fast and simple surrogate model.

3 Methodology

In this section, the overall workflow and methodology adopted in the thesis is outlined to provide a clear and structured overview. The workflow naturally divides into four distinct segments consisting of validation, rotor simulations, proper orthogonal decomposition (POD) via the method of snapshots, and machine learning, each requiring substantially different methodological approaches. Accordingly, the methodology section follows this segmentation to offer a unified and comprehensible summary of the workflow.

3.1 Validation of simulation results

The validation stage aims to verify the accuracy and reliability of the numerical approach implemented in WaterLily.jl before conducting the parametric rotor simulations. The validation cases are selected based on the experimental study of Shehata and Medina (2021) and LES simulations of Liu et al. (2025).

Shehata and Medina (2021) investigated the wake development of a wall-mounted rotating cylinder with the experiments they have carried out in an open surface water tunnel. The experiments were carried out for cylinders with aspect ratios of $AR = 0.5$ and $AR = 1$ at Reynolds number $Re = 10^3$ and for several spin ratios. The wake structures and the variation of time averaged stream-wise and span-wise velocities were presented for diameter based Re of 10^3. The case with $AR = 1$ and $\lambda = 3$ was used as reference. The motivation behind the selection of this case is twofold. First, the case for the aspect ratio of 0.5, the cylinder is fully submerged in the boundary layer of the flat plate which is not the case for a high aspect ratio Flettner rotor. Second, the spin ratio of 3 is much closer to the spin ratios that will be investigated in the present study. The simulations are carried out with Julia based open-source CFD code WaterLily.jl. The computational setup replicated the geometry and boundary conditions of the experiment, modeling a flat plate at the bottom a rotating cylinder inside the flow region. The boundary condition on the flat plate and cylinder is a no-slip wall condition. The inflow condition employs a Blasius boundary layer profile to match the boundary layer profile from the experiments. The outlet plane has a convective outlet boundary condition, the lateral boundaries employ periodic boundary conditions and the upper plane of the domain employs a free-slip condition. The size of the computational domain is $10D \times 10D \times 3D$ in streamwise (x-direction), cross-stream (y-direction) and spanwise (z-direction). The upstream boundary is $2D$ away, downstream boundary $7D$ away, lateral boundaries $4.5D$ away and top boundary $2D$ away from the cylinder surface. The the distance of the upstream surface from the cylinder surface is selected to allow undisturbed flow to reach the cylinder and the rest is selected to allow the wake to develop, eliminate any interference effects from the boundaries and to roughly match the measurement domain from Shehata and Medina (2021). With the size of the current computational domain a blockage ratio of 5.0% is achieved based on the cross sectional area, which is clearly in the acceptable range for these type of experiments (West and Apelt, 1982; Park and Lee, 2000). A sketch of the computational domain is presented in Figure 10. The blockage ratio achieved in the experiments of Shehata and Medina (2021) is 0.14% which would require a domain having a cross sectional area of approximately $(27D \times 27D)$. This is highly computationally expensive as WaterLily.jl utilizes an uniform Cartesian Eulerian mesh structure. $3d$ flow fields were investigated using the Q-criterion for vortex identification to ensure that this domain size was sufficient before running the full simulations by checking if the vortical structures in the wake of the cylinder is effected by the location of the outer

boundaries of the domain. The Blasius boundary layer profile inflow condition was validated against the numerical solution of the Blasius equation and the development of the boundary layer profile was checked with a simulation employing the same domain size and boundary conditions without the cylinder inside the flow region. A mesh convergence study was performed, and the numerical results were validated qualitatively through comparison of the mean velocity contours and quantitatively against the streamwise and spanwise velocity profiles reported by Shehata and Medina (2021). The good agreement obtained especially for the static cylinder case confirmed that the numerical framework accurately reproduces the wake topology and velocity characteristics of the experimental case, providing confidence in its suitability for subsequent rotor interaction simulations.

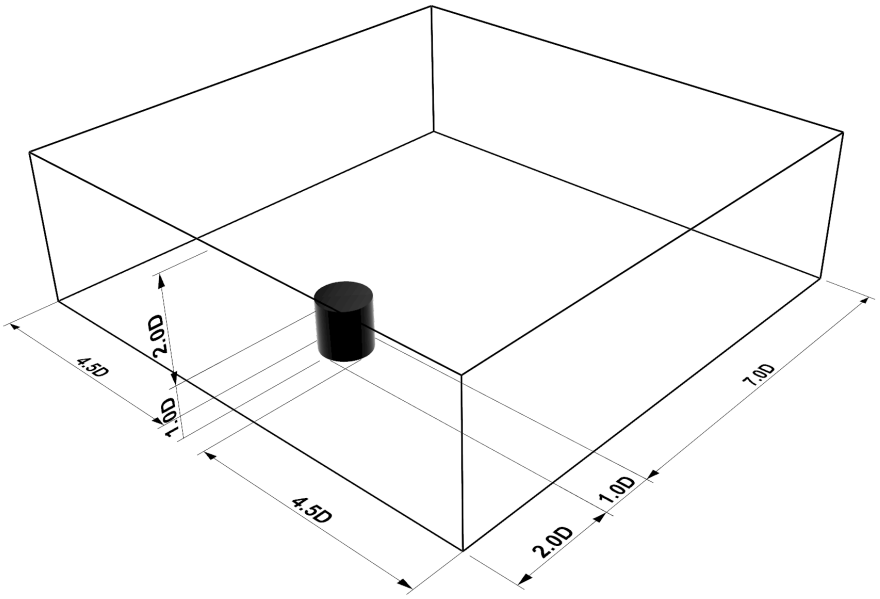

Figure 10: Computational domain for validation against Shehata and Medina (2021).

Liu et al. (2025) investigated the end effects from a finite cylinder with $AR = 10$ and with two free ends, on the wake field and sectional force coefficients on the cylinder for rotation rates ranging from 0 to 5 and Re from 50 to 500. They presented $2d$ slices of the $3d$ computational domain for the instantaneous z-vorticity (ω_z) and $3d$ flow fields using Q-criterion for vortex identification. Furthermore, they presented sectional force coefficients on the cylinder for the whole span. The selected validation case was the case with $Re = 500$ and $\lambda = 3$ as these are the closest conditions to the rotor simulations. Three simulations were carried out in total. For the first simulation, the full span of the cylinder was modeled and Biot-Savart boundary conditions were employed on each external boundary of the computational domain. The second simulation modeled the half span of the cylinder, employed a symmetry boundary condition at the bottom plane and Biot-Savart boundary conditions on the other external boundaries. The third simulation also modeled half span of the cylinder, but employed free-slip wall condition on the bottom plane and Biot-Savart boundary conditions on the other external boundaries. For each case the cylinder surface employs a non-slip boundary condition. The first simulation was used to provide a basis, the second simulation was carried out to validate the computational modeling when only the half span of the cylinder is modeled. The third simulation was carried out to investigate the effect free-slip condition on the bottom boundary which then represents exactly the same boundary conditions and geometrical modeling for the rotor simulations. The

results were compared qualitatively against the $3d$ wake field plots and quantitatively against the sectional force coefficients presented by Liu et al. (2025). The size of the computational domain for the first simulation is $12D \times 5D \times 12D$ in streamwise (x-direction), cross-stream (y-direction) and spanwise (z-direction). The upstream boundary is $1D$ away, downstream boundary $10D$ away, lateral boundaries $2D$ away and top and bottom boundaries $1D$ away from the cylinder surface. For the second and third simulations the computational domain was cut in half in spanwise direction resulting in a domain size of $12D \times 5D \times 6D$. The diameter resolution was the same resolution obtained from the grid convergence study carried out for the validation against the results of Shehata and Medina (2021). A sketch of the half span computational domain for validation against the results of Liu et al. (2025) is given in Figure 11. This domain employs either free-slip or symmetry boundary condition at the bottom plane and the full span domain is obtained by applying symmetry around the bottom plane.

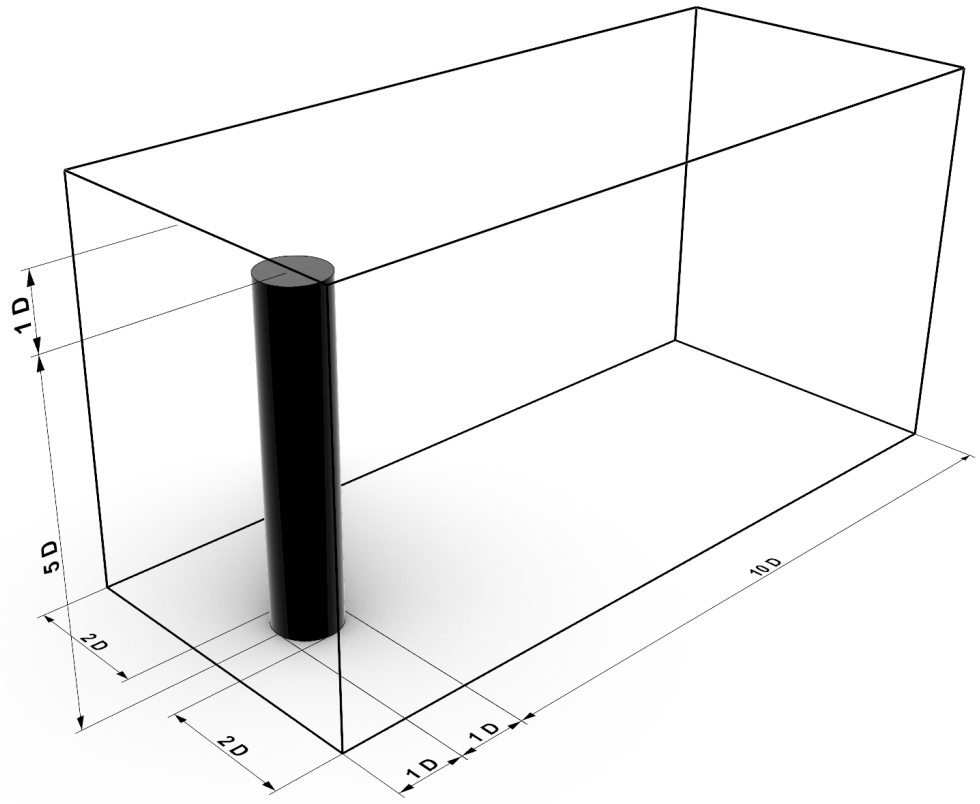

Figure 11: Computational domain for validation against Liu et al. (2025).

3.2 Rotor simulations

Following the validation stage, the numerical setup was extended to perform a systematic series of rotor simulations aimed at investigating the wake-induced interactions between Flettner rotors. All simulations were carried out using the GPU-accelerated CFD solver WaterLily.jl on Delft High Performance Computing Centre (DHPC). The computational domain was defined as $8D \times 5D \times 8D$ in the streamwise, cross-stream, and spanwise directions respectively. The Biot–Savart boundary conditions were implemented for each boundary except the bottom boundary, which uses is a free-slip condition. A no-slip condition was implemented on rotor surfaces. This setup enables accurate simulation of non-aligned inflow directions without requiring domain reorientation and precise results on wake topology in a much smaller

domain compared to a domain employing conventional boundary conditions. The conventional boundary conditions used in the validation case for the experimental results of Shehata and Medina (2021) require the wake of the cylinder to fully develop before reaching the end of the computational domain. This necessity significantly increases both the domain size and the computational cost. The issue becomes even more pronounced for cases involving an angle of incidence, as the required domain size may further expand depending on the wake deflection of the rotors. The Biot-Savart boundary conditions, however, offer the potential to substantially reduce and standardize the computational domain across all simulations. Since these boundary conditions can accurately reproduce the flow even when the inflow velocity vector is not aligned with the domain boundaries (Weymouth and Lauber, 2024), and enable a consistent domain configuration for varying inflow angles. The simulation matrix for the present study is relatively extensive, and the reduced computational cost per case is a significant advantage.

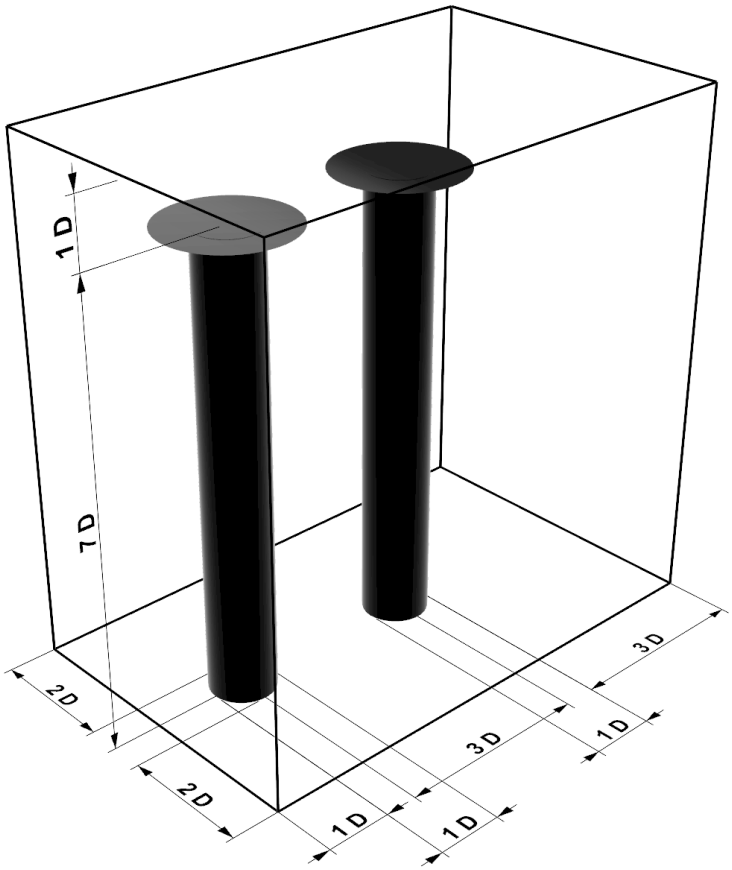

Figure 12: Computational domain for rotor simulations

The aspect ratio of the rotors examined here is considerably higher than that in the experimental validation case and from the related studies by Liu et al. (2024), Afgan et al. (2007), Park and Lee (2000), Rostamy et al. (2012) and Sumner et al. (2004), it can be concluded that the boundary layer over the flat plate is negligible for similar aspect ratios and stable boundary layers. Additionally, the numerical validation case against the computational results of Liu et al. (2025) showed promising results for finite rotating cylinder. Therefore, the Biot-Savart boundary condition is applied with a slip-wall boundary at the bottom plane of the domain with uniform inflow condition, neglecting the influence of the flat-plate boundary layer. Finally, a no-slip wall condition is applied on rotor surfaces. This approach allows the computational

boundaries to be placed much closer to the rotor surface, as illustrated in Figure 12, thereby allowing a higher grid resolution inside the gap region, which is the primary area of interest in this study. The size of the computational domain for generating the snapshot data is $8D \times 5D \times 8D$ in streamwise (x-direction), cross-stream (y-direction) and spanwise (z-direction) directions. The upstream boundary is $1D$ away, downstream boundary $3D$ away, lateral boundaries $2D$ away and top boundary $1D$ away from the closest rotor surface. A sketch of the computational domain for the rotor cases is presented in Figure 12.

3.3 Simulation matrix

The study considers a range of spin ratios $\lambda_1, \lambda_2 \in [3, 4, 5]$, and incidence angles $\theta \in [0°, 15°, 30°]$ as global parameters to capture the variation in wake interaction strength and force response. Each simulation provided time-averaged flow field data and aerodynamic force coefficients for both rotors, forming the basis for subsequent proper orthogonal decomposition (POD) and reduced-order modeling. The rotor simulations thus served as the core dataset generation step, linking the validated numerical framework to the data-driven analysis performed in the later stages of this study. The simulations are carried out at $Re = 1000$. Note that the spin ratios are systematically varied to ensure that the experimental matrix includes asymmetric rotation rates on the rotors as well. This setup results in 27 experiments which means 27 data-points corresponding to each case. This is estimated to be sufficient for both obtaining converged POD modes and generating a sufficient training set for a ML algorithm as similar parametric POD studies used similar number of data-points for parametric POD on turbulent flows around aerofoils (Renganathan et al., 2020; Alonso et al., 2012; Lorente et al., 2013). The simulation matrix is presented in Table 9.

Table 9: Simulation matrix

	$\theta = 0°$		$\theta = 15°$		$\theta = 30°$	
Case No:	λ_1	λ_2	λ_1	λ_2	λ_1	λ_2
1	3	3	3	3	3	3
2	3	4	3	4	3	4
3	3	5	3	5	3	5
4	4	3	4	3	4	3
5	4	4	4	4	4	4
6	4	5	4	5	4	5
7	5	3	5	3	5	3
8	5	4	5	4	5	4
9	5	5	5	5	5	5

3.4 Proper orthogonal decomposition

The Proper Orthogonal Decomposition (POD) analysis was employed to extract the dominant flow structures from the time-averaged flow fields and to quantify how these structures vary with the global parameters $(\lambda_1, \lambda_2, \theta)$ and to provide a suitable training set for the machine learning algorithm. The method of snapshots was adopted because of its suitability for information generated with CFD simulations and to efficiently compute the spatial modes from the high-dimensional flow field data generated in the rotor simulations. For each combination of spin ratios and incidence angles, the time-averaged velocity and pressure fields were collected

and organized into the data matrix, which is then decomposed into orthogonal spatial modes and their corresponding energy-ranked coefficients. Time-averaged flow fields were preferred over instantaneous data to filter out small-scale turbulence and improve the stability of the modal decomposition, as the present study focuses on the statistically steady wake interactions rather than transient dynamics. The convergence of the POD modes was assessed based on the cumulative energy content, and the number of retained modes was chosen to capture at least 95% of the total flow field energy while ensuring efficient dimensionality reduction. This parametric POD approach allows systematic comparison of the wake structures across different operating conditions and provides a compact, high-fidelity representation of the flow field suitable for subsequent machine learning-based reduced-order modeling.

The parametric POD algorithm adopted for this study is similar to the ones used by Renganathan et al. (2020), Alonso et al. (2012), Lorente et al. (2013), Wu et al. (2019) and Braconnier et al. (2011). These studies indicate, the spacing between the snapshots can highly effect the ability of the resulting modes to capture the total energy of the flow field and increase the number of modes needed to capture most of the total energy in the flow field. However, it is difficult to determine a favorable number of snapshots and spacing when sampling the snapshots from the parameter space beforehand. Lorente et al. (2013) adopts an iterative process to generate an algorithm for selecting a favorable sampling of snapshots based on the previous snapshots. This reduces the number of snapshots needed to generate POD modes that can capture most of the energy contained in the full order model (FOM). On the other hand, it is also possible to achieve satisfactory results for the POD modes by considering equal spacing between the snapshots as shown by Renganathan et al. (2020). Thus, equally spaced samples of snapshots, namely generated with Latin Hypercube design methodology, similar to the one adopted by Alonso et al. (2012), in the parameter space is adopted for the present study as explained in Section 3.3. Since WaterLily.jl already provides a significantly reduced simulation time compared to commercial CFD codes, it is not particularly necessary to further reduce the number of snapshots by a small margin (Weymouth and Font, 2025). POD analysis with method of snapshots is conducted on the time averaged flow field data rather than using instantaneous time instances as snapshots. Since the flow field is time-averaged and is not a function of time, rather a function of the global parameters, the mean will not be subtracted from the snapshots as it is generally done for POD over time instances.

3.5 Machine learning

The final stage of the methodology involves developing a machine learning (ML) framework to learn a functional mapping between the global parameters $(\lambda_1, \lambda_2, \theta)$ and the corresponding reduced-order flow representations obtained from the POD analysis, as time cost of POD is substantially small and it is still capable of producing acceptable reconstruction errors compared to the newer approaches such as recursive dynamic mode decomposition (RDMD) (Stankiewicz, 2022). The approach builds upon the concept of using deep neural networks (DNNs) to predict the time-averaged flow field from low-dimensional feature sets. Specifically, the truncated POD coefficients, which capture the dominant energetic modes of the flow field, are used as the target outputs of the network, while the input layer receives the corresponding global parameters describing the simulation configuration. This formulation greatly reduces the dimensionality of the problem and ensures efficient training while retaining the essential flow physics. The DNN architecture is a MLP, which is a fully connected feed-forward network with multiple hidden layers with non-linear activation function. The selected loss-function is mean-squared error

(MSE) and is optimized using the Adam algorithm (Kingma and Ba, 2014).

The convergence of the algorithm is checked at each epoch to introduce an early cut-off criteria to avoid over-fitting. The criteria is the improvement in the loss function of the validation set. After the loss-function of the validation set stops to improve, the training is carried out for an additional of epochs called patience, which is set to 50. If the loss-function has not improved after this patience is applied, the algorithm stops and resets the trained coefficients to the coefficients where the best loss-function value was obtained. 80% of the generated snapshots are used as training set and 20% as validation set. This ratio or 90% to 10% for training and validation sets respectively are the ones generally adopted for similar studies and both are proved to be sufficient (Renganathan et al., 2020; Li et al., 2022; Xu et al., 2023; Yousif and Lim, 2022). While splitting the training and validation sets it is ensured that all combinations of parameters are represented and the extremum points (the fist and last two columns of the data matrix) in the dataset is always kept in the training set for better training. Furthermore, the sensitivity of the predictions on different non-linear activation functions, namely ELU, GeLU, ReLU, SELU, and Swish is investigated as non-linear activation functions generally produce better results for non-linear prediction problems (Murata et al., 2020). The prediction sensitivity depending on the number of hidden layers and hidden layer width is also investigated for each activation function. The number of hidden layers (nHL) are altered between $nHL \in [2, 3]$ and the width of each hidden layer (wHL) is altered between $wHL \in [16, 32, 64]$. After the training is completed, the predicted POD coefficients are combined with the precomputed spatial modes to reconstruct the full three-dimensional flow fields, allowing rapid evaluation of new operating conditions without running additional CFD simulations. For each target flow feature, namely streamwise, cross-stream and span-wise velocity components and pressure, a different DNN with the same layout was trained.

To explore the possibility of better training with a probabilistic ML algorithm, a Bayesian Polynomial Regression (BPR) model was employed. Bayesian regression is particularly well suited for this task because it naturally incorporates regularization, uncertainty quantification, and protection against overfitting, which is crucial when the number of data-points is moderate. A sensitivity analysis on the degree of polynomial features of the input parameters is investigated. The polynomial degree (deg) is altered between $deg \in [2, 4, 6, 8]$ and for each degree the sensitivity of the prediction is investigated if the polynomial coefficients obtained by the multiplication of different parameters are kept in the input array.

The accuracy both algorithms was assessed by comparing the predicted and ground truth values of POD coefficients and the reconstructed full order fields against the ground truth CFD data. Then the reconstructed flow fields are used to predict the forces on the rotors by integrating the pressure and velocity on the surface of the rotors. This final stage effectively links the high-fidelity simulation database with a fast, data-driven reduced-order model, enabling real-time prediction of wake interactions across the parameter space. Finally the errors on the predicted force coefficients from both algorithms are compared to determine the algorithm with higher prediction quality.

In the present work, pressure and velocity fields are modeled with separate reduced-order surrogates rather than recovering the pressure from the predicted velocity field by solving the Poisson equation using the predicted velocity field data. This choice is motivated by several considerations. First, the MLP-predicted velocity field is an approximation and does not strictly

satisfy the governing equations. Using such an approximate field as input to a Poisson solver can amplify small errors in the velocity through the second-order derivatives, leading to pressure fields that are numerically noisy or physically inconsistent. Second, solving a Poisson equation on top of the ROM introduces an additional numerical layer (boundary-condition treatment and iterative solver tolerances), which partially defeats the purpose of having a cheap surrogate model. Third, velocity and pressure generally exhibit different spatial structures and statistical properties, training separate POD-ML models for each quantity allows each ROM to use a basis optimally tailored to that field, rather than forcing pressure to be inferred indirectly from a possibly suboptimal velocity representation.

4 Results and Discussion

This section presents and discusses the results obtained throughout the entire thesis, following the methodological structure established in previous chapters. The findings from the validation study, rotor simulations, POD analysis, and machine learning framework are examined in sequence, with emphasis on the physical interpretation of the flow features, the accuracy of the reduced-order models, and the implications for wake–interaction dynamics in tandem Flettner rotors. By integrating these components, the section provides a comprehensive assessment of the thesis outcomes and evaluates the extent to which the research objectives have been achieved.

4.1 Validation

To ensure the reliability and accuracy of the numerical approach adopted in this study, the simulations are firstly validated against the experimental measurements of Shehata and Medina (2021). Their work investigates the wake structure of a wall-mounted, low-aspect-ratio rotating cylinder at a diameter-based Reynolds number of $Re_D \approx 1000$, using particle image velocimetry (PIV) to capture detailed time-averaged flow fields. Among the tested cases, the configurations with an AR of 1 and spin ratios of $\lambda = 0$ and $\lambda = 3$ was selected for validation. This case provides high-quality reference data for both qualitative and quantitative comparisons, including streamwise and spanwise velocity distributions, recirculation length, and downwash characteristics. In the present study, the validation process involved qualitatively comparing the contour plots of streamwise velocity for both rotating and non-rotating cylinder cases, and quantitatively comparing the location of the maximum downwash and the length of the recirculation region. Matching these flow features in the numerical results is an essential first step before extending the simulations to the more complex tandem Flettner rotor configurations.

Following a preliminary inspection of wake deflection using the Q-criterion for the medium mesh ($D = 72$) in the grid convergence study, it is observed that the $2d$ upstream distance to the cylinder surface was sufficient, as almost no vortical structures were observed in that region. Similarly, the wake deflection was not severe enough to suggest a need for more lateral distance than $4.5D$. In addition, the $7D$ downstream distance was also deemed sufficient, since the rotor simulations will involve a second body located only $2D$ downstream of the first, rather than requiring validation of the wake as far as $10D$ measured by Shehata and Medina (2021). Taking into account the need to balance accuracy with GPU memory limitations for a sufficiently fine mesh, the computational domain presented earlier in Section 3.1 was used. The instantaneous $3d$ wake structures around the rotating cylinder after the wake has stabilized are presented in Figure 13. The Q iso-surfaces for $Q = 1$ are plotted in Figure 13 and they are colored with

the non-dimensional z-vorticity (ω_z). It is clear from the figure that the vortical structures developing from the near-wake region of the cylinder are not hitting the boundaries of the domain.

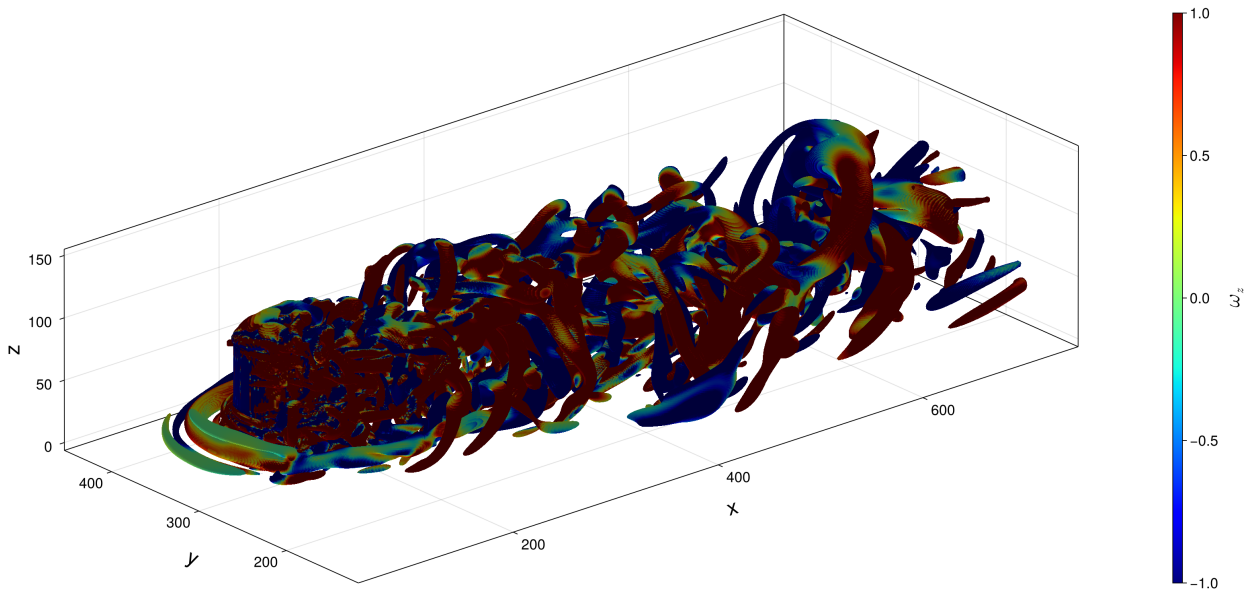

Figure 13: Q iso-surfaces ($Q = 1.0$) colored by non-dimensional ω_z.

The inflow condition for the numerical simulation employs an analytical approximation of the Blasius boundary layer profile to match the experimental setup as Shehata and Medina (2021) state that the developed boundary layer close to the cylinder location follows the Blasius boundary layer profile closely in the experiments. A comparison between the numerical and analytical Blasius profile at the inflow plane of the simulation is presented in Figure 14. The analytical approximation is the one given by He (1998) and is given in Equations 4.1 & 4.2. Here, "η" is the typical similarity variable for the Blasius equation as given in Equation 4.3 (Cengel and Cimbala, 2013). The results of Equations 4.1 & 4.2 are presented compared to the numerical solution of the Blasius boundary layer equations in Figure 14. The numerical solution is obtained by solving the Blasius boundary layer equations with 4^{th} order Runge-Kutta method for $x = 10D$, which is the same length scale used for the inflow boundary condition matching the experimental conditions of Shehata and Medina (2021).

$$f(\eta) = \eta - 1.8760 + 1.4564e^{-\eta} + 1.2956\eta e^{-\eta} + 0.4196e^{-2\eta} \tag{4.1}$$

$$f'(\eta) = 1.0 - 0.1608e^{-\eta} - 1.2956\eta e^{-\eta} - 0.8392e^{-2\eta} \tag{4.2}$$

$$\eta = z\sqrt{\frac{U_\infty}{\nu x}} \tag{4.3}$$

A simulation for the flat plate is carried out using the same domain size presented in Section 3.1 with a flat plate modeled on the bottom boundary of the domain to verify that the boundary layer profile is maintained through the plate in a $3d$ case. The time averaged boundary layer profiles on various locations at the wake centerline for a flat plate is given in Figure 15 showing that the boundary layer is maintained on a flat plate without the presence of a low AR cylinder.

Note that the characteristic length contains 48 grid points for this simulation ($L = 48$) and the total domain size is $x, y, z = (10L, 10L, 3L)$, which is identical with the coarse grid in cylinder cases in the mesh convergence study. For the cylinder simulations, the characteristic length is selected do be the diameter of the cylinder, and will be shown with "D" further in the document.

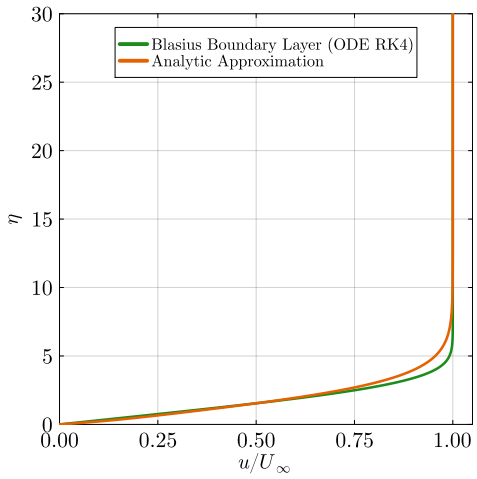

Figure 14: Comparison between numerical solution of the Blasius boundary layer and the analytic approximation

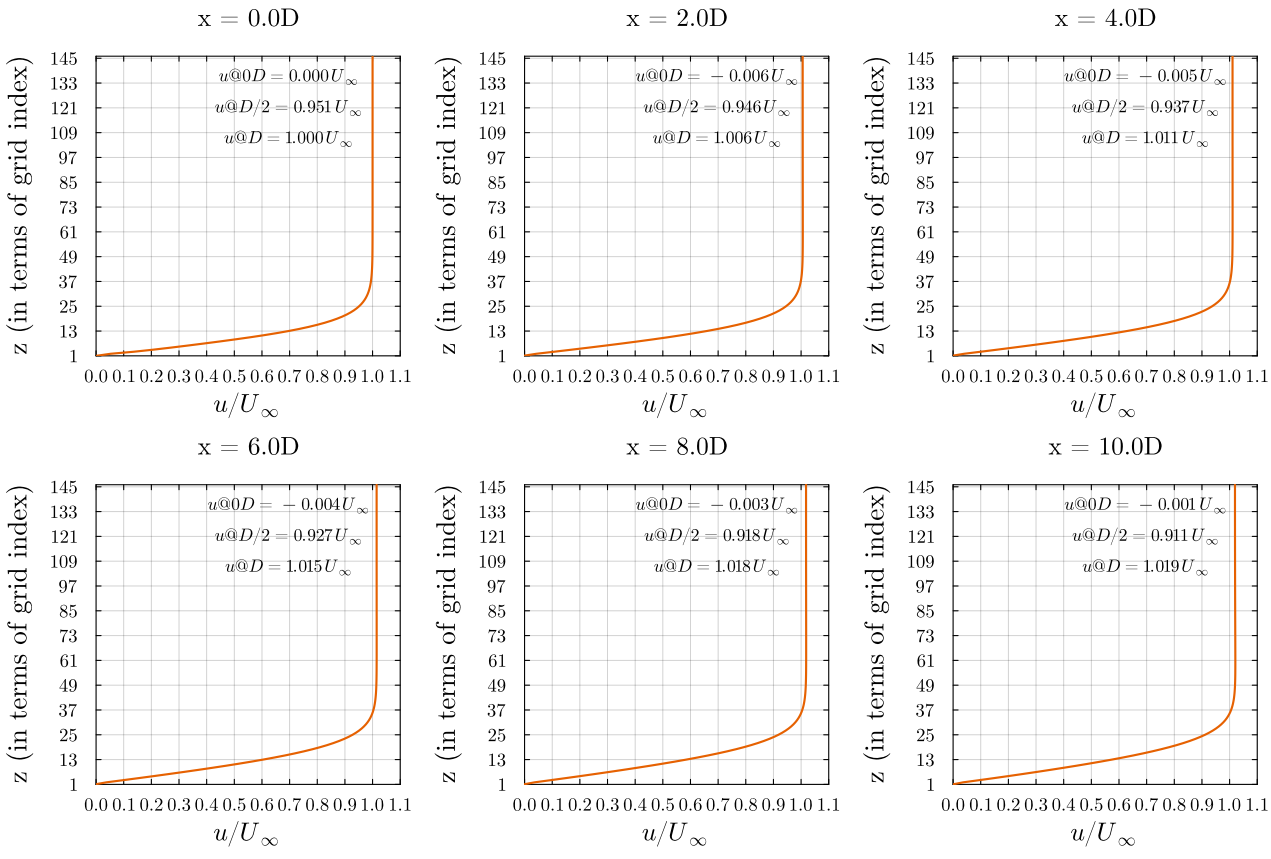

Figure 15: Time averaged velocity profiles on a flat plate ($L = 48$)

After it is verified that the boundary layer profile is maintained on a flat plate the cases for rotating and static cylinders are computed and the time averaged results are presented. The time averaging is started after the standard deviation of the moving average of the instantaneous streamwise velocity of a probe inside the domain just behind the cylinder has reached a steady state. The coordinates for the probe is given by $x, y, x = (4D, 5D, 0.53D)$ for both cases, which corresponds to a location $1D$ behind the cylinder, at the wake centerline and approximately at half height of the cylinder. The moving average of the instantaneous streamwise velocity component recorded by the probe for static and rotating cylinder cases with the moving average and the standard deviation of the moving average are given in Figures 16 & 18 respectively. These statistics are also presented in the time-averaging window in Figures 17 & 19 to show that the standard deviation of the moving average is not high throughout the whole time averaging window and the flow has reached a statistically stable state. The simulations are advanced for 2000 convective time units ($CTUs$) and the time averaging is started at 1500CTU and carried out for $500CTUs$ for both cases. The CTU is calculated with respect to the maximum inflow velocity (U_∞) as in Equation 4.4. The contour plots of the streamwise velocity component are given for both cases with their counterparts from the experiments of Shehata and Medina (2021) in Figures 20 through 23. Note that the simulation results are given for $D = 72$ case which corresponds to roughly $112.0M$ cells inside the domain.

$$CTU = \frac{tU_\infty}{D} \tag{4.4}$$

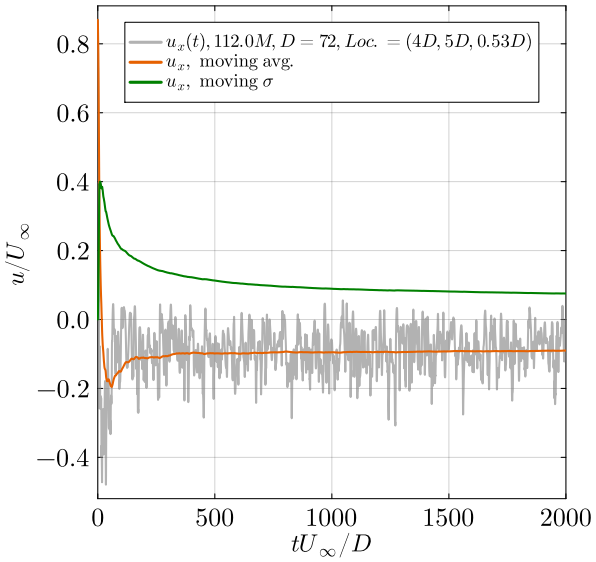

Figure 16: Streamwise velocity component recorded by the probe and its moving average and standard deviation (σ) for static cylinder.

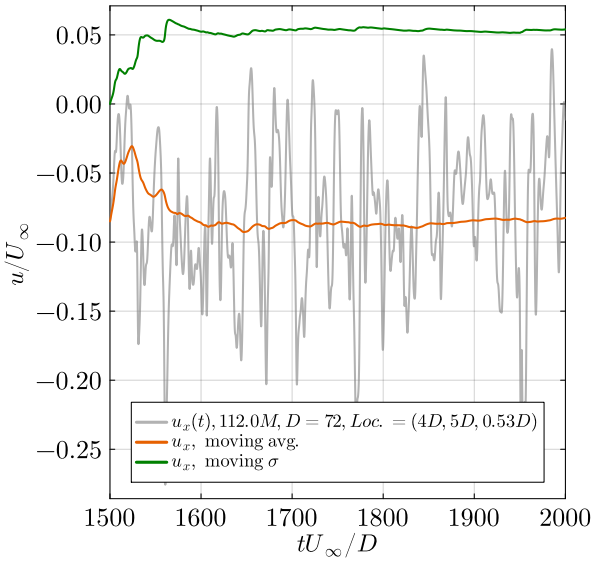

Figure 17: Streamwise velocity component recorded by the probe and its moving average and standard deviation (σ) in the time-averaging window for static cylinder.

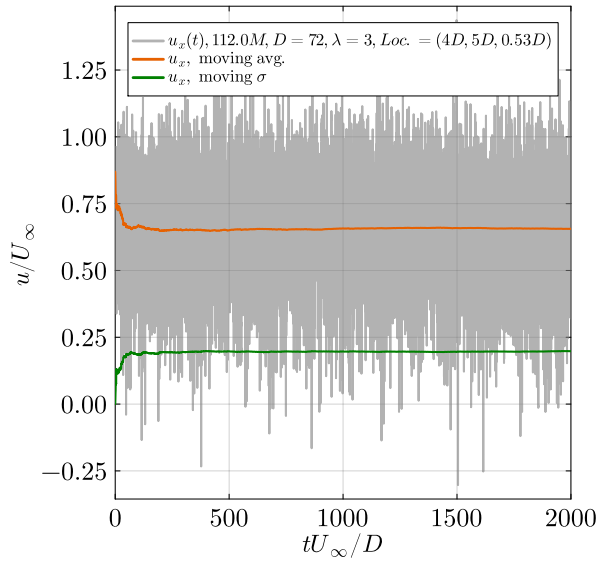

Figure 18: Streamwise velocity component recorded by the probe and its moving average and standard deviation (σ) for rotating cylinder.

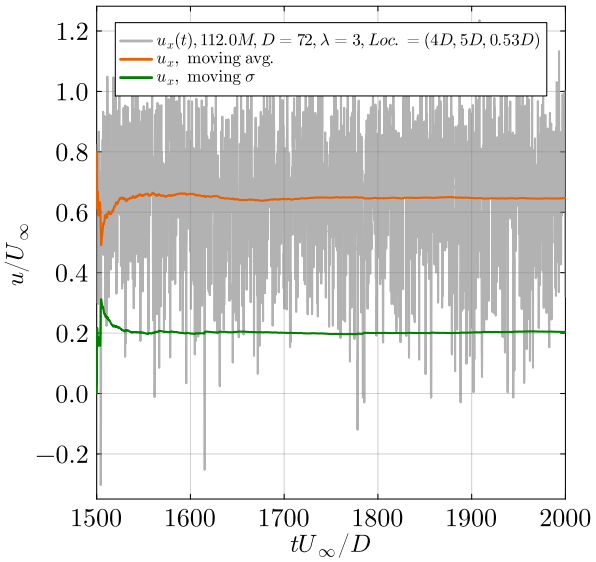

Figure 19: Streamwise velocity component recorded by the probe and its moving average and standard deviation (σ) in the time-averaging window for rotating cylinder.

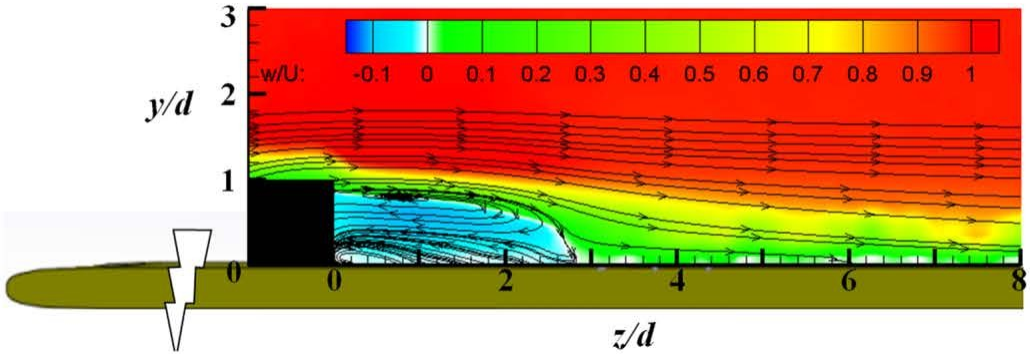

Figure 20: PIV measurement of streamwise velocity contours for static cylinder (Shehata and Medina, 2021).

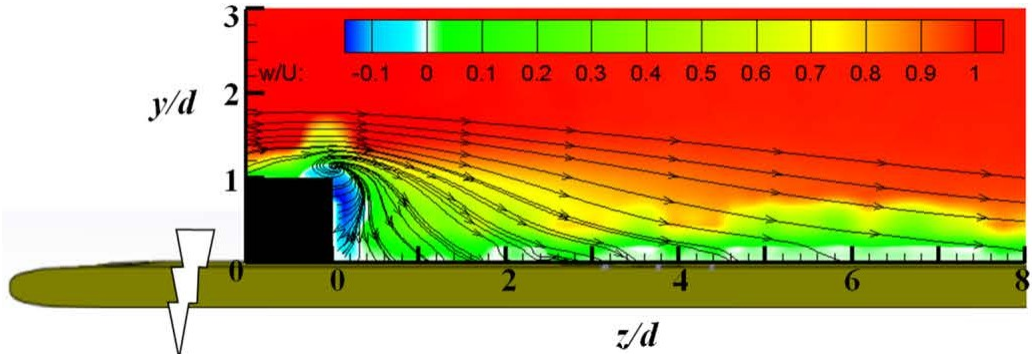

Figure 21: PIV measurement of streamwise velocity contours for rotating cylinder (Shehata and Medina, 2021).

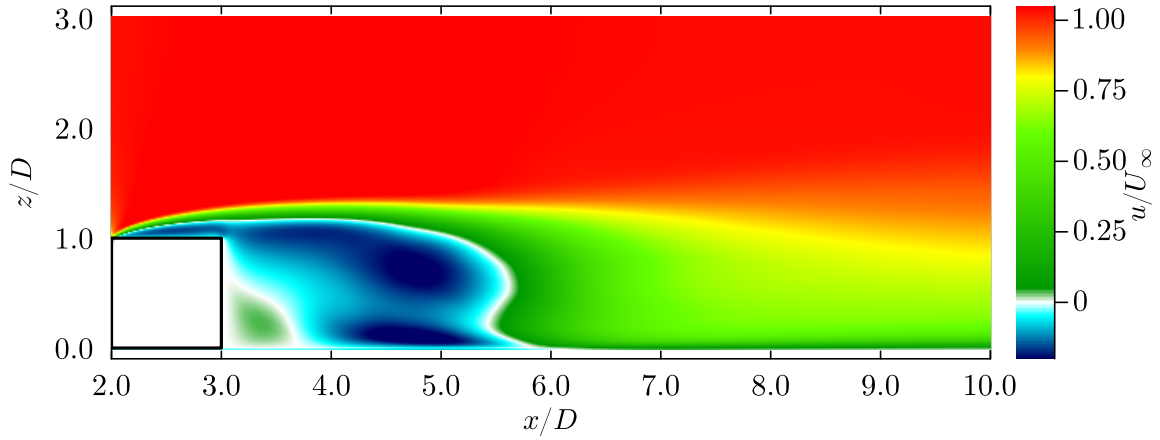

Figure 22: Streamwise velocity contours for static cylinder

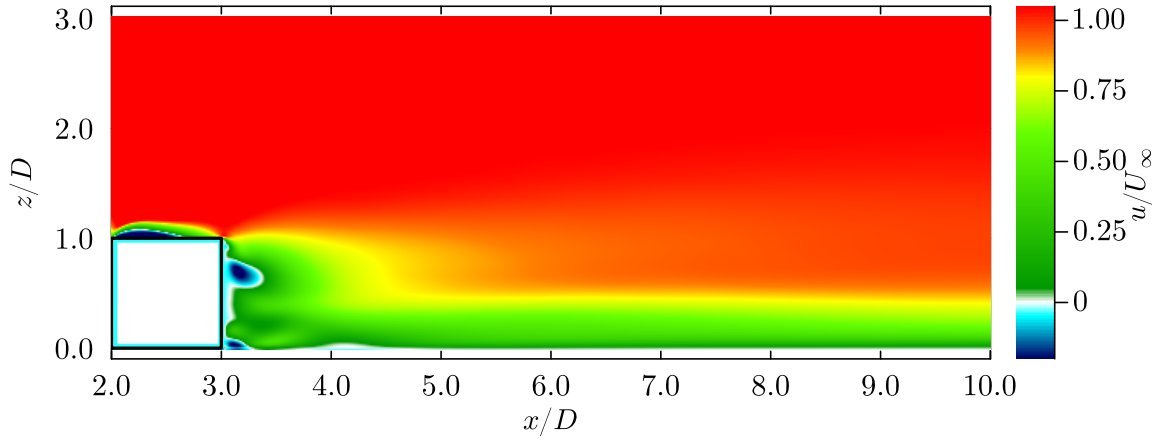

Figure 23: Streamwise velocity contours for rotating cylinder

Figure 20 shows the streamwise velocity contours from the experiments of Shehata and Medina (2021) where, the cross-stream, spanwise, and streamwise directions are selected to be in alignment with the x, y and z axes respectively. However, in the present study the streamwise, cross-stream and spanwise directions are selected to be in alignment with x, y and z axes respectively which better fits with the general convention. From now on, these axes will be used to refer to streamwise, cross-stream and spanwise directions for both the simulations in this study.

Comparison with the simulation results for $D = 72$ reveals several differences. First, the shear layer over the cylinder is not well captured in Figure 20, and the recirculation region behind the cylinder does not extend across the full span in the z-direction, but instead terminates at approximately $z/D = 0.8$. This feature is also evident in Figure 6c of Shehata and Medina (2021) and in Figure 24. Moreover, a closer inspection of the downstream region in Figure 20 shows the persistence of small-scale turbulent structures after time averaging, beginning around $x/D = 4$ and continuing further downstream. These observations raise questions regarding the adequacy of the time-averaging period and whether averaging was initiated only after the flow had reached a statistically steady state, as Shehata and Medina (2021) does not provide details on the procedure followed. This aspect of the time-averaging procedure as well as the analytical approximation of the boundary layer profile are therefore considered to be the primary

sources of the discrepancies between the simulations and the experiments of Shehata and Medina (2021). Thus, it is decided to validate the recirculation length and the spatial location of the maximum downwash instead of the full time-averaged velocity values in the cylinder wake as these values will be highly effected by the time averaging. Nevertheless, the recirculation length is found to be comparable, measuring $2.8D$ in Figure 20 and $3D$ in Figure 22. The two vortical flow systems within the recirculation region are also present in Figure 22, though their centers are located slightly differently. According to Shehata and Medina (2021), these structures are located around $x/D \approx 0.8$, $z/D \approx 0.9$, and near the ground at $x/D \approx 0.2$, $z/D \approx 0.1$. In contrast, Figure 22 shows them positioned further downstream, around $x/D \approx 4.0$, $z/D \approx 0.9$, and $x/D \approx 3.3$, $z/D \approx 0.2$. Similar issues are observed for the rotating cylinder case in Figure 21, where small-scale turbulence emerges almost immediately at $x/D = 0$, reflecting the generally more turbulent nature of the wake. A closer inspection shows that the recirculation length is significantly reduced for the rotating cylinder. In the experiments of Shehata and Medina (2021), it is shortened to approximately $0.3D$, while Figure 23 indicates an even smaller value of about $0.13D$. Finally, no part of the flow fields in Figures 22 & 23 exhibit small-scale turbulence which indicates the time-averaging was carried out correctly for present simulations.

The uncertainty in the velocity vectors for the cross-stream view is reported by Shehata and Medina (2021) as $\delta u_{\text{vec.}} = \delta w_{\text{vec.}} = \pm 0.043$. The uncertainty in the spatial location of the streamwise velocity component is calculated using Equation 4.5, based on a three-point first-order central difference scheme, where the central point corresponds to the zero-crossing ($u_2 = 0U_\infty$) that defines the end of the recirculation region. Similarly, the uncertainty in the spatial location of the spanwise velocity component is determined using Equation 4.6 with a three-point second-order central difference scheme, as the location of the maximum downwash corresponds to a global minimum. In this case, the central value is taken as $w_2 = w_{\min}$.

$$\delta u_{spatial} = \frac{\delta u_{vec.}}{\frac{\partial u}{\partial x}} = \frac{\delta u_{vec.}}{\frac{u_3 - u_1}{x_3 - x_1}} \tag{4.5}$$

$$\delta w_{spatial} = \frac{\delta w_{vec.}}{\frac{\partial w}{\partial x}} = \frac{\delta w_{vec.}}{\frac{w_3 - 2w_2 + w_1}{(x_1 - x_2)^2}} \tag{4.6}$$

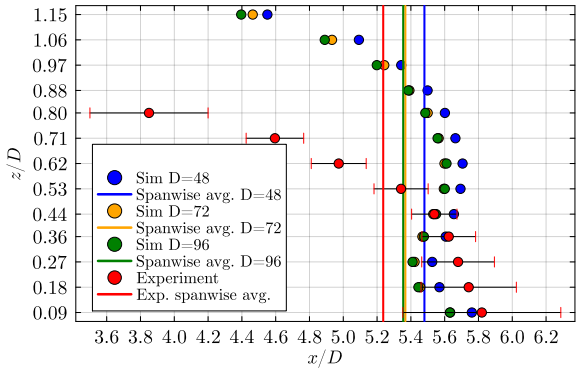

Figure 24: Recirculation length at different z-planes and spanwise averaged recirculation length for static cylinder (Shehata and Medina, 2021).

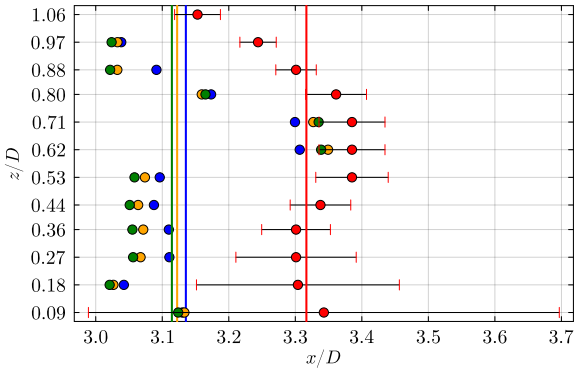

Figure 25: Recirculation length at different z-planes and spanwise averaged recirculation length for rotating cylinder (Shehata and Medina, 2021).

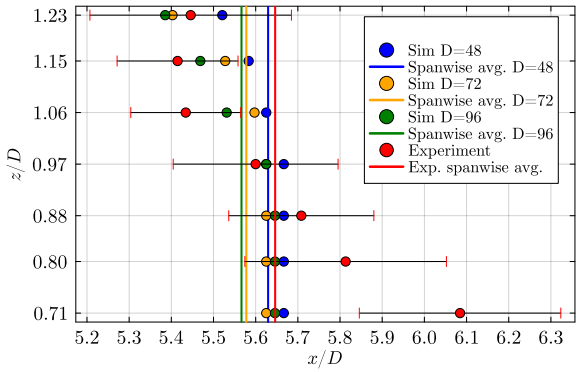

Figure 26: Location of the maximum downwash at different z-planes and spanwise averaged location for maximum downwash for static cylinder (Shehata and Medina, 2021).

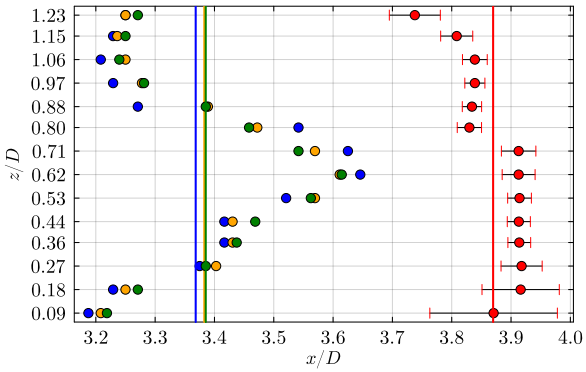

Figure 27: Location of the maximum downwash at different z-planes and spanwise averaged location for maximum downwash for rotating cylinder (Shehata and Medina, 2021).

Figures 24 and 25 present the recirculation length for the static and rotating cylinder cases, respectively. For the static cylinder, the recirculation length is predicted within approximately 3% up to half the cylinder span, after which the experimental and numerical values begin to diverge. In the experiments of Shehata and Medina (2021), the recirculation region terminates at $z/D = 0.8$, whereas in the simulations it extends to the end of the shear layer, at approximately $z/D = 1.15$. Despite these discrepancies across individual z-planes, the spanwise-averaged recirculation length is within 2.50% of the experimental value for the $D = 72$ (medium) mesh. Moreover, the $D = 96$ (fine) mesh does not yield a significant improvement over the medium mesh relative to the additional computational cost. For the rotating cylinder, the numerical results exhibit considerable scatter across the z-planes, although the experimental trend is reasonably captured. The spanwise-averaged recirculation length is predicted within 5.86% of the experimental value for the medium mesh, and again, the fine mesh does not provide a notable improvement.

Figures 26 and 27 show the spatial location of the maximum downwash for the static and rotating cylinder cases, respectively. For the static cylinder, all values, except at $z/D = 0.71$ and $z/D = 1.06$, fall within the experimental uncertainty, and the spanwise average deviates by only 1.21% for the medium mesh. In contrast, the rotating cylinder simulations exhibit pronounced scatter, with the spanwise average being the least accurate, deviating by 12.58% from the experimental value. This discrepancy is likely attributable to the relatively small magnitude of the w-velocity (on the order of 10^{-3}), which makes it more sensitive to modeling errors introduced by the analytic approximation of the boundary-layer profile and the time-averaging procedure.

Based on these observations on mesh convergence, the medium mesh is deemed sufficiently dense for both the static and rotating cylinder cases, as the fine mesh does not yield any substantial improvement relative to the increased computational cost. Therefore, the characteristic length of $D = 72$ is also adopted for the subsequent validation case against the LES results of Liu et al. (2025).

The results for the computational validation case are qualitatively compared against the $3d$ wake field plots and qualitatively against the sectional force coefficients on the rotor presented

by Liu et al. (2025). The selected validation case is the one with $\lambda = 3$ and $Re = 500$ Figure 29 shows the Q iso-surfaces where $Q = 10^{-3}$ for the simulation results and Figure 28 shows the Q iso-surfaces where $Q = 10^{-3}$ presented by Liu et al. (2025) for the cases with $\lambda \in [0, 0.5, 1, 1.5, 2, 2.5, 3, 3.5, 4]$ and $Re = 400$. Unfortunately they did not present the same result for the $Re = 500$ case, but the wake topology in both figures are quite similar. Note that the Q iso-surfaces are colored with non-dimensional ω_z for both Figure 29 and Figure 28.

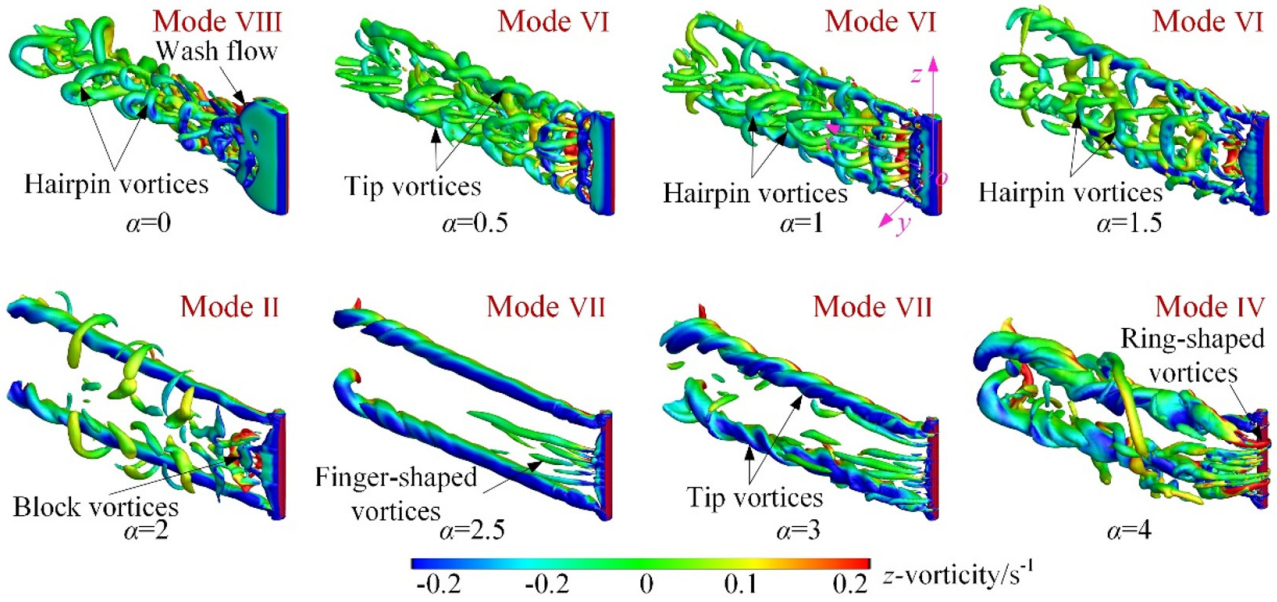

Figure 28: Q iso-surfaces ($Q = 10^{-3}$) colored by non-dimensional ω_z for various rotation rates (α) (Liu et al., 2025).

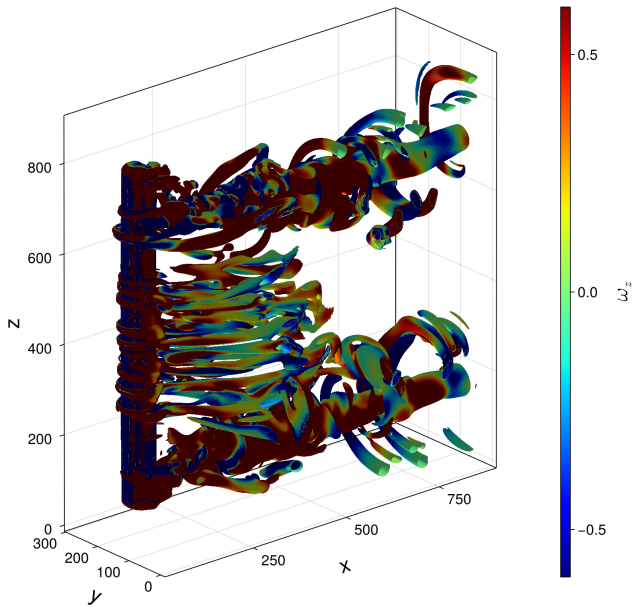

Figure 29: Q iso-surfaces ($Q = 10^{-3}$) colored by non-dimensional ω_z for $\lambda = 3$ for the full span simulation.

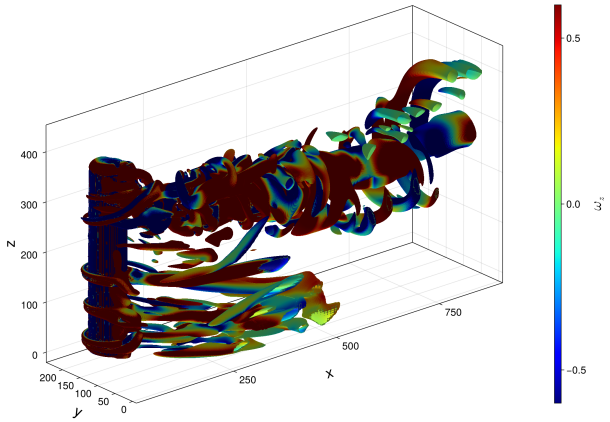

Figure 30: Q iso-surfaces ($Q = 10^{-3}$) colored by non-dimensional ω_z for $\lambda = 3$ for the half span simulation with symmetry boundary condition.

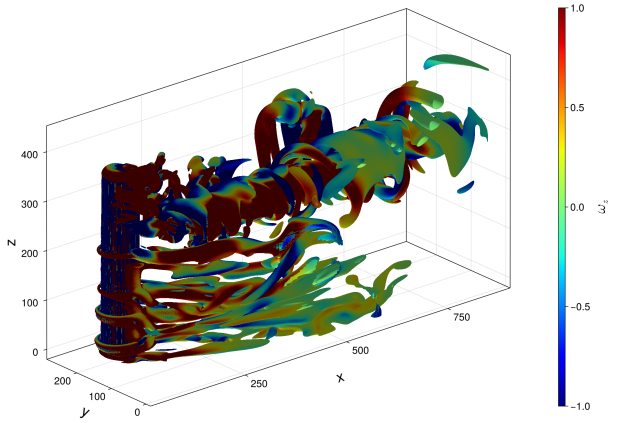

Figure 31: Q iso-surfaces ($Q = 10^{-3}$) colored by non-dimensional ω_z for $\lambda = 3$ for the half span simulation with free slip boundary condition.

The tip vortices and finger-shaped vortices at the mid-span of the cylinder presented by Liu et al. (2025) in Figure 28 for Mode VII is captured quite similarly in the present simulations as shown in Figure 29. Note that the coloring on the Q iso-surfaces are different because Liu et al. (2025) implement rotation in counter-clockwise direction and the present study in clockwise direction. Figures 30 & 31 shows the Q iso-surfaces where $Q = 10^{-3}$ for $\lambda = 3$ for the half domain simulations with symmetry and free-slip boundary conditions on the bottom plane respectively. Figure 30 shows that the exact wake topology as the full span simulation can be obtained with no-problem with the symmetry boundary condition at the bottom plane. Figure 31 shows a quite similar topology to Figure 30 & 29 as well as the Mode VII wake presented in Figure 28 even though the so called finger-like vortical structures at the mid-span of the cylinder are pushed towards the tip of the cylinder a bit more. This qualitative comparison suggests that the free-slip boundary condition is implemented correctly and does not change the wake structure of the cylinder significantly.

Figures 32 & 33 show the time-averaged sectional drag ($\overline{C}_{D_s}$) and lift ($\overline{C}_{D_s}$) coefficient distribution on the cylinder presented by Liu et al. (2025) for each case. Figures 34 & 35 show $\overline{C}_{D_s}$ and $\overline{C}_{D_s}$ distribution for the present simulations.

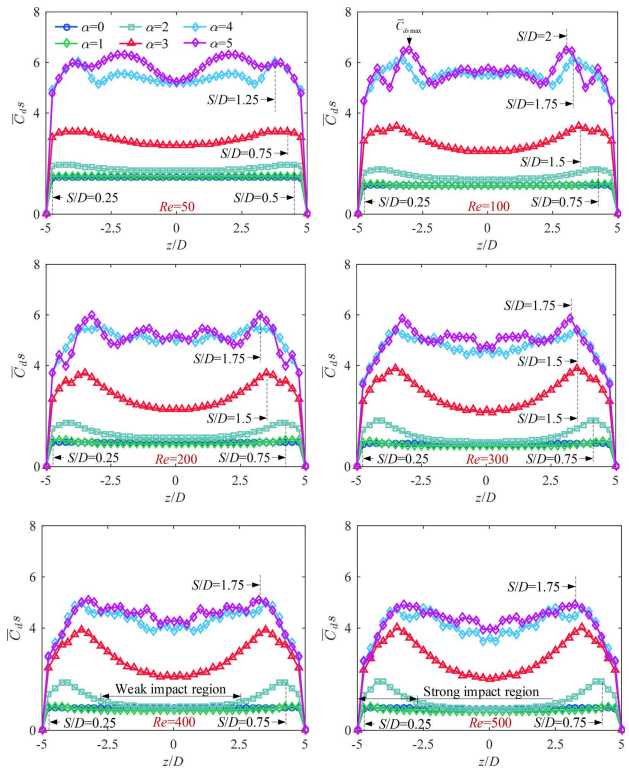

Figure 32: $(\overline{C}_{D_s})$ distributions of the cylinder for various rotation rates (α) and Re (Liu et al., 2025).

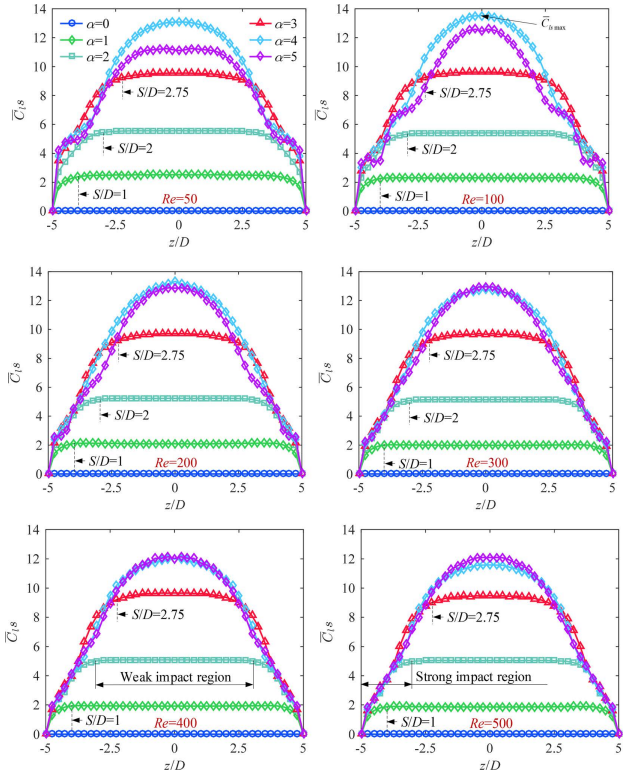

Figure 33: $(\overline{C}_{L_s})$ distributions of the cylinder for various rotation rates (α) and Re (Liu et al., 2025).

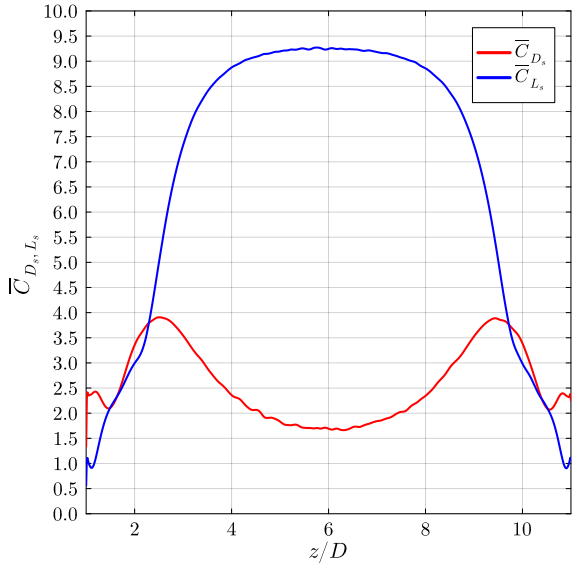

Figure 34: $(\overline{C}_{D_s})$ and $(\overline{C}_{L_s})$ distributions of the cylinder for $\lambda = 3$ and $Re = 500$ for full span simulation.

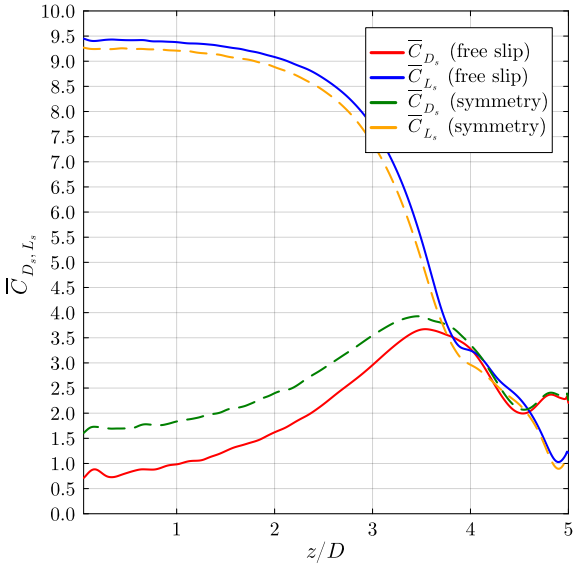

Figure 35: $(\overline{C}_{D_s})$ and $(\overline{C}_{L_s})$ distributions of the cylinder for $\lambda = 3$ and $Re = 500$ for half span simulations.

The full span simulation is able to capture the trend in both $\overline{C}_{L_s}$ and $\overline{C}_{D_s}$ distributions presented by Liu et al. (2025). The location and value of the peaks in $\overline{C}_{D_s}$ are matched quite closely as

well as the maximum value and static lift region for $\overline{C}_{L_s}$. The half span simulation with the symmetry boundary condition is able to reproduce these result and is matched quite closely by the half span simulation with free slip for $\overline{C}_{L_s}$. The $\overline{C}_{D_s}$ is generally under estimated by the half span simulation with free slip boundary condition. However, both the half span simulations with 72 grid points per characteristic length present highly satisfactory results with just a fraction of the computational domain size implemented by Liu et al. (2025). Thus, the same grid resolution and configuration is implemented for the rotor simulations.

4.2 Preliminary results

All the rotor simulations were run in the DelftBlue cluster (Delft High Performance Computing Centre , DHPC) and the computational domain presented earlier in Section 3.2 was used. The first simulation batch was the setup with zero incidence angle (uniform flow along $+x$-axis). Upon first inspection of the results on the flow field, pressure field and rotor forces, a distinct phenomena was discovered for the cases with $\theta = 0$. The upstream rotor experienced a small net thrust force along $-x$-axis and the downstream rotor experienced a drag force along $+x$-axis meaning the rotors are repulsive to each other. This behavior is most pronounced when the rotation rate is the same on both cylinders and/or the rotation rate of the downstream cylinder is higher than the upstream one, where the net thrust force on the upstream cylinder is slightly bigger than the other cases.

In order to confirm and sanity check the results at $Re = 1000$ and validate the post processing of the results, two additional cases were investigated and the results were cross-checked to bring an explanation to this phenomena. The first test case implemented the exact same geometry without the rotation (TC1), and the second test case (TC2) implemented only the upstream cylinder with $\lambda = 3$ to exclude the effect of the downstream one and to provide a basis for comparison. The results were mainly compared to the case with $\lambda_1 = 3$, $\lambda_2 = 3$ and $\theta = 0°$. The hypothesis on the occurrence of this phenomena is explained further in detail after presenting the test cases and the comparison between the results. The probe statistics for both TC1 and TC2 can be found in Appendix B.

The test case with tandem static cylinders (TC1) were run to sanity check the post processing and the boundary conditions of the simulation setup and is qualitatively compared to the results of Maryami et al. (2022), Alam et al. (2003b), Mittal et al. (1997) and Chang et al. (2024). Even though the geometric configurations and the diameter based Reynolds numbers are slightly different then the simulation, these studies provide good qualitative basis and correlate to the static test case in terms of the flow regime around the cylinders. A summary about these studies can be found in Table 7. The comparison is made for the $2d$ pressure, velocity and z-vorticity (ω_z) contours at $z = 3D$ where it is assumed that this location is sufficiently far away from the end plates and the flow here is not effected much by them, because all comparative studies employ tandem static infinite cylinders. Figure 36 & Figure 37 shows time-averaged streamwise velocity ($\overline{u}_x$) and pressure ($\overline{P}$) contours with force coefficient vectors respectively for TC1. Figure 38 shows time averaged vorticity z-vorticity ($\overline{\omega}_z$) contours for TC1, and it is clear from the figure that the shear layers from the upstream cylinder reattaches to the downstream one and generates small scale eddies inside the gap region. Both shear layers shedding from the downstream cylinder clearly curl towards the wake centerline indicating that there is vortex shedding from the downstream cylinder. These observations correlate well with the flow regimes explained by both Maryami et al. (2022) & Alam et al. (2003b). Figure 37

shows good correlation with the steady state solution of Mittal et al. (1997) at $Re = 100$ and Figure 36 shows good correlation with the time averaged velocity contours of Chang et al. (2024) at $Re = 3900$. Additionally, even though they do not provide time averaged z-vorticity contours, their instantaneous snapshots of ω_z shows good correlation with the reattachment flow regime described by Maryami et al. (2022) & Alam et al. (2003b) and the same behavior can also be observed from the $\overline{\omega}_z$ contours in Figure 38.

The flow around a rotating cylinder is widely known and studied extensively in the literature, thus a quick qualitative comparison with the results of Aljure et al. (2015), Padrino and Joseph (2006) and Karabelas (2010) was carried out for TC2. Figure 41 shows $\overline{\omega}_z$ contours for TC2 and it correlates well with the results of Aljure et al. (2015) and Padrino and Joseph (2006). The two distinct shear layers presented by Aljure et al. (2015) at $Re = 5000$ and $\lambda = 2$, and by Padrino and Joseph (2006) at $Re = 1000$ and $\lambda = 3$ are also present in Figure 41. There is no pressure field presented in these studies, however Figure 40 shows good correlation with the pressure distribution on the cylinder presented by Aljure et al. (2015) in terms of the minimum pressure region. If the positive angle is defined counterclockwise from the $y = 0$ axis, the minimum pressure is given to be roughly between $70° - 80°$ for λ from 2 to 5 by Aljure et al. (2015). This agrees well with the low pressure region on top of the cylinder in Figure 40.

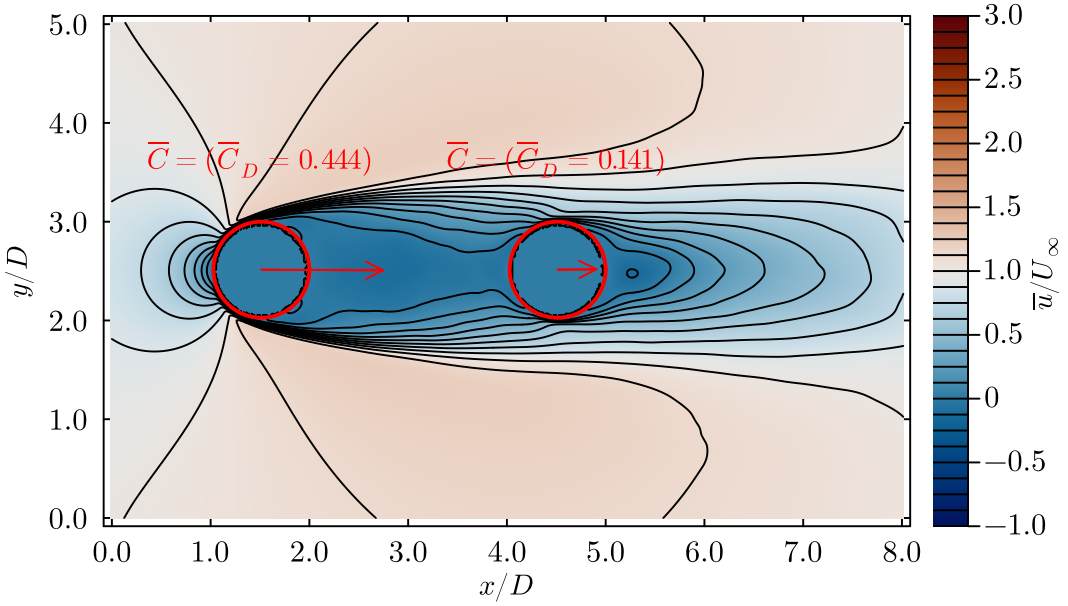

Figure 36: Time averaged streamwise velocity contours with force vectors for TC1 ($z = 3D$).

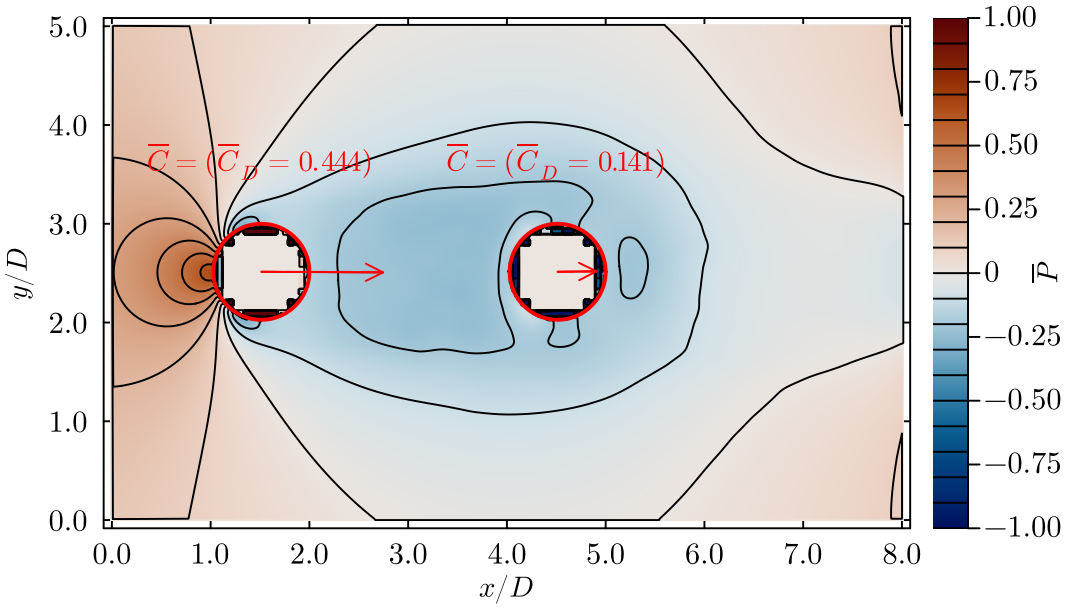

Figure 37: Time averaged pressure contours with force vectors for TC1 ($z = 3D$).

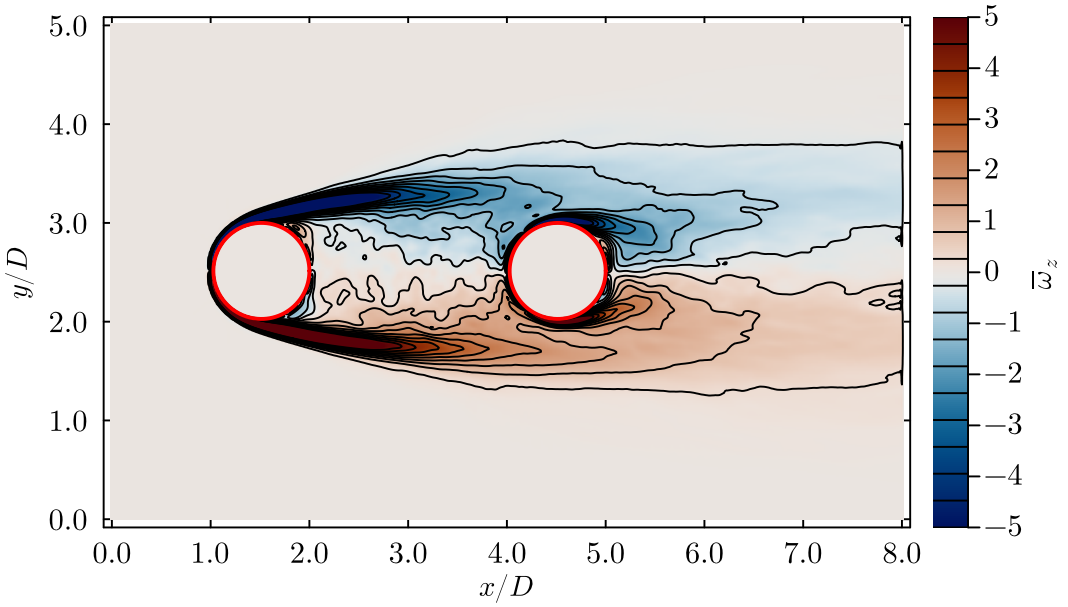

Figure 38: Time averaged z-vorticity contours for TC1 ($z = 3D$).

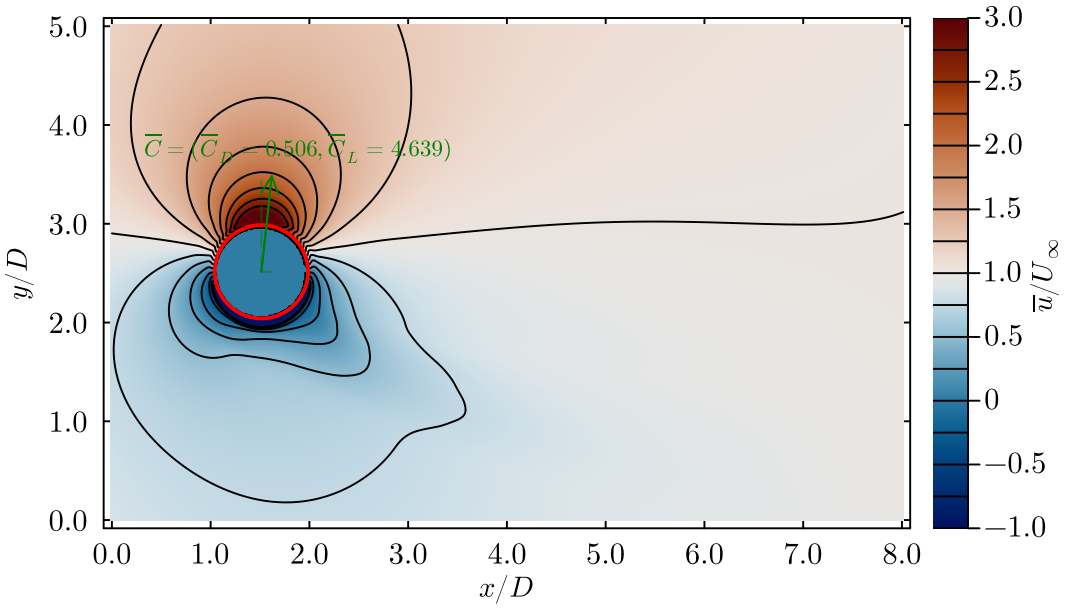

Figure 39: Time averaged streamwise velocity contours with force vectors for TC2 ($z = 3D$).

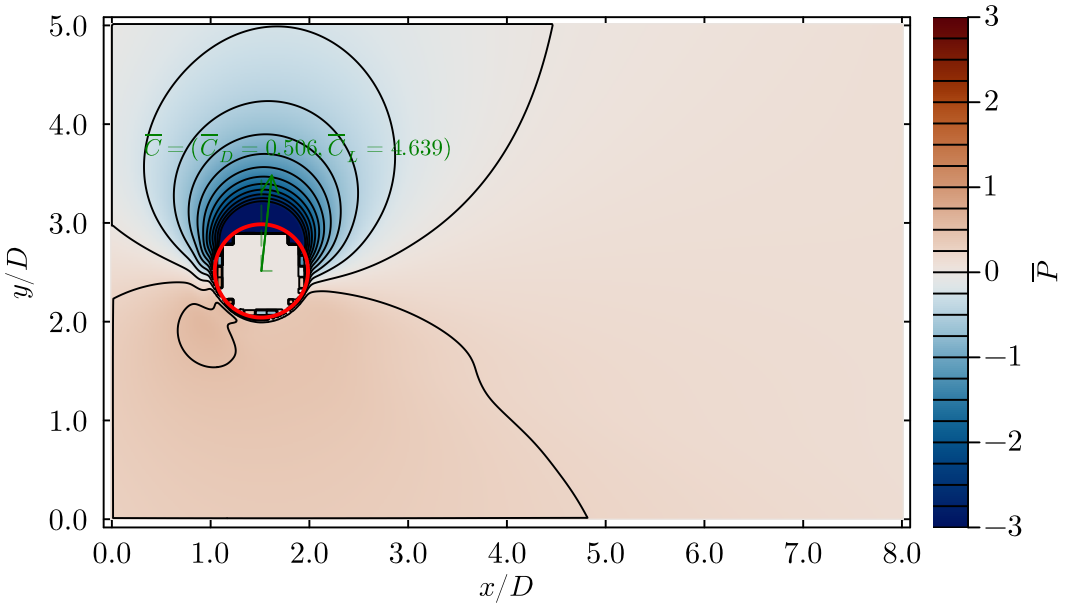

Figure 40: Time averaged pressure contours with force vectors for TC2 ($z = 3D$).

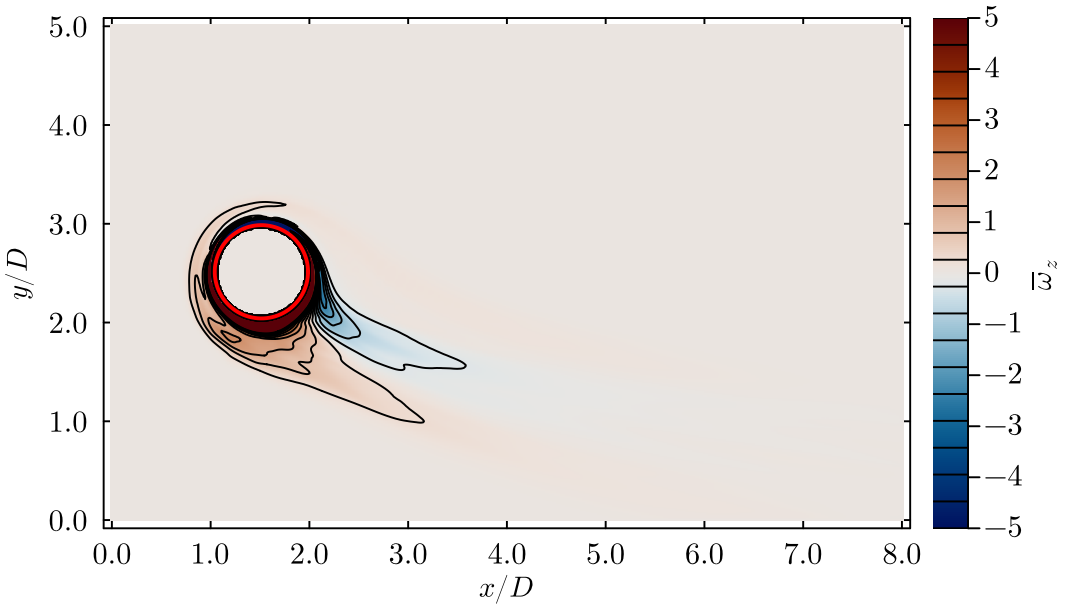

Figure 41: Time averaged z-vorticity contours for TC2 ($z = 3D$).

4.3 Aerodynamic force variation induced by rotor interactions

The repulsive behavior between tandem rotating cylinders observed in the present study was also observed in $2d$ simulations previously by Darvishyadegari and Hassanzadeh (2019), Rastan et al. (2021) and Siddiqui et al. (2024) at lower Re ranging between $100 - 200$ at high rotation rates ranging roughly between $2 - 6$. Darvishyadegari and Hassanzadeh (2019) carried out $2d$ DNS for tandem cylinders at $Re = 200$ for center to center gap ratios (L/D) between $1.5 - 3$ and λ between $0 - 4$. Similarly, Rastan et al. (2021) conducted DNS on 2d tandem cylinders for Re between $100 - 200$, L/D between $2.5 - 6$ and λ between $0 - 5$. Siddiqui et al. (2024) carried out DNS at $Re = 100$ for tandem co-rotating and counter-rotating cylinders for L/D ranging between $1.5 - 4$ and λ from 0 to 6. Each author reported similar findings, and the work of Siddiqui et al. (2024) is analyzed in depth, as it offers a detailed examination of the flow regime around the cylinders. They found that this repulsive behavior starts around $\lambda = 2$ irrespective of L/D and becomes more and more pronounced as the rotation rate increases. They show that the magnitude of the time averaged thrust/drag force coefficients on both cylinders are almost the same and explained this behavior physically by connecting it to the pressure build-up inside the gap region due to the slowed fluid flow in that area. They explain that this pressure is enough to start pushing the cylinders away from each other by overcoming the pressure drag on the front cylinder after $\lambda = 2$. The trend of the magnitude of the thrust/drag force coefficients reported by Siddiqui et al. (2024) is also experienced by Darvishyadegari and Hassanzadeh (2019) and Rastan et al. (2021), and each author explained this repulsive behavior with the pressure buildup inside the gap region. However, the physics behind the repulsive behavior experienced in this study at $Re = 1000$ is considered to be different than the one explained by Darvishyadegari and Hassanzadeh (2019), Rastan et al. (2021) and Siddiqui et al. (2024) since the magnitudes of the thrust/drag forces on the cylinders are quite different. The repulsive behavior at $Re = 1000$ is considered to be dominated by the up-wash induced on the upstream cylinder by the rotation of the downstream one. This up-wash is considered to induce an effective incidence angle on the upstream cylinder tilting the total force slightly towards the

inflow direction and vice versa. This induced effective incidence angle results in the repulsive behavior of the cylinders. A comparison for the x-force coefficients on the cylinders between Darvishyadegari and Hassanzadeh (2019), Rastan et al. (2021), Siddiqui et al. (2024) and the present study is presented in Figure 45. Note that the x-force and y-force coefficients indicate the forces experienced by the cylinders in x and y-directions and are in the same direction as lift and drag coefficients respectively. This notation is used for generalization since for some cases the upstream rotor experiences thrust force rather than drag.

Each author mentioned in the previous paragraph carried out $2d$ DNS and used the force coefficients as $C_F = 2F/\rho U_\infty^2 D$ where the present study uses the so-called wetted surface area of the rotors to non-dimensionalize both force coefficients as $C_F = 2FS/\rho U_\infty^2 \nabla$. The wetted surface area for one rotor is calculated as $\nabla = 35\pi D^2/4 + 2\pi(2\epsilon + \sqrt{2})$ where "ϵ" is the kernel width employed in the simulations which is set to one grid point. The expression "$(2\epsilon + \sqrt{2})(1/D)$" defines the rotor end plate thickness in the simulations. However, to provide a better comparison between the studies, the sectional force coefficients at a section where the force coefficient is not effected by the bottom boundary and end-plates was made. The sectional force coefficient distribution on the rotors for each case plotted in Figure 45 is presented in Figures 42, 43 & 44. These figures show that for the bigger portion of the span of both cylinders, the sectional forces are not effected by the end-plate and the bottom boundary and behaves like the force coefficient distribution presented for the validation case in Figure 35. Thus, the sectional force coefficient at $z = 2D$, which is sufficiently away from both the bottom boundary and the end-plate effects, is selected for comparison in Figure 45. The figure also shows the boundary that marks the change in x-force on the upstream cylinder due to the rotation of the downstream one, and vice versa, as predicted by a simplified model in potential theory combined with the Kutta–Joukowski theorem. The velocity field around a rotating cylinder, can be represented as the superposition of a uniform flow, a dipole flow, and an irrotational vortex flow. However, both cylinders are simplified into $2d$ point vortexes with circulation strength equal to a cylinder with a non-dimensional rotation rate of $\lambda = 3$ to avoid having to satisfy the boundary conditions required to maintain the circle radius. Then, "Γ" represents the circulation strength created by a rotating cylinder with radius "a" at its center, and is given as in Equation 4.7.

$$\Gamma = 2\pi a^2 \Omega = \frac{\pi}{2} D^2 \Omega \tag{4.7}$$

Using the definition of non-dimensional rotation rate and substituting $\Omega = \frac{2\lambda U_\infty}{D}$ gives:

$$\Gamma = 2\pi a \lambda U_\infty \tag{4.8}$$

Then a small trick should be applied to predict the drag change due to the induced radial velocity on the upstream cylinder. Because of D'alembert's paradox the drag on a point vortex in potential flow under incoming uniform flow is zero. Therefore, the trick is to use a local coordinate system on the upstream vortex, assuming the induced radial velocity experienced by the upstream vortex as the uniform flow velocity and calculating the lift on the vortex due to the induced radial velocity. The lift calculated with respect to the local coordinate system will point towards the $-x$-axis in the global coordinate system. The induced velocity in y-direction from the downstream vortex on the upstream one is given as in Equation 4.9

$$u_{i,y} = \frac{-\Gamma}{2\pi} \cdot \frac{r_x}{r} = \frac{-\Gamma}{2\pi} \cdot \frac{-6a}{(6a)^2} = \frac{\Gamma}{12\pi a} \tag{4.9}$$

The force on a vortex is given in Kutta-Joukowski theorem as Equation 4.10.

$$F = -\rho U \Gamma \tag{4.10}$$

Then, plugging in the induced velocity and the circulation strength for the upstream vortex yields Equation 4.11

$$F = -\rho \cdot \frac{\Gamma}{12\pi a} \cdot \Gamma = \frac{-\rho \Gamma^2}{12\pi} = \frac{-\rho \pi a \lambda^2 U_\infty^2}{3} \tag{4.11}$$

Equation 4.11 is subsequently non-dimensionalized to yield the change in x-force coefficient, as shown in Equation 4.12, with $D = 2a$. It should be emphasized that potential theory allows only the estimation of the change in x-force coefficient, rather than the total drag. Nevertheless, this estimation closely approximates the total thrust force acting on the upstream cylinder, since the drag on a single rotating cylinder is already negligible, as illustrated in Figure 40.

$$\Delta C_x = \frac{\frac{-\rho \pi a \lambda^2 U_\infty^2}{3}}{\rho U_\infty \pi a} = \frac{\lambda^2 U_\infty}{3} \tag{4.12}$$

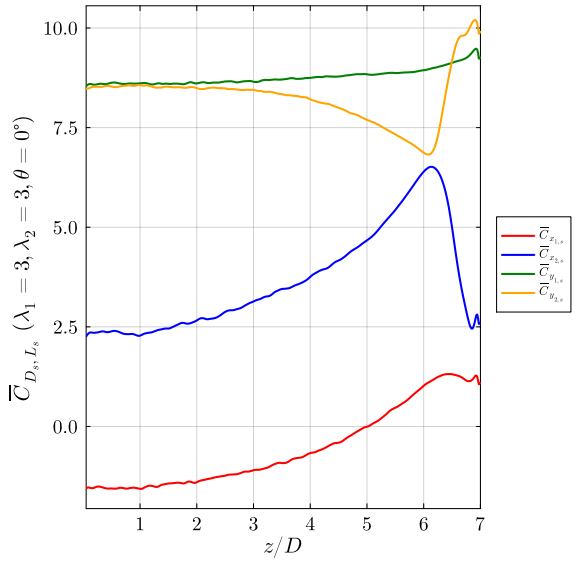

Figure 42: $(\overline{C}_{x_s})$ and $(\overline{C}_{y_s})$ distributions on the cylinders for $\lambda_1 = 3$, $\lambda_2 = 3$, $\theta = 0°$.

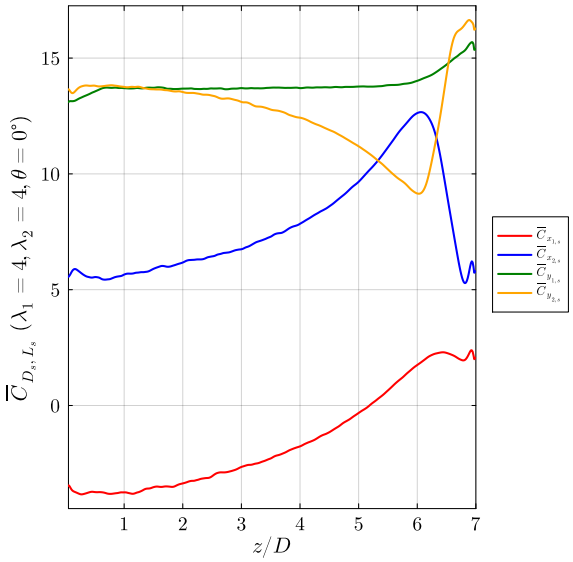

Figure 43: $(\overline{C}_{x_s})$ and $(\overline{C}_{y_s})$ distributions on the cylinders for $\lambda_1 = 3$, $\lambda_2 = 3$, $\theta = 0°$.

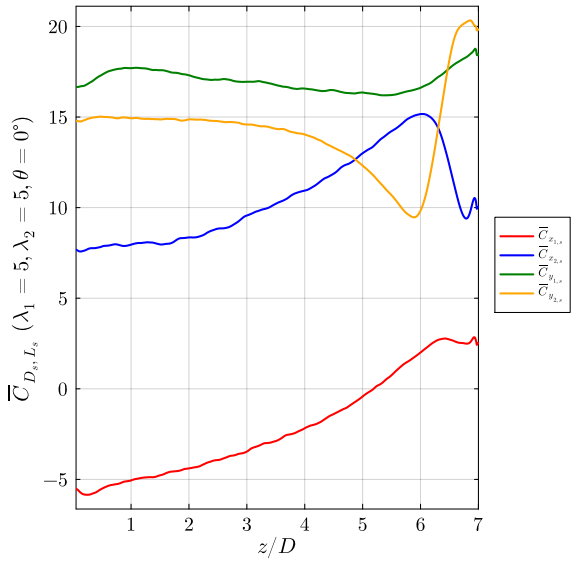

Figure 44: $(\overline{C}_{x_s})$ and $(\overline{C}_{y_s})$ distributions on the cylinders for $\lambda_1 = 5$, $\lambda_2 = 5$, $\theta = 0°$.

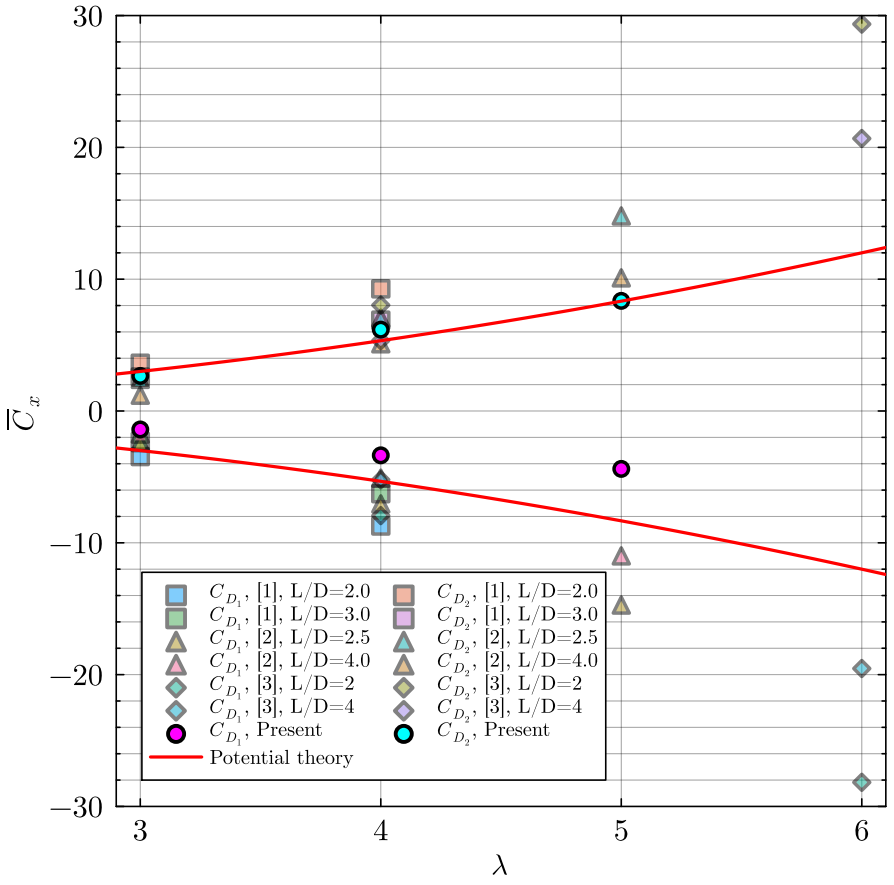

Figure 45: Thrust and drag force coefficient magnitudes on tandem rotating cylinders for different λ and L/D. [1]: $Re = 200$ (Darvishyadegari and Hassanzadeh, 2019), [2]: $Re = 100$ (Rastan et al., 2021), [3]: $Re = 100$ (Siddiqui et al., 2024), [4]: $Re = 1000$ Present

Figure 45 shows that in lower Re, $2d$ simulations of tandem rotating cylinders, the repulsive behavior consistently strengthens with increasing rotation rate, largely independent of L/D, and the force magnitudes on the two cylinders remain nearly equal. Previous authors have attributed this to the pressure buildup inside the gap region. Once $\lambda \geq 2$, the elevated pressure overcomes the pressure drag on the upstream cylinder and drives it into thrust, while simultaneously augmenting the downstream cylinder's drag. This picture, however, does not fully capture the dynamics at higher Re. In the present $3d$ study at $Re = 1000$, viscous effects are greatly reduced and inertial effects dominate compared to lower Re cases, bringing the flow around the upstream cylinder closer to potential-flow behavior, while the dominant mechanism becomes the up-wash induced by the downstream cylinder. This up-wash effectively introduces an incidence angle on the upstream cylinder, tilting the net force towards the inflow direction and producing the observed x-force change. Importantly, the potential-flow estimate of the x-force change agrees closely with the measured force coefficients in the present study especially for the downstream cylinder, whereas the pressure-buildup hypothesis cannot account for the pronounced difference in magnitudes. The upstream cylinder experiences less thrust per unit length compared to the potential model and the downstream cylinder experiences drag which is almost the same as the force change estimated by the potential model in terms in terms of force magnitudes. This is attributed to the pressure drag acting on both cylinders, which cannot be calculated by potential theory and reduces the thrust force on the upstream one and increases the drag force on the downstream one, thus creating the difference between the potential model and the simulations. However the pressure drag experienced by the downstream cylinder is less because it operates in the wake of the upstream cylinder which brings the total drag experienced by it closer to the potential model force change estimate in terms of magnitude. This indicates that, at high Re, the repulsive behavior is better explained by potential-flow mechanisms rather than by gap-region pressure buildup as the present simulations follow the trend of the potential estimation quite closely, even though the overall trend of increasing repulsiveness with rotation rate remains consistent across both low and high Re cases. To further examine the mechanisms underlying the repulsive behavior identified in Figure 45, the time averaged flow fields are also included for each case. Furthermore, to provide an insight on the repulsive behavior when the rotation rate is different, flow fields for two additional cases being $\lambda_1 = 3$, $\lambda_2 = 5$, $\theta = 0$ and $\lambda_1 = 5$, $\lambda_2 = 3$, $\theta = 0$ are also included. Note that all $2d$ slices of the flow fields are taken at $z = 2D$. The probe statistics for each case can be found in Appendix B.

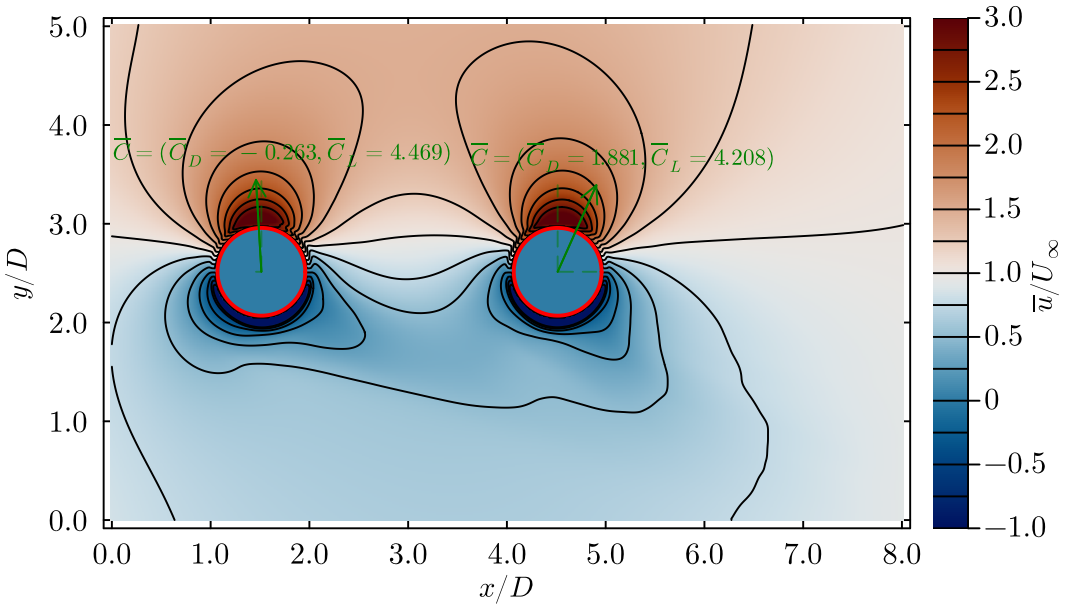

Figure 46: Time averaged streamwise velocity contours for $\lambda_1 = 3$, $\lambda_2 = 3$, $\theta = 0°$ ($z = 2D$).

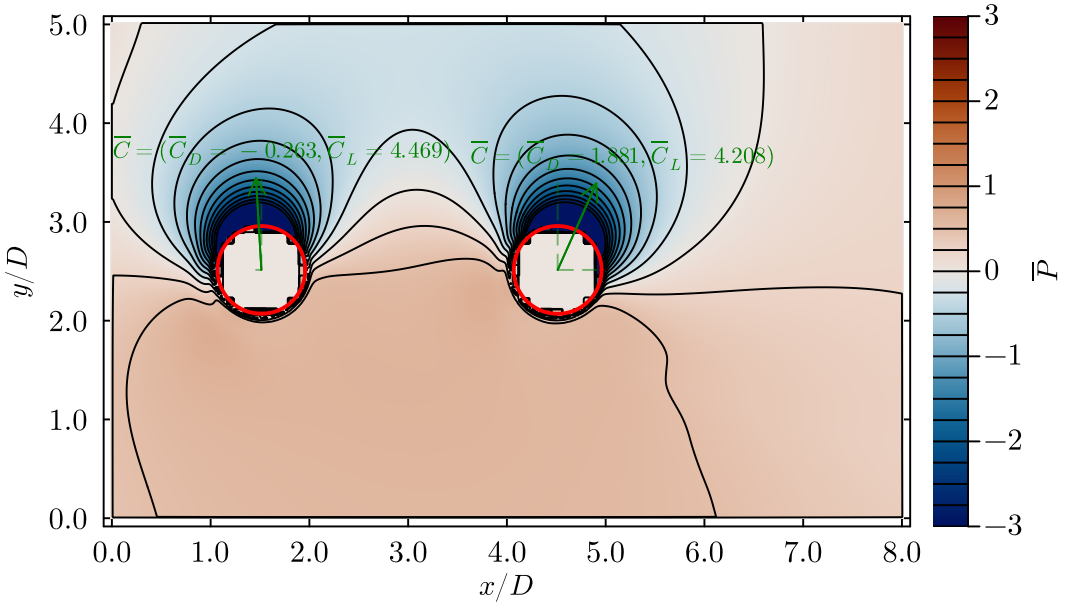

Figure 47: Time averaged pressure contours for $\lambda_1 = 3$, $\lambda_2 = 3$, $\theta = 0°$ ($z = 2D$).

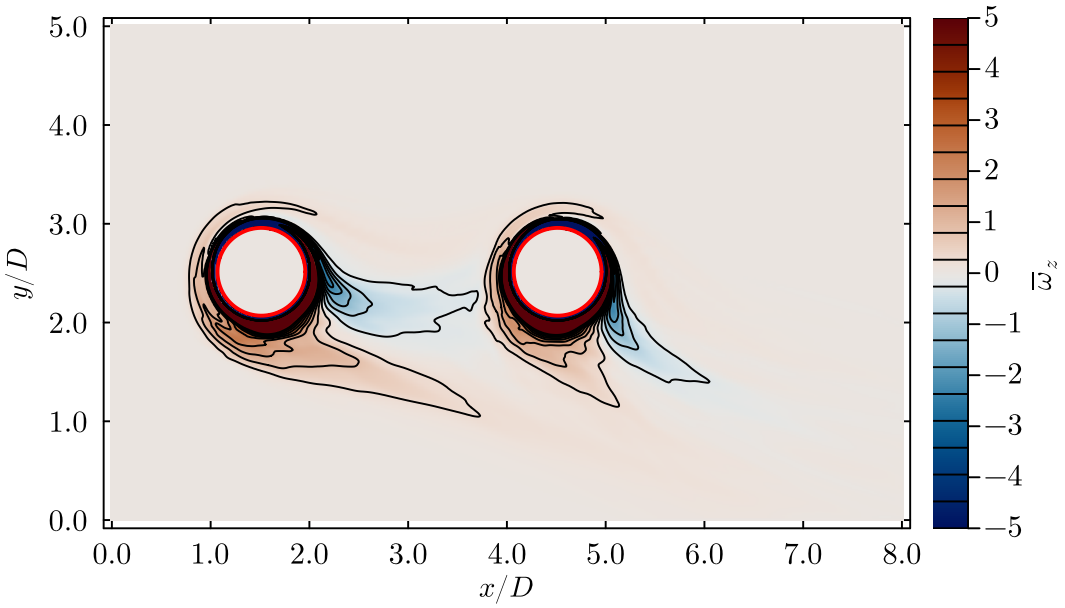

Figure 48: Time averaged z-vorticity contours for $\lambda_1 = 3$, $\lambda_2 = 3$, $\theta = 0°$ ($z = 2D$).

Figure 47 shows the pressure contour lines inside the gap region is tilted upwards as a result and the zero relative pressure area is also misplaced along $+y$-axis. It is clearly visible from a quick comparison between Figure 47 and Figure 39 that the low pressure region on top of both cylinders have changed locations compared to the low pressure region on a single rotating cylinder. The low pressure region on the upstream and downstream cylinders are pushed towards the second and first quadrant of the cylinders respectively. This shift on the low pressure region changes the direction of the total force vector for both cylinders and apparently overcomes the pressure drag of the upstream cylinder to apply a small thrust force on it while adding to the pressure drag of the downstream one. This low pressure region misplacement is much more pronounced for higher rotation rates such as $\lambda_1 = 4$, $\lambda_2 = 4$, $\theta = 0°$ and $\lambda_1 = 5$, $\lambda_2 = 5$, $\theta = 0°$ cases as shown in the pressure contour plots in Figures 50 & 53 for these cases. These figures show clearly higher displacement on the pressure contours and zero relative pressure area towards the $+y$-axis. Additionally, the higher displacement on the low pressure regions on the cylinders result in higher repulsive behavior.

Figure 48 shows the $\overline{\omega}_z$ contours for $\lambda_1 = 3$, $\lambda_2 = 3$, $\theta = 0$. Two shear layers separating from both cylinders, much like the single cylinder case presented in Figure 41, are still visible and these shear layers does not form a vortex shedding regime. However, the shear layers separating from the upstream one is pushed ipwards in $+z$-direction and the negative shear layer reattaches to the downstream cylinder. This behavior was also observed by Siddiqui et al. (2024). This angle change on the shear layers separating from the upstream cylinder is caused by the up-wash along $+y$-axis induced by the rotation of the second cylinder, which also confirms the theory explained before on the induced effective incidence angle on the upstream cylinder. Figure 51 shows that the flow regime around the cylinders have completely changed for $\lambda_1 = 4$, $\lambda_2 = 4$, $\theta = 0$. One of the shear layers on the upstream cylinder moves around the cylinder an is detached from the same side as the other shear layer. For the downstream cylinder, both shear layers wrap around the cylinder and does not separate. Figure 54 shows that the flow regime changes once again at high rotation rate for the $\lambda_1 = 5$, $\lambda_2 = 5$, $\theta = 0$

case. The shear layers are wrapped around the cylinder for both upstream and downstream cylinders. For each tandem rotating cylinder case presented here, there is no vortex shedding from either cylinder and the wake is in steady state.

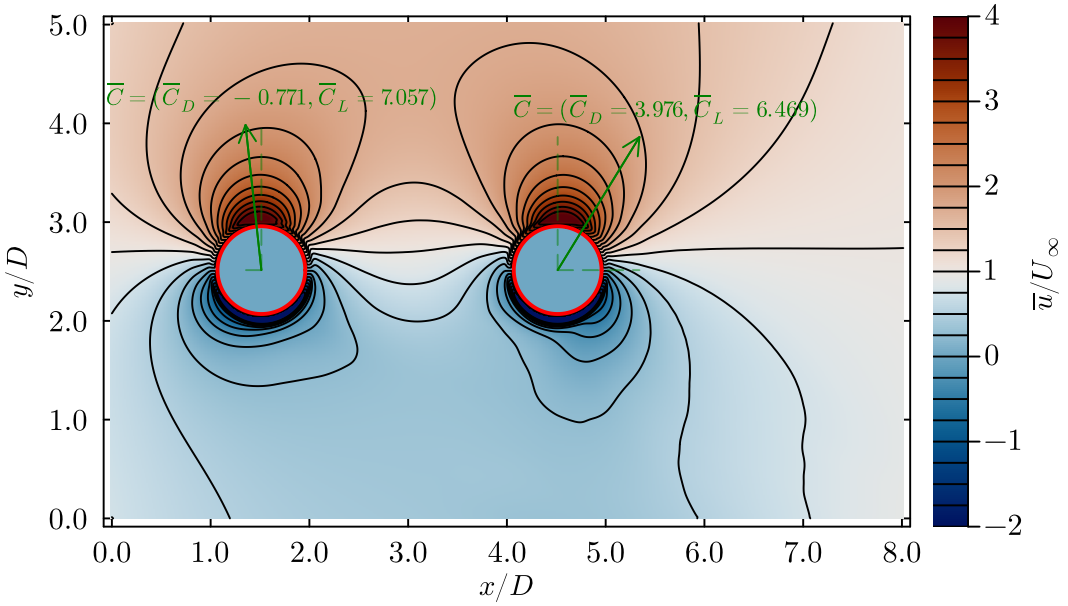

Figure 49: Time averaged streamwise velocity contours for $\lambda_1 = 4$, $\lambda_2 = 4$, $\theta = 0°$ $(z = 2D)$.

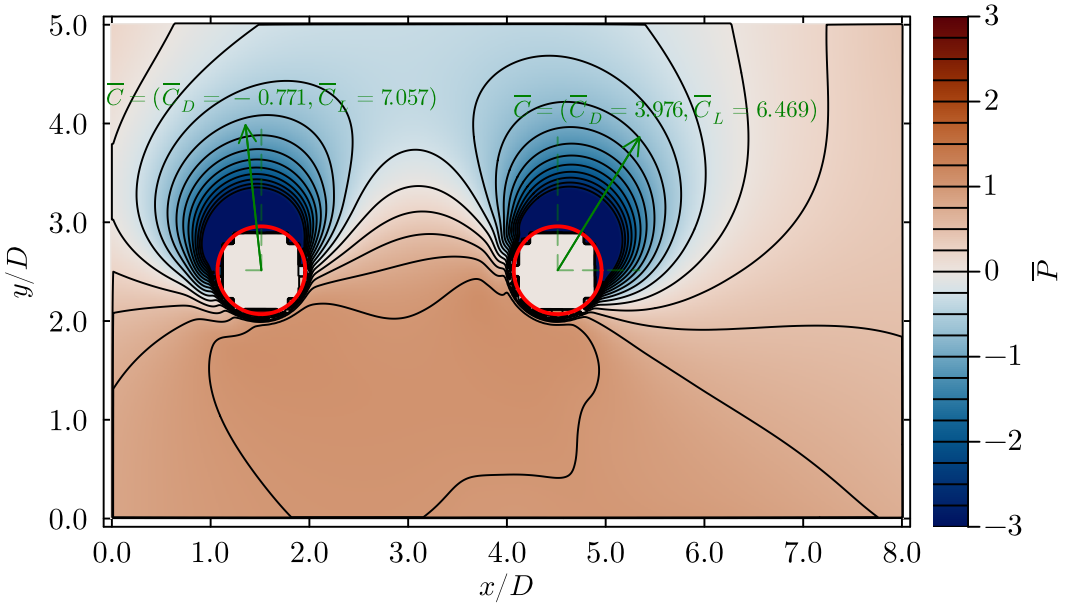

Figure 50: Time averaged pressure contours for $\lambda_1 = 4$, $\lambda_2 = 4$, $\theta = 0°$ $(z = 2D)$.

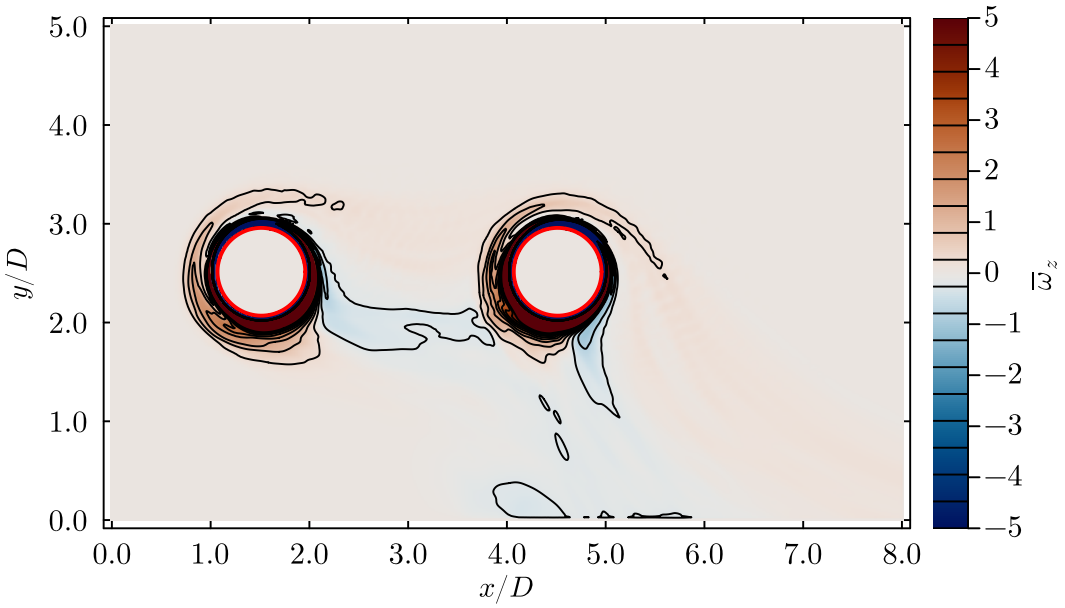

Figure 51: Time averaged z-vorticity contours for $\lambda_1 = 4$, $\lambda_2 = 4$, $\theta = 0°$ ($z = 2D$).

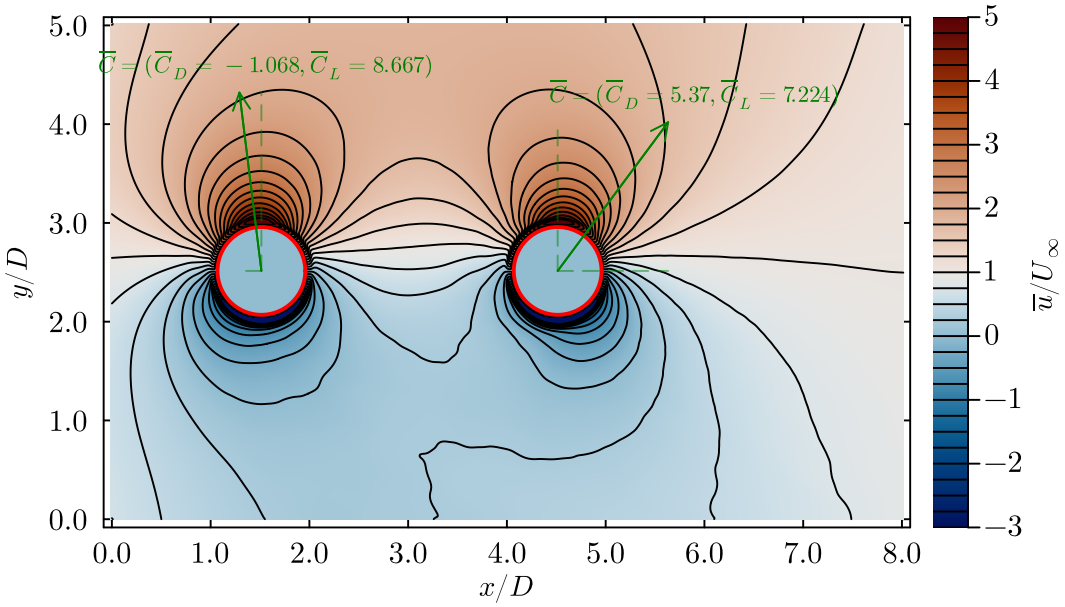

Figure 52: Time averaged streamwise velocity contours for $\lambda_1 = 5$, $\lambda_2 = 5$, $\theta = 0°$ ($z = 2D$).

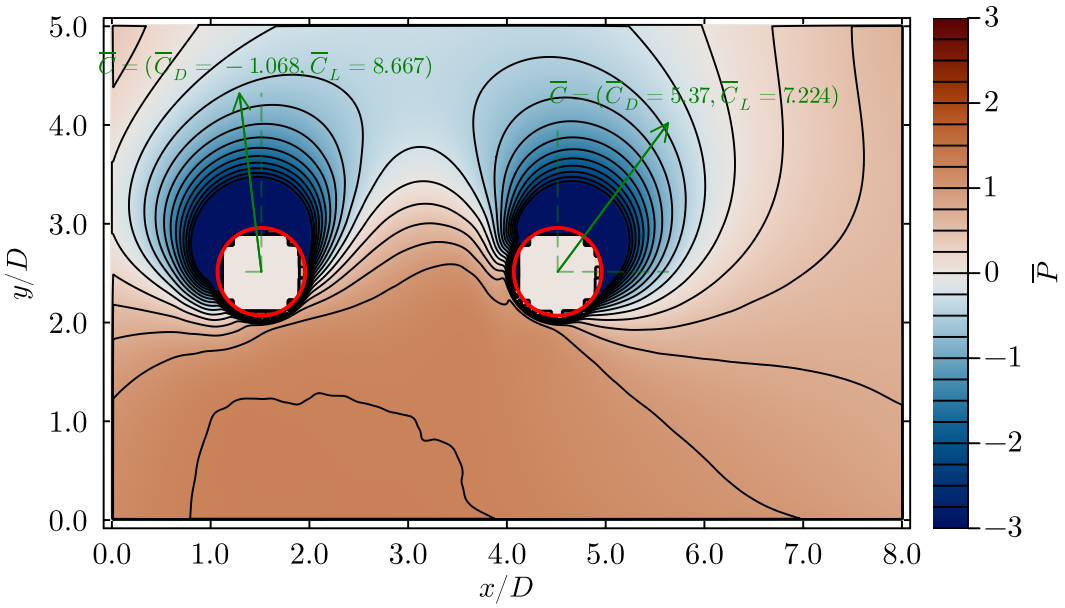

Figure 53: Time averaged pressure contours for $\lambda_1 = 5$, $\lambda_2 = 5$, $\theta = 0°$ ($z = 2D$).

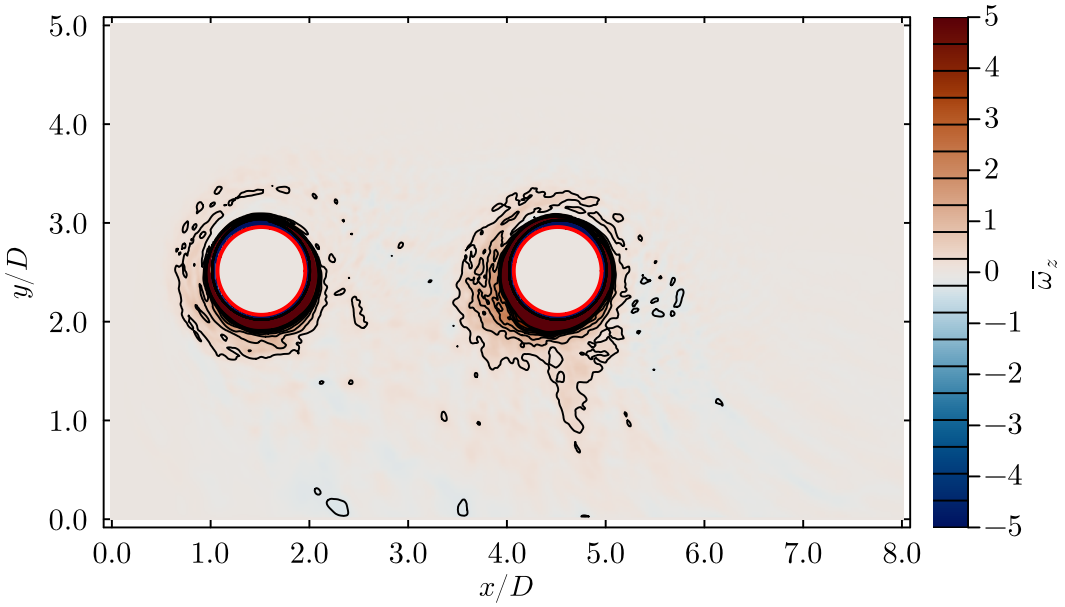

Figure 54: Time averaged z-vorticity contours for $\lambda_1 = 5$, $\lambda_2 = 5$, $\theta = 0°$ ($z = 2D$).

In order to determine the extent of the effect of the up-wash from the downstream cylinder on the thrust/drag force of the upstream cylinder two additional cases are presented, being ($\lambda_1 = 3$, $\lambda_2 = 5$, $\theta = 0°$) and ($\lambda_1 = 5$, $\lambda_2 = 3$, $\theta = 0°$) cases. The thrust force experienced by the upstream cylinder for the ($\lambda_1 = 3$, $\lambda_2 = 5$, $\theta = 0°$) case is higher than ($\lambda_1 = 3$, $\lambda_2 = 3$, $\theta = 0°$) because the up-wash from the downstream cylinder is higher for $\lambda = 5$. This can also bee seen by comparing the vorticity contours for both cases. As explained before, Figure 48 shows that the shear layers separating from the upstream cylinder is pushed upwards because of the up-wash. Figure 57 clearly shows that this up-wash is higher for ($\lambda_1 = 3$, $\lambda_2 = 5$, $\theta = 0°$) case and the displacement of the shear layers are higher. As a result, both shear layers reattach and completely wrap around the downstream cylinder. For the ($\lambda_1 = 5$, $\lambda_2 = 3$, $\theta = 0°$) case, the upstream cylinder no longer experiences thrust, although its drag remains reduced compared to the single-cylinder reference. This indicates that there is still considerable up-wash from the downstream cylinder, but it is insufficient to induce a large enough incidence angle to tilt the resultant force vector forward into thrust. Overall, the additional different rotation ratio cases can be consistently interpreted within the framework of the up-wash mechanism.

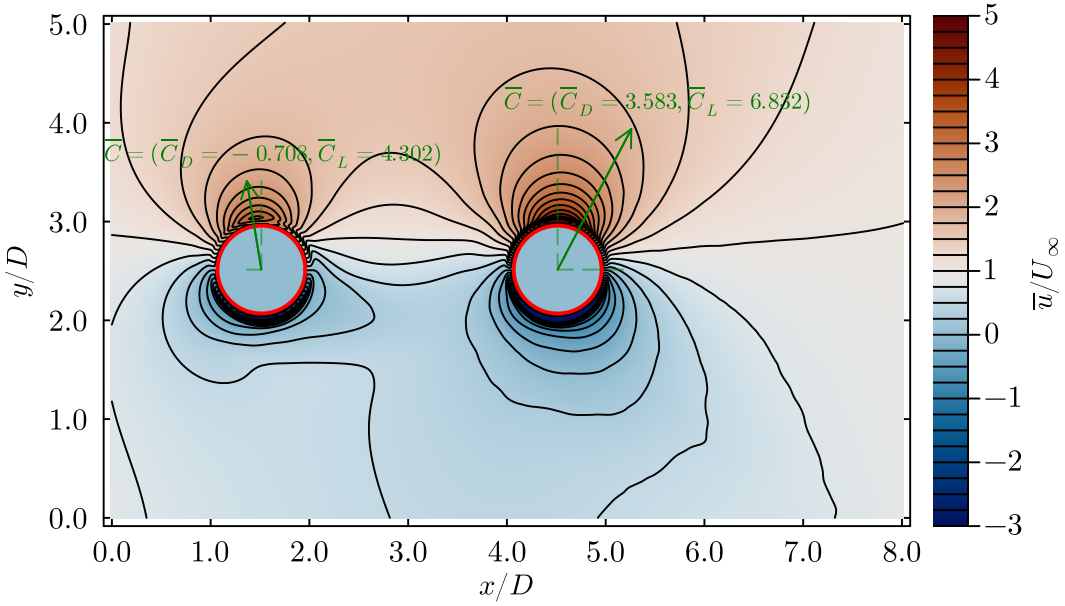

Figure 55: Time averaged streamwise velocity contours for $\lambda_1 = 3$, $\lambda_2 = 5$, $\theta = 0°$ ($z = 2D$).

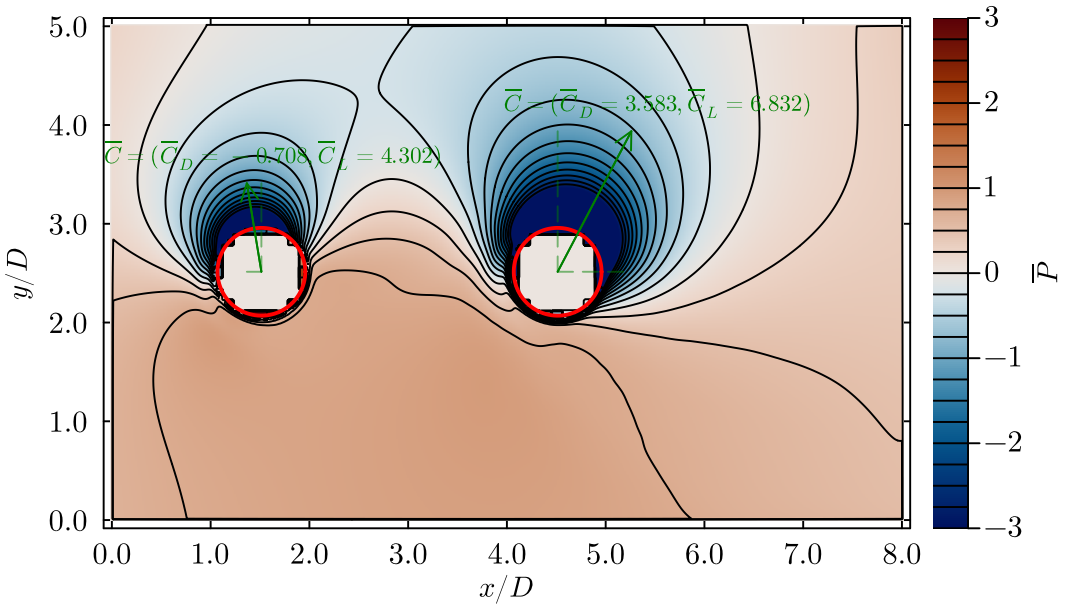

Figure 56: Time averaged pressure contours for $\lambda_1 = 3$, $\lambda_2 = 5$, $\theta = 0°$ ($z = 2D$).

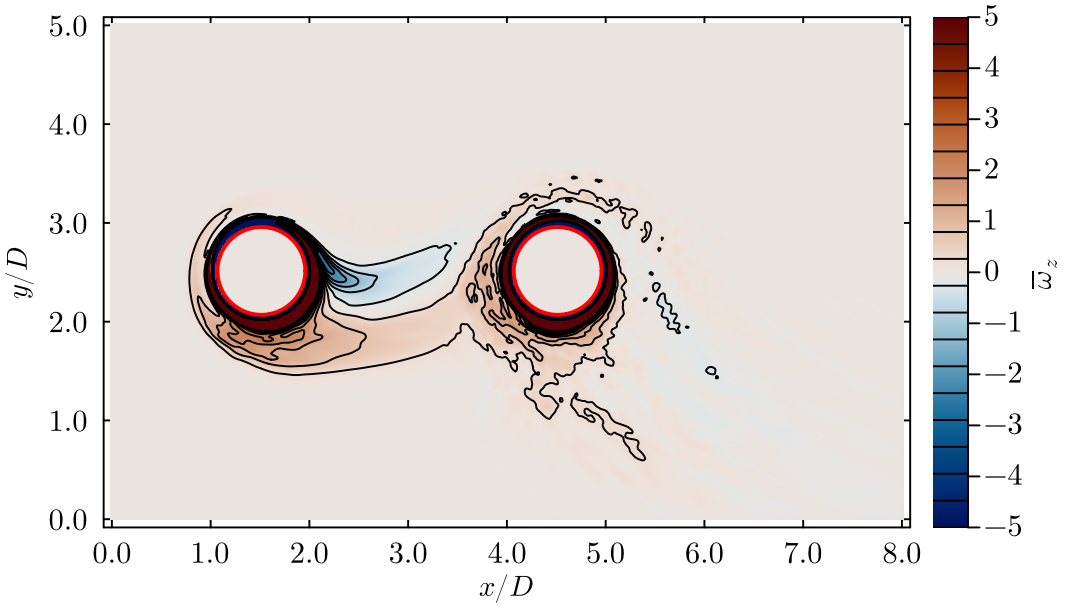

Figure 57: Time averaged z-vorticity contours for $\lambda_1 = 3$, $\lambda_2 = 5$, $\theta = 0°$ ($z = 2D$).

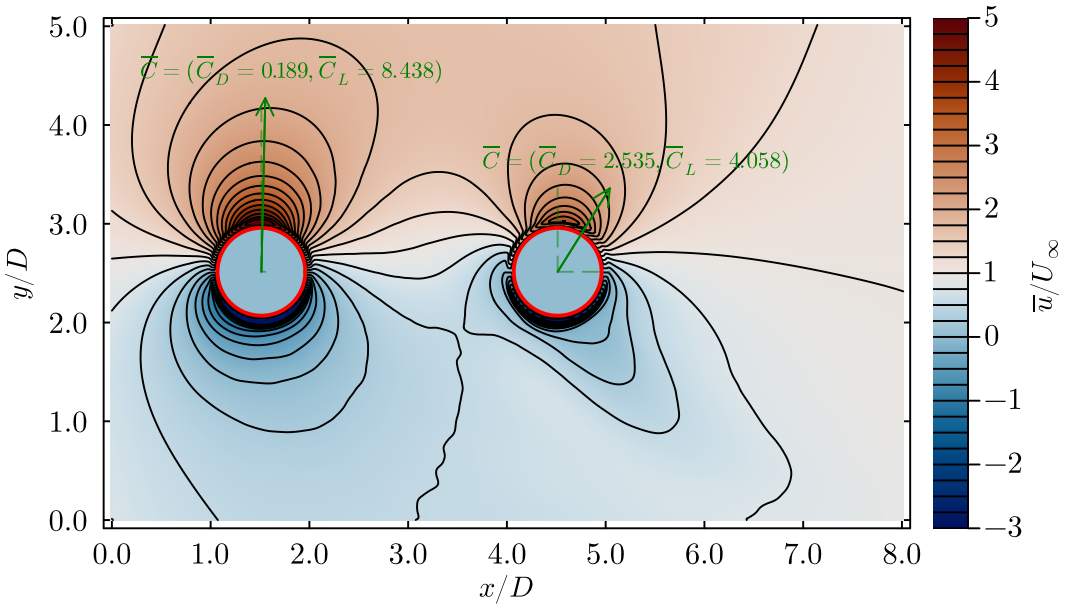

Figure 58: Time averaged streamwise velocity contours for $\lambda_1 = 5$, $\lambda_2 = 3$, $\theta = 0°$ ($z = 2D$).

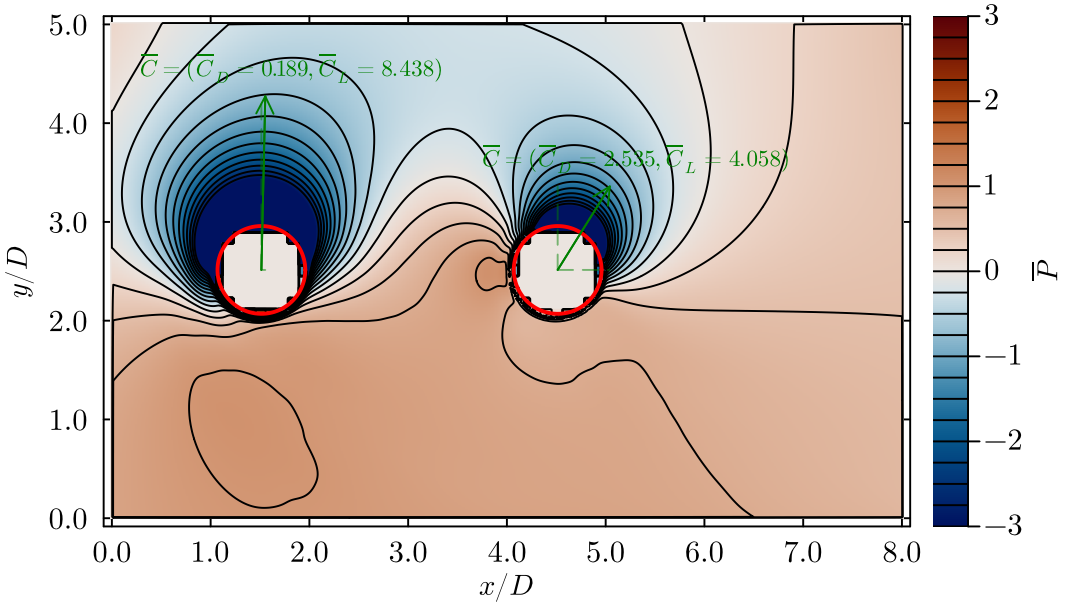

Figure 59: Time averaged pressure contours for $\lambda_1 = 5$, $\lambda_2 = 3$, $\theta = 0°$ ($z = 2D$).

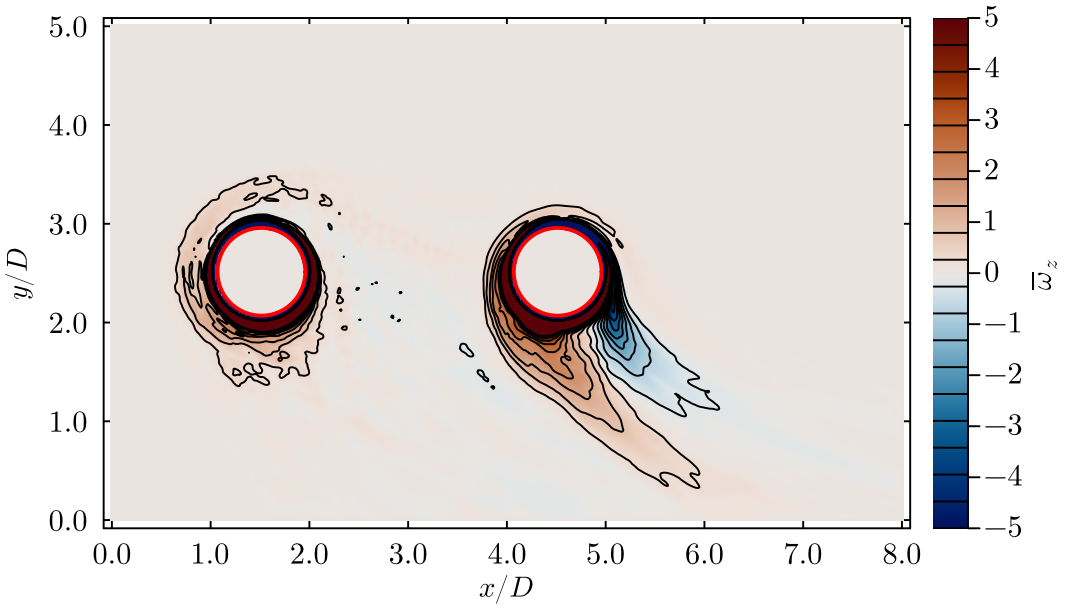

Figure 60: Time averaged z-vorticity contours for $\lambda_1 = 5$, $\lambda_2 = 3$, $\theta = 0°$ ($z = 2D$).

Finally, the flow field contours of a few additional cases with $\theta = 30°$ are presented below to provide an insight to the flow change with increasing incidence angle. The selected cases are ($\lambda_1 = 3$, $\lambda_2 = 3$, $\theta = 30°$), ($\lambda_1 = 3$, $\lambda_2 = 5$, $\theta = 30°$) and ($\lambda_1 = 4$, $\lambda_2 = 3$, $\theta = 30°$). The probe statistics for each case can be found in Appendix B It is imperative to note from the $\overline{\omega}_z$ contours for each case presented below, the steady shear layer shapes around each individual cylinder is not much different from the cases with $\theta = 0°$. There is either two separate shear layers detaching from the cylinder or the shear layers both wrap around the cylinder and there is no separation similar to the no-incidence angle cases. However, the shear layers are rotated towards the bottom side of the domain because of the increased actual incidence angle and there is much less interaction between the wake of the upstream cylinder and the downstream cylinder itself. The re-attachment of separating shear layers from the upstream cylinder to the downstream one, shown in Figure 48 is not experienced by cases with $\theta = 30°$.

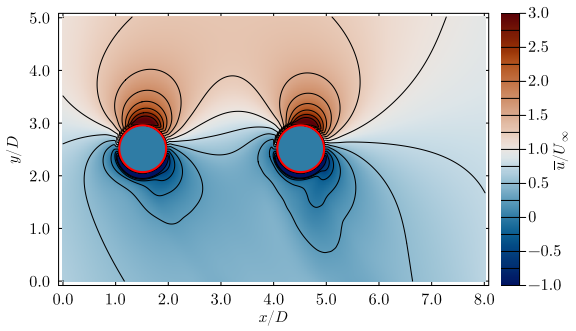

Figure 61: Time-averaged streamwise velocity contours for $\lambda_1 = 3$, $\lambda_2 = 3$, $\theta = 30°$ ($z = 3D$).

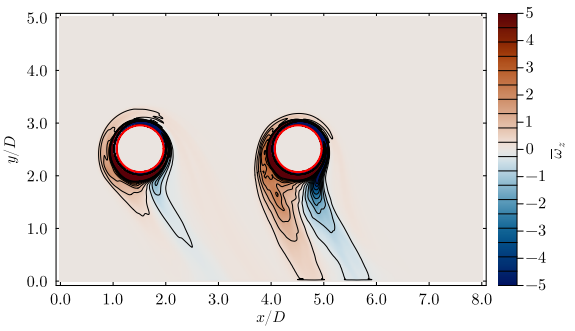

Figure 62: Time-averaged z-vorticity contours for $\lambda_1 = 3$, $\lambda_2 = 3$, $\theta = 30°$ ($z = 3D$).

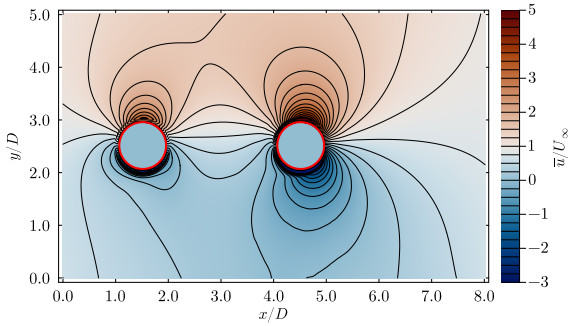

Figure 63: Time-averaged streamwise velocity contours for $\lambda_1 = 3$, $\lambda_2 = 5$, $\theta = 30°$ ($z = 3D$).

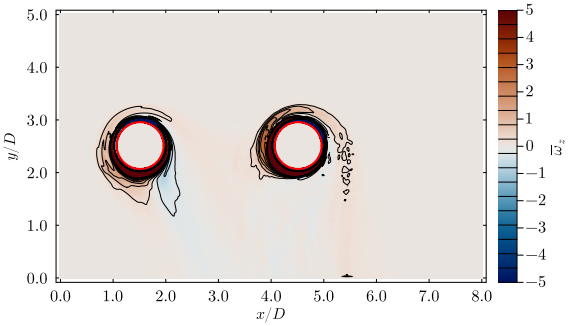

Figure 64: Time-averaged z-vorticity contours for $\lambda_1 = 3$, $\lambda_2 = 5$, $\theta = 30°$ ($z = 3D$).

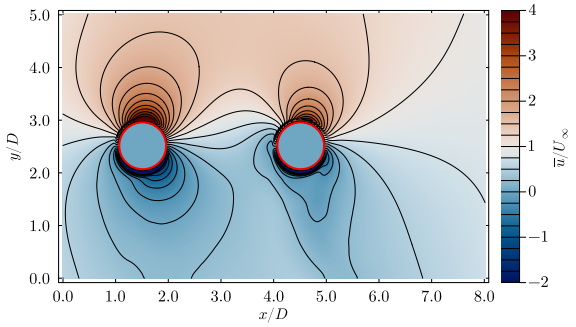

Figure 65: Time-averaged streamwise velocity contours for $\lambda_1 = 4$, $\lambda_2 = 3$, $\theta = 30°$ ($z = 3D$).

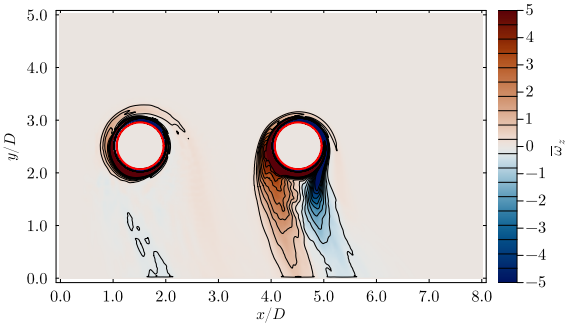

Figure 66: Time-averaged z-vorticity contours for $\lambda_1 = 4$, $\lambda_2 = 3$, $\theta = 30°$ ($z = 3D$).

4.4 Forces

The individual x and y-force coefficients are investigated in this section to get a grasp of how the rotation rate and wake-induced interactions effect each rotor. Figures 67, 68 & 69 show the force pairs for each rotor in each case with $\theta = 0°$, $\theta = 15°$ and $\theta = 30°$ respectively. The figures have x-force coefficients for individual rotors at x-axis and y-force coefficients on y-axis. The magenta and cyan colored dots show the forces on the upstream and downstream rotor for each case respectively. The dots are labeled with the value of the rotation rate on the upstream and downstream rotor respectively to indicate which case they belong to.

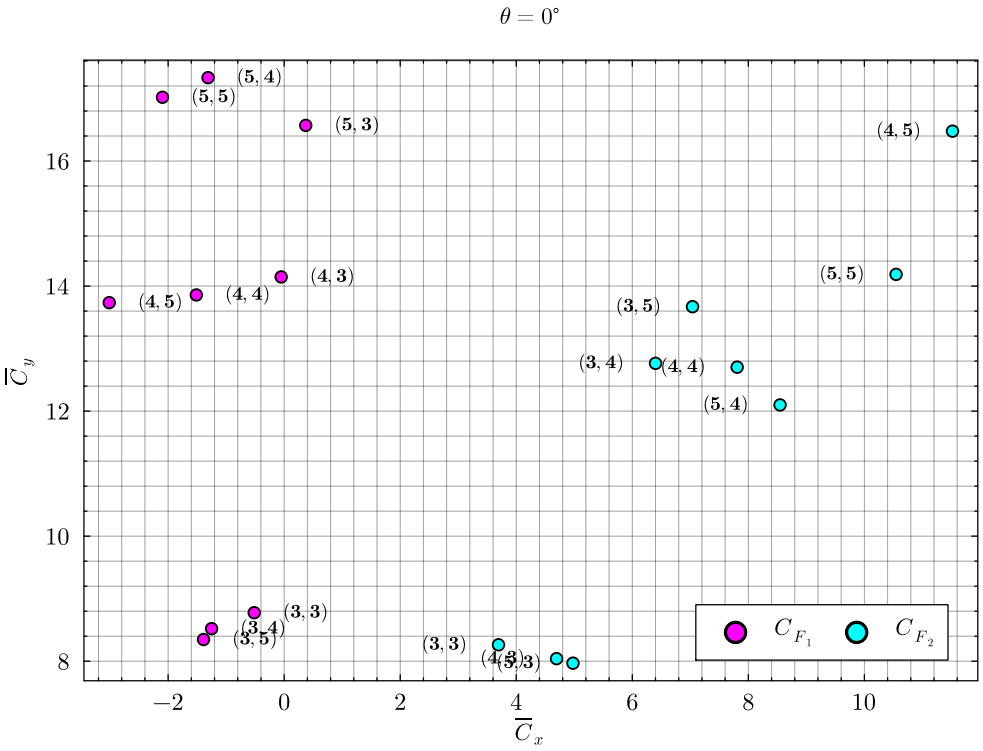

Figure 67: Force pairs for each case with $\theta = 0°$.

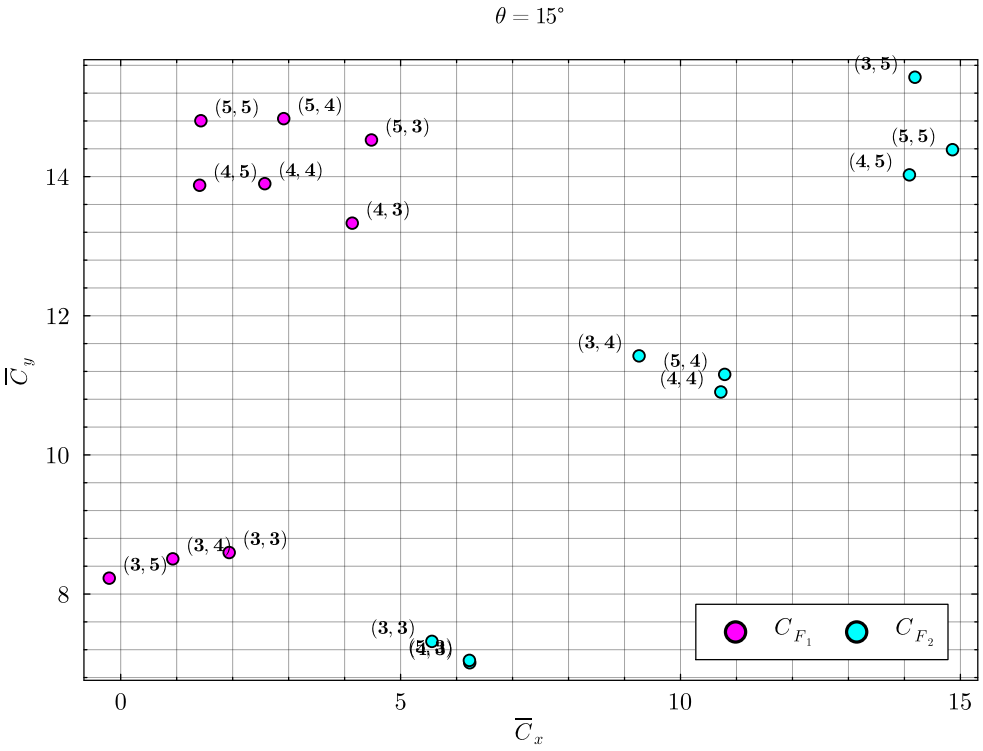

Figure 68: Force pairs for each case with $\theta = 15°$.

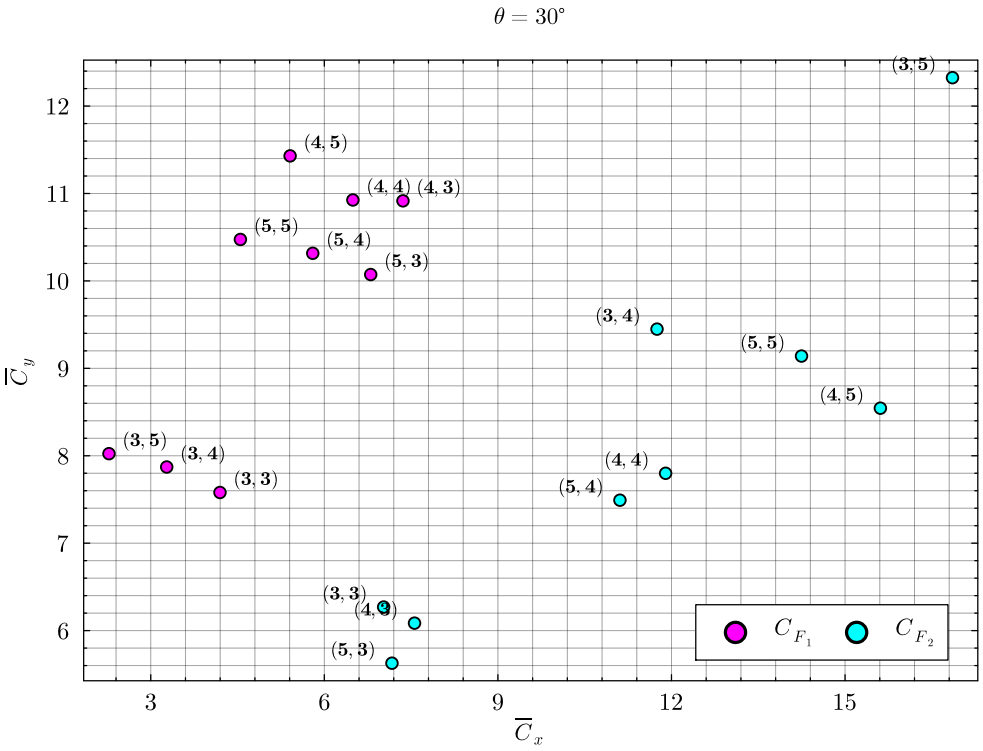

Figure 69: Force pairs for each case with $\theta = 30°$.

Figure 67, shows that the drag on the downstream cylinder is consistently higher for $\theta = 0°$. A clear trend is observed for $\lambda_2 \in [3, 4]$. As the rotation rate of the upstream cylinder increases, the drag on the downstream cylinder rises while its lift decreases. The upstream cylinder, on the other hand, experiences a net thrust for all configurations except for $(\lambda_1, \lambda_2) = (5, 3)$. For $\lambda_1 \in [3, 4]$, the thrust on the upstream cylinder increases and its lift decreases with increasing rotation rate of the downstream cylinder. A key observation explaining these behaviors is the cases with emergence of the induced incidence angle mechanism explained in Section 4.2. At $\theta = 0°$, the interaction between the rotors introduces an induced velocity field that modifies the local incidence angle on each rotor. The presence of the downstream rotor reduces the drag on the upstream rotor, while the up-wash generated on the upstream rotor can tilt the resultant force vector enough to produce a net thrust. Simultaneously, this up-wash slightly decreases the lift on the upstream rotor, with both effects intensifying as the downstream rotation rate increases. Conversely, the upstream rotor induces a down-wash that increases drag and reduces lift on the downstream rotor, with the magnitude of this effect also growing with increasing upstream rotation rate. The variation of these force components across different spin-ratio combinations can clearly be observed from Figure 67. For $\lambda_1 = 5$ cases, a similar increasing trend is observed in the thrust force on the upstream cylinder; however, the $(5, 4)$ configuration exhibits the highest lift among the three cases. For the $\lambda_2 = 5$ configurations, the $(4, 5)$ case results in the highest drag and lift on the downstream cylinder.

Figure 68 shows the behavior of the forces on the rotors exhibits characteristics from both $\theta = 0°$ and $\theta = 30°$ cases. For $\lambda_1 \in [3, 5]$ the upstream cylinder shows the same behavior on forces as the same cases with $\theta = 0°$ and for $\lambda_1 = 4$ the behavior is similar to the same cases with $\theta = 30°$. The force pairs for the downstream cylinder is much more predictable compared to their $\theta = 0°$ and $\theta = 30°$ as they are nicely bunched up in distinct areas of the Figure 68, showing less scattering.

Figure 69 shows the effect of the downstream cylinder is still highly influential on the forces of the upstream cylinder. It is observed that the behavior of the upstream cylinder is more predictable than $\theta = 0°$ cases. Each rotation rate $\lambda_1 \in [3, 4, 5]$ exhibits the same behavior of increasing lift and decreasing drag with increasing λ_2. This is due to the fact that the induced incidence angle from the downstream cylinder acts in favor of the actual incidence angle. However, the behavior of the downstream cylinder is much more chaotic than the $\theta = 0°$. Despite the relatively chaotic behavior of the drag and lift on the downstream cylinder, the lift force decreases with increasing λ_1 for almost all cases with $\theta = 30°$.

4.5 Proper orthogonal decomposition via the method of snapshots

Proper Orthogonal Decomposition (POD) is a widely used technique for extracting coherent structures from complex datasets, particularly in fluid mechanics. The essential idea is to represent a high-dimensional flow field using a reduced number of modes that optimally capture the energy of the system. Each POD mode corresponds to a spatial structure, while the associated coefficients describe the temporal evolution of that structure. Since flow simulations often produce very large datasets with high degrees of freedom (DoF), directly computing the eigendecomposition of the correlation matrix becomes computationally prohibitive. To overcome this, the method of snapshots, first introduced by Sirovich (1987), reformulates the problem so that the eigenvalue problem is solved in a much smaller subspace defined by the number of snapshots rather than the full spatial dimension. The method of snapshots is a computationally efficient procedure to compute the POD when the number of spatial degrees of freedom greatly exceeds the number of snapshots. Rather than forming and diagonalizing a huge spatial covariance matrix, it solves an eigenvalue problem in the space of snapshots. Mathematically, it is equivalent to the thin singular value decomposition (SVD) of the snapshot matrix, and it yields the same modes, singular (POD) values and temporal coefficients, but at a much lower computational cost when $M \gg N$. Note that the term "snapshot" is typically used for flow fields at consecutive time instances, however in this study the term snapshots is used for time averaged flow field data for each simulation in the simulation matrix presented in Section 3.3.

Let the data be arranged into a matrix of snapshots as Equation 4.13, where each column $\mathbf{u}_i \in \mathbb{R}^M$ is a time-averaged flow field (snapshot) sampled at different global parameters, M is the number of spatial degrees of freedom, and N is the number of snapshots.

$$X = \begin{bmatrix} | & | & & | \\ x_1 & x_2 & \cdots & x_N \\ | & | & & | \end{bmatrix} \in \mathbb{R}^{M \times N} \tag{4.13}$$

The correlation matrix of the snapshots is then defined as in Equation 4.14 in classical POD.

$$C = XX^T \in \mathbb{R}^{M \times M}. \tag{4.14}$$

The alternative formulation known as the method of snapshots constructs the correlation matrix from a collection of snapshots $x_{M,N}$ taken at discrete instances where typically $N \ll M$ and relies on solving an eigenvalue problem of a much smaller size $(N \times N)$ to find the POD modes. The number of snapshots (N) should be selected sufficiently large to capture the dominant variations in the flow field. Then, the reduced order eigenvalue problem can be defined as Equation 4.15

$$X^T X\psi_i = \lambda_i \psi_i, \quad \psi_i \in \mathbb{R}^M, \quad M \ll N \tag{4.15}$$

where $X^T X$ is of dimension $M \times M$, in contrast to the original problem of size $N \times N$. Although the smaller system is analyzed, both $X^T X$ and XX^T share the same nonzero eigenvalues, and their eigenvectors are related through a linear transformation. Once the eigenvectors (ψ_i) of the reduced system are obtained, the POD modes can be reconstructed using Equation 4.16

$$\phi_i = X\psi_i \frac{1}{\sqrt{\lambda_i}}, \quad i = 1 \in \mathbb{R}^M, \quad i = 1, 2, \ldots, N \tag{4.16}$$

Equation 4.16 can also be written in matrix form as Equation 4.17

$$\Phi = X\Psi\Lambda^{-1/2} \tag{4.17}$$

where $\Phi = \left[\phi_1^{(q)}, \phi_2^{(q)} \cdots \phi_N^{(q)}\right] \in \mathbb{R}^{M \times N}$ is the spatial modes and $\Psi = \left[\psi_1^{(q)}, \psi_2^{(q)} \cdots \psi_N^{(q)}\right] \in \mathbb{R}^{N \times N}$ is the mode coefficients.

The eigenvalue and singular value decompositions (SVD) are fundamentally interconnected. Specifically, the left and right singular vectors of a matrix $A \in \mathbb{C}^{m \times n}$ correspond to the orthonormal eigenvectors of AA^{-1} and $A^{-1}A$, respectively. Moreover, the nonzero singular values of A are equal to the square roots of the nonzero eigenvalues of these two matrices. Consequently, the singular values and vectors of A can be obtained by performing an eigenvalue decomposition on either AA^{-1} or $A^{-1}A$. In practice, the smaller of these two square matrices is typically selected to minimize computational cost, offering a more efficient alternative to computing the full SVD. This approach is particularly useful in flow field analyses, where the data matrix is often rectangular and highly dimensional in one direction. Then in matrix form, the snapshot matrix X can be decomposed with SVD as in Equation 4.18.

$$X = \Phi\Sigma\Psi^T \tag{4.18}$$

In Equation 4.18, $\Phi \in \mathbb{R}^{M \times M}$, $\Psi \in \mathbb{R}^{N \times N}$, and $\Sigma \in \mathbb{R}^{M \times N}$ with $N < M$. The matrices Φ and Ψ contain the left and right singular vectors of X, while Σ is a diagonal matrix holding the singular values $(\sigma_1, \sigma_2, \ldots, \sigma_N)$. The singular vectors Φ and Ψ correspond to the eigenvectors of XX^T and $X^T X$, respectively, and the singular values are related to the eigenvalues through $\sigma_i^2 = \lambda_i$. Therefore, performing the singular value decomposition (SVD) of X directly yields the POD modes Φ. It should be noted that the SVD provides Φ with a full size of $M \times M$, whereas the snapshot method yields Φ of size $M \times N$, retaining only the dominant N modes. Although the terms POD and SVD are sometimes used interchangeably in the literature, there is a conceptual distinction between them. SVD is a numerical decomposition technique applicable to rectangular matrices, whereas POD represents a broader decomposition framework for which SVD serves as one computational approach. While the snapshot method is computationally advantageous for large datasets, the SVD-based computation of POD modes is often preferred for its superior numerical robustness and reduced sensitivity to round-off errors.

Finally, the snapshot matrix can be approximated by a truncated expansion with r number of modes retained as in Equation 4.29.

$$X \approx \Phi\Lambda^{1/2}\Psi^T = \Phi\Sigma\Psi^T \tag{4.19}$$

Where, $\Phi = \left[\phi_1^{(q)}, \phi_2^{(q)} \cdots \phi_r^{(q)}\right] \in \mathbb{R}^{M \times r}$ is the truncated spatial modes, $\Psi = \left[\psi_1^{(q)}, \psi_2^{(q)} \cdots \psi_r^{(q)}\right] \in \mathbb{R}^{r \times r}$ is the truncated mode coefficients and $\Sigma = \left[\sigma_1^{(q)}, \sigma_2^{(q)} \cdots \sigma_r^{(q)}\right] \in \mathbb{R}^{M \times r}$ truncated singular values.

Note that for the present study, the snapshots are the time averaged flow fields for different global parameters so they are not exactly snapshots of an instantaneous fluid flow at different time instances. However, they will still be referred to as snapshots. On the contrary, the the temporal coefficients (ψ_i) will be referred to as POD coefficients. The first four spatial POD modes for the physical quantities of time-averaged streamwise velocity component ($q = \overline{u}_x$) and pressure ($q = \overline{P}$) are given as contour plots in Figure 70 through Figure 79. The energy content of each POD mode for each velocity component as well as pressure are given in Figure 82. The energy content of the each mode is calculated as in Equation 4.20 as the square of the singular value (σ_i).

$$e_k = \frac{\lambda_k}{\sum_{i=1}^{N} \lambda_i} = \frac{\sigma_k^2}{\sum_{i=1}^{N} \sigma_i^2} \tag{4.20}$$

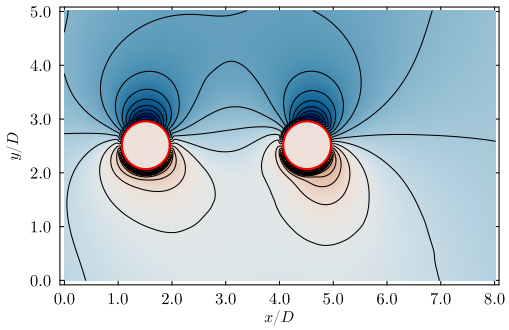

Figure 70: Spatial POD mode 1 for $\overline{u}_x$ at $z = 3.0D$.

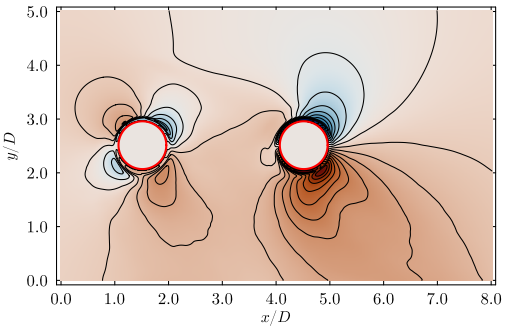

Figure 71: Spatial POD mode 2 for $\overline{u}_x$ at $z = 3.0D$.

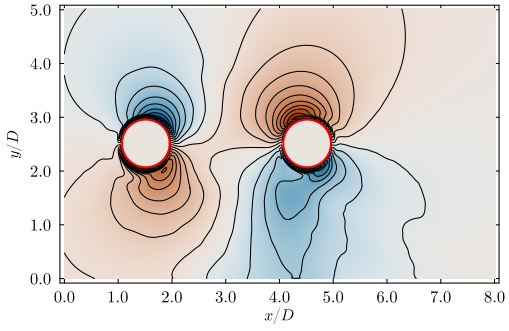

Figure 72: Spatial POD mode 3 for $\overline{u}_x$ at $z = 3.0D$.

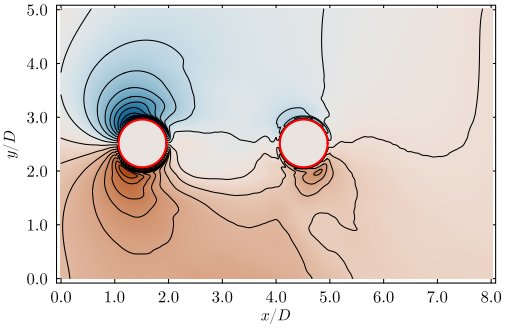

Figure 73: Spatial POD mode 4 for $\overline{u}_x$ at $z = 3.0D$.

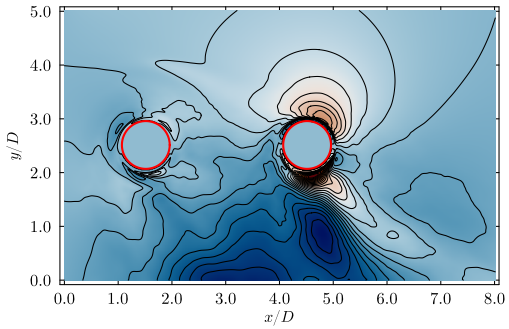

Figure 74: Spatial POD mode 5 for $\overline{u}_x$ at $z = 3.0D$.

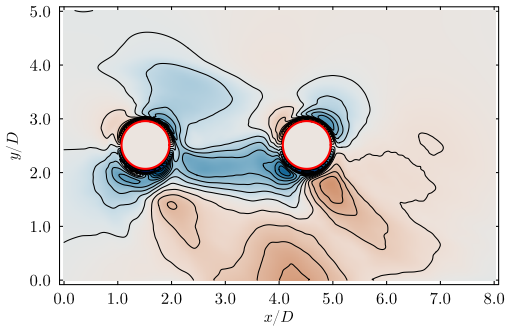

Figure 75: Spatial POD mode 6 for $\overline{u}_x$ at $z = 3.0D$.

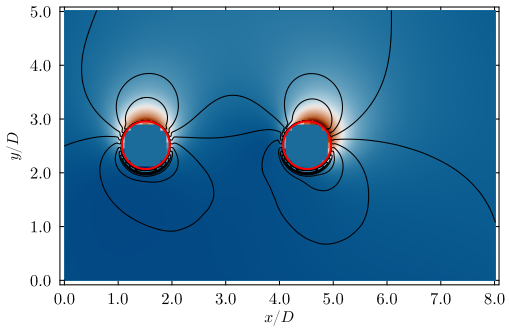

Figure 76: Spatial POD mode 1 for $\overline{P}$ at $z = 3.0D$.

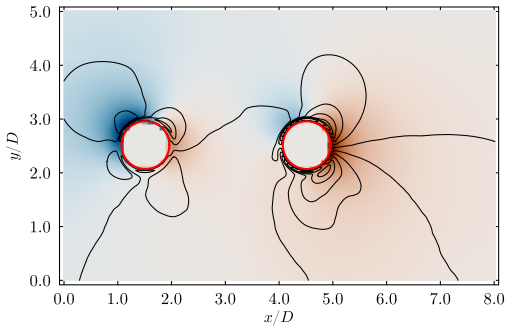

Figure 77: Spatial POD mode 2 for $\overline{P}$ at $z = 3.0D$.

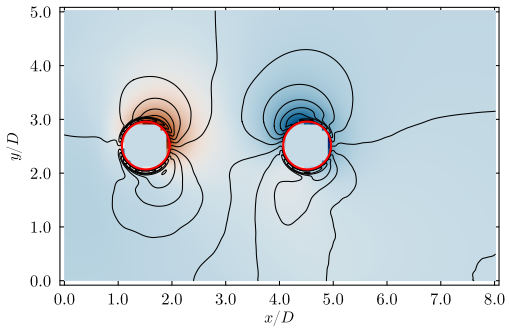

Figure 78: Spatial POD mode 3 for $\overline{P}$ at $z = 3.0D$.

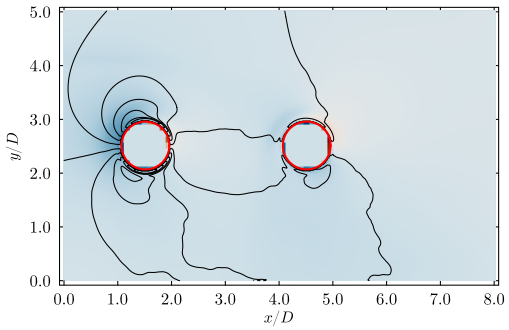

Figure 79: Spatial POD mode 4 for $\overline{P}$ at $z = 3.0D$.

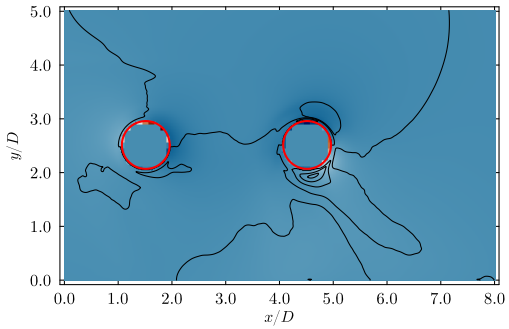

Figure 80: Spatial POD mode 5 for $\overline{P}$ at $z = 3.0D$.

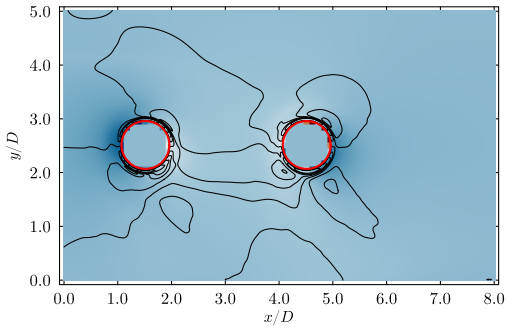

Figure 81: Spatial POD mode 6 for $\overline{P}$ at $z = 3.0D$.

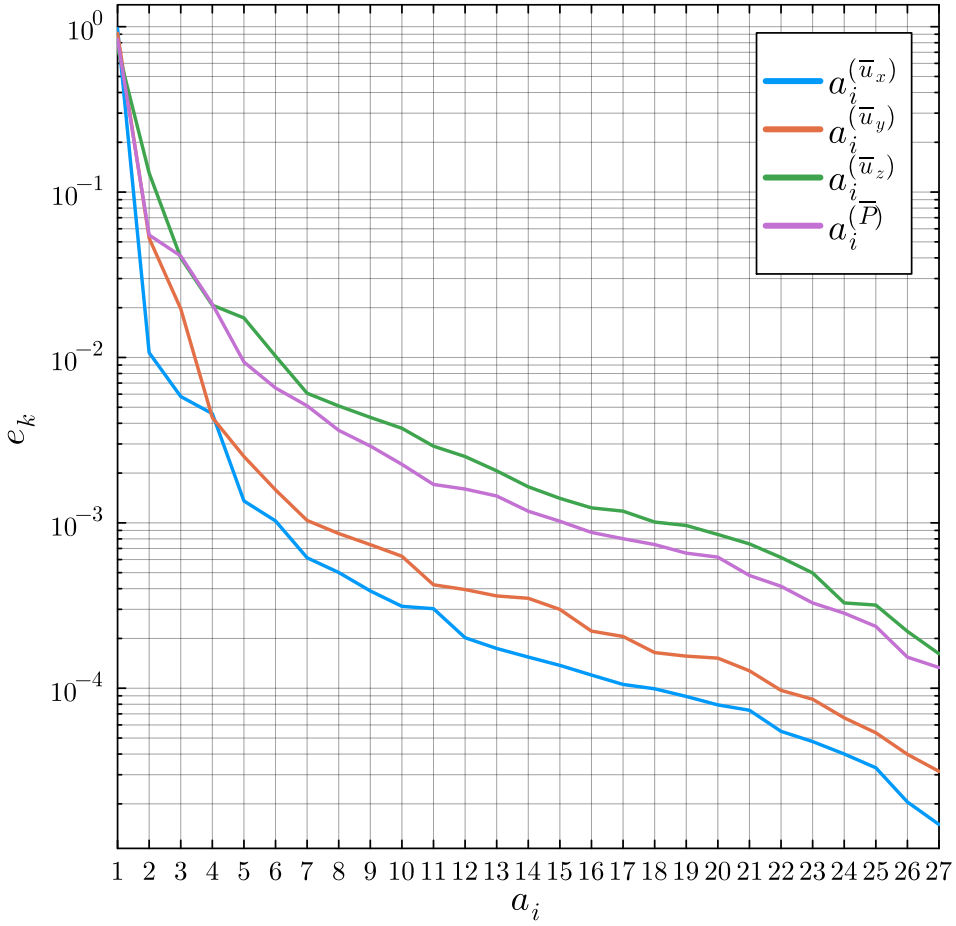

Figure 82: Energy content of each spatial mode for velocity components and pressure.

Figure 82 shows that the energy contained in each mode drops rapidly after the second mode and after the fourth mode, the contribution from each mode to the total flow property (physical quantity) is minimal for each velocity component and pressure after the fifth mode. This can also be seen from the spatial POD modes for $q = \overline{u}_x$. Figure 70 shows the first spatial POD mode for a z-slice at $z = 3.0D$ and greatly resembles the $\overline{u}_x$ contours for any of the global

parameters. The first mode is associated to the column-wise mean of the snapshot matrix (X). Figure 71, 72 & 73 shows the second, third and fourth spatial POD modes at the same z location, and they are strongly associated with the fluctuations from the mean mainly around the upstream and downstream cylinders. The fifth mode and the following spatial modes are strongly associated with the small frequency fluctuations around and away from both cylinders which can be observed from Figures 74 & 75. The same behavior is also followed by the pressure modes and other velocity component modes. Depending on the energy content of the spatial POD modes, the flow field can be reconstructed with the first 5 modes which corresponds to 99.54%, 99.19%, 95.19% and 96.69% of the total energy for $q = \overline{u}_x$, $q = \overline{u}_y$, $q = \overline{u}_z$ and $q = \overline{P}$ respectively.

4.6 Machine learning

The idea behind combining the results from POD with a simple deep neural network is to be able to quickly predict the time-averaged flow field around the rotors depending on changing global parameters. The POD coefficients are used to learn a map between the global parameters and the coefficients. As the coefficient matrix is much smaller than the full 3D flow field for the full dataset, this approach greatly reduces the time cost for training the ML algorithm and ensures faster convergence. However, faster convergence does not necessarily mean good training. The predicted POD coefficients and the full order predicted flow fields still have to be validated against the ground truth values.

Having reduced each flow field to a small set of POD coefficients, the central task is to learn how those coefficients vary with the global parameters of the configuration. In our problem the global parameters are the spin rate for the upstream (λ_1) and downstream (λ_2) cylinder and the angle of incidence (θ). These parameters are used as inputs for the neural network (NN) by creating a vector from their mathematical values as in Equation 4.21.

$$p = \begin{bmatrix} \lambda_1 \\ \lambda_2 \\ \theta \end{bmatrix} \in \mathbb{R}^3, \tag{4.21}$$

For each physical quantity $q \in \{\overline{u}_x, \overline{u}_y, \overline{u}_z, \overline{P}\}$ we have a truncated vector of POD coefficients dependent on the global parameters with r number of retained modes. Figure 82 shows the energy content of the spatial POD modes and as explained before in Section 4.5, the first five modes contain more than 95% of the total energy of the flow field for each physical quantity. Thus, the rest of the modes were truncated which results in a POD coefficient vector with five elements ($r = 5$) for each snapshot. Learning the parametric map $p \mapsto \psi_r^{(q)}(p)$ gives a fast surrogate which predicts the low-dimensional truncated POD coefficients first, then reconstructs the full flow field for each physical quantity linearly. Let the dataset contain N time-averaged global parameter cases (snapshots). From the POD (method of snapshots) we have, for each physical quantity quantity q, the truncated coefficient matrix is given as Equation 4.22

$$\Psi^{(q)}(p) = \left[\psi_1^{(q)}, \psi_2^{(q)} \cdots \psi_r^{(q)}\right] \in \mathbb{R}^{r \times r} \tag{4.22}$$

where $\psi_i^{(q)}$ is the column of coefficients for case $i = 1, 2, \ldots, N$. Importantly, the POD coefficients used in the training and validation sets include the singular-value scaling, as in Equation 4.23.

$$A = \Lambda^{1/2}\Psi^T = \Sigma\Psi^T \quad \in \mathbb{R}^{r \times r} \tag{4.23}$$

It is imperative to note that the training and validation sets are still referred to as POD coefficients for the rest of the section but these coefficients are the singular-value scaled coefficients ($A \in \mathbb{R}^{r\times r}$). For each $q \in \{\overline{u}_x, \overline{u}_x, \overline{u}_y, \overline{P}\}$ an independent multi-layer perceptron (MLP) is trained to find a map from the global parameters to the corresponding truncated POD coefficient matrix column ($a_i^{(q)}$) with r number of modes.

$$f_\theta^{(q)} : \mathbb{R}^3 \longrightarrow \mathbb{R}^r \tag{4.24}$$

After the sensitivity analysis explained in Section 3.5 was carried out for the type of activation function nHL and wHL, the best prediction quality is obtained with two hidden layers of width 64, including the input layer, a $GeLU$ non-linear activation function for each hidden layer and a linear output layer of width 3 across all physical quantities. The $GeLU$ activation function is given as $GeLU(x) = x \cdot \Phi(x)$ where $\Phi(x)$ is the cumulative distribution function of the standard normal distribution. Then the MLP can be defined as in Equation 4.25 where, Υ defines the array of trainable parameters, W_1 defines the input layer, W_2 defines the hidden layer and W_3 defines the linear output layer, z_n defines de affine map, h_n defines the non-linearity by $GeLU$ activation function and $a_\star$ defines output affine map. For each physical parameter, the same MLP structure is used. A simple schematic for the MLP structure is also presented in Figure 83.

$$f_\Upsilon^{(q)}(p) = W_3 GeLU\left(W_2 GeLU\left(W_1\, p + b_1\right) + b_2\right) + b_3 \tag{4.25}$$

$$\begin{aligned}
&\Upsilon = \{W_\ell, b_\ell\}_{\ell=1}^3 \\
&W_1 \in \mathbb{R}^{64\times 3}, \quad b_1 \in \mathbb{R}^{64} \\
&W_2 \in \mathbb{R}^{64\times 64}, \quad b_2 \in \mathbb{R}^{64} \\
&W_3 \in \mathbb{R}^{r\times 64}, \quad b_3 \in \mathbb{R}^{r} \\
&z_1 = W_1 p + b_1 \in \mathbb{R}^{64} \\
&h_1 = GeLU(z_1) \in \mathbb{R}^{64} \\
&z_2 = W_2 h_1 + b_2 \in \mathbb{R}^{64} \\
&h_2 = GeLU(z_2) \in \mathbb{R}^{64} \\
&a_\star = W_3 h_2 + b_3 \in \mathbb{R}^{r}
\end{aligned}$$

The POD coefficient vectors for each snapshot is split into into a training set and a validation set. This is achieved by keying each snapshot by its corresponding global parameters so tracking which snapshots are used for training and which for validation is possible later. Each column in the truncated coefficient matrix in Equation 4.22 corresponds to a snapshot. Each snapshot is indexed from 1 to N and arranged as separate arrays. The indexes are shuffled randomly and then the indexes thus the corresponding POD coefficient arrays are separated as training validation data with a 80% to 20% ratio respectively. Note that while determining the training and validation snapshots, the first two and last two snapshots on the snapshot matrix are always kept in the training set to ensure the extreme points in the parameter space are used in training. Each MLP ($f_\Upsilon^{(q)}$) is trained to minimize mean-squared error (MSE) on the truncated coefficients. The mean square error between the predicted POD coefficients and the ground truth values is given as Equations 4.27 & 4.27 for training and validation runs and is referred to as the loss function. Here $\mathcal{T}$ and $\mathcal{V}$ represents the number of training and validation snapshots respectively.

$$\mathcal{L}^{(q)}(\Upsilon) = \frac{1}{\mathcal{T}} \sum_{j \in \mathcal{T}} \left(f_{\Upsilon}^{(q)}(p_{i,tr.}) - a_i^{(q)} \right)^2 \tag{4.26}$$

$$\mathcal{L}^{(q)}(\Upsilon) = \frac{1}{\mathcal{V}} \sum_{j \in \mathcal{V}} \left(f_{\Upsilon}^{(q)}(p_{i,val.}) - a_i^{(q)} \right)^2 \tag{4.27}$$

Optimization problem for the loss function uses Adam optimizer with a learning rate of $\eta = 10^{-3}$, momentum for the mean $\beta_1 = 0.9$, decay for the variance $\beta_2 = 0.999$ and numerical stability $\epsilon = 10^{-8}$ and full-batch updates. An early-stop criteria on the improvement of the validation set errors is introduced to avoid over-fitting. The criteria is if the MSE of the validation set does not improve for a certain number of epochs (patience) the training is stopped and the trained coefficients are restored back to the ones giving the best MSE. The patience is selected to be 50 epochs. The normalized loss functions plotted against the number of epochs are presented in Figure 84 through Figure 87 for each physical quantity

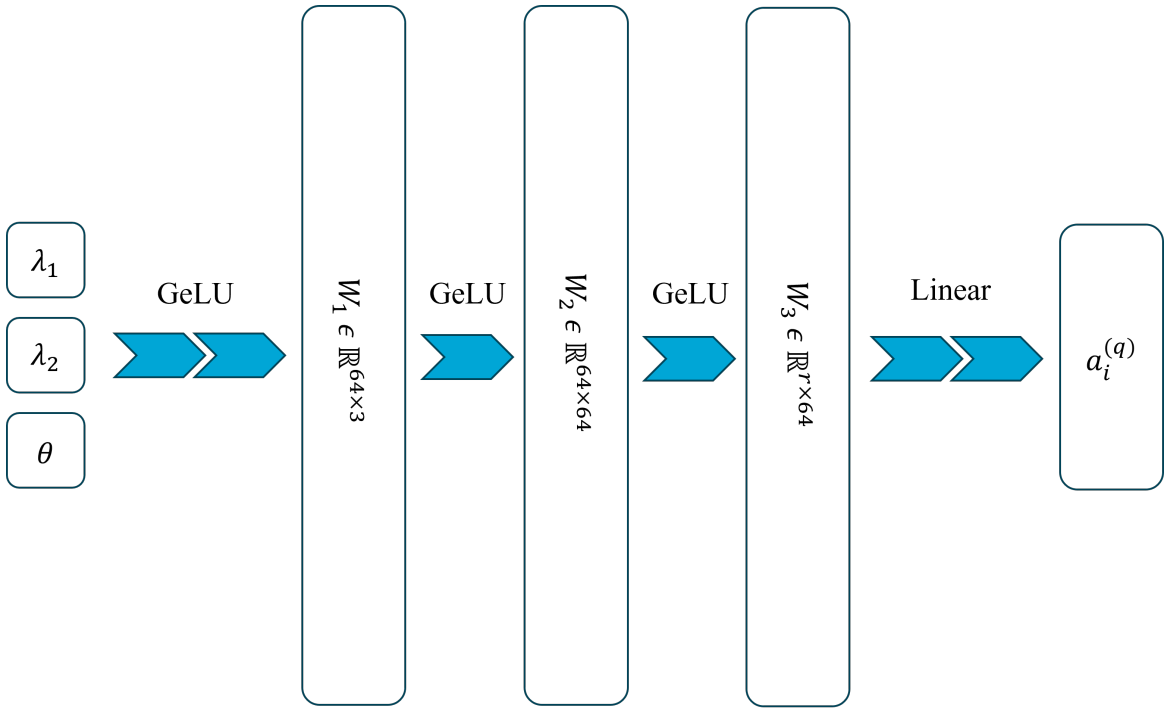

Figure 83: MLP schematic

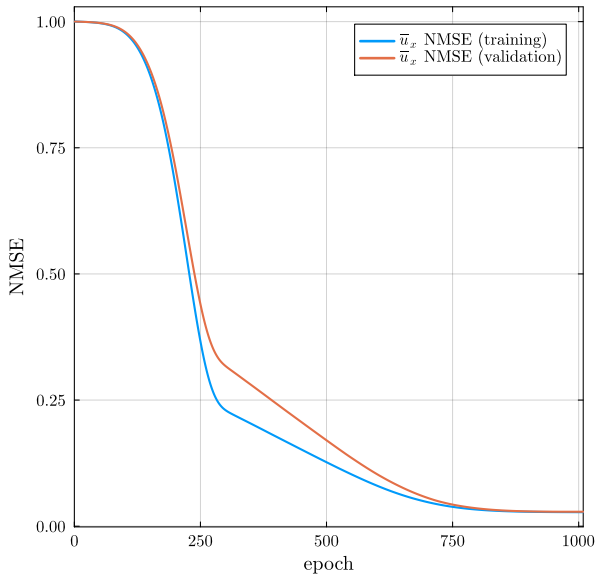

Figure 84: Loss function for $q = \overline{u}_x$.

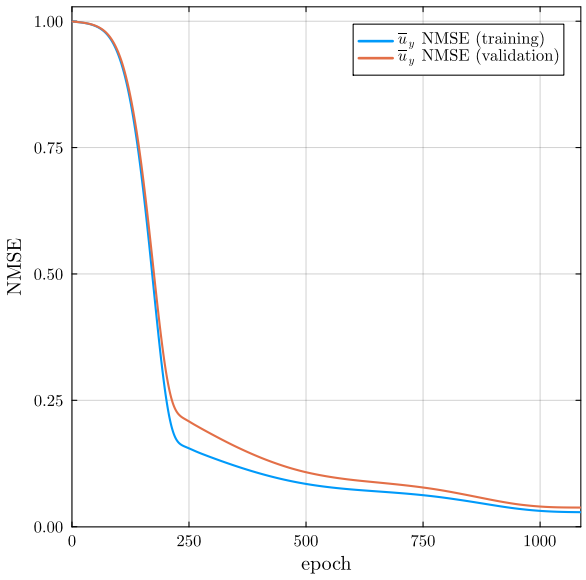

Figure 85: Loss function for $q = \overline{u}_y$.

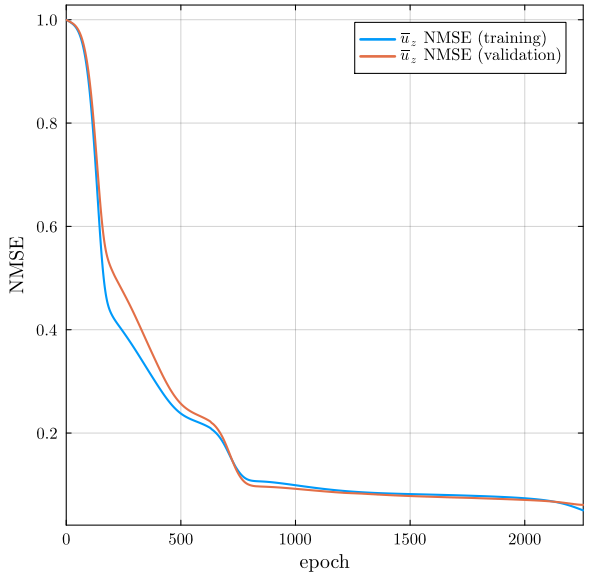

Figure 86: Loss function for $q = \overline{u}_z$.

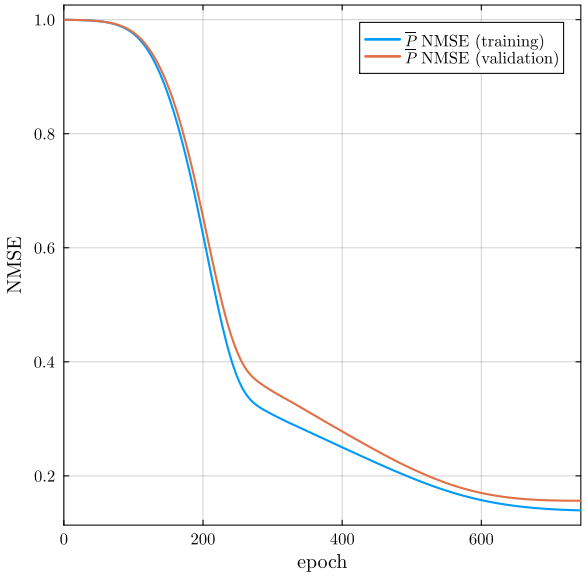

Figure 87: Loss function for $q = \overline{P}$.

The trend observed in each loss function is fast decrease until approximately $150 - 200$ epochs and stabilization after, which is a strong indication of a converged MLP result. In order to have an overview on the shape of the coefficient space and the prediction quality of the trained algorithm, each POD coefficient is predicted with the trained MLP and the space created by the predictions of the MLP is plotted on top of the ground truth space in Appendix D. The plotted surfaces are the sum of each truncated POD coefficient for each snapshot for constant inflow angle (θ).

To investigate the prediction quality of the MLP in detail, each predicted coefficient ($a_{\star,i}^{(q)}$) is plotted against the ground truth values ($a_i^{(q)}$) in a parity plot for each physical quantity

($q \in \{\overline{u}_x, \overline{u}_y, \overline{u}_z, \overline{P}\}$) from Figure 88 through Figure 91. The parity plots obtained during the sensitivity analysis are also presented in Appendix C to provide an insight on the capabilities of different MLP algorithms. The main problem encountered during this sensitivity analysis is for most MLP algorithms there is a bunching for the predicted coefficients around zero for different physical quantities indicating that the MLP algorithm struggles to properly learn and estimate the effect of global parameters on the POD coefficients. It is highly likely for those algorithms to return a value close to zero for varying input parameters making their out-of-training prediction quality quite low.

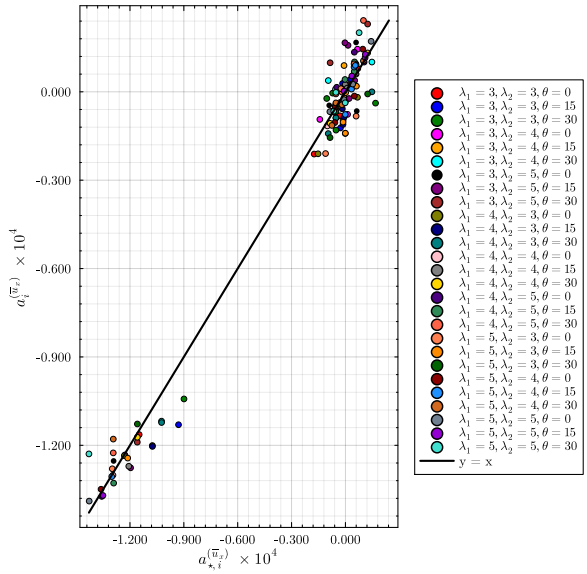

Figure 88: Parity plot of predicted and ground truth truncated POD coefficients for $q = \overline{u}_x$.

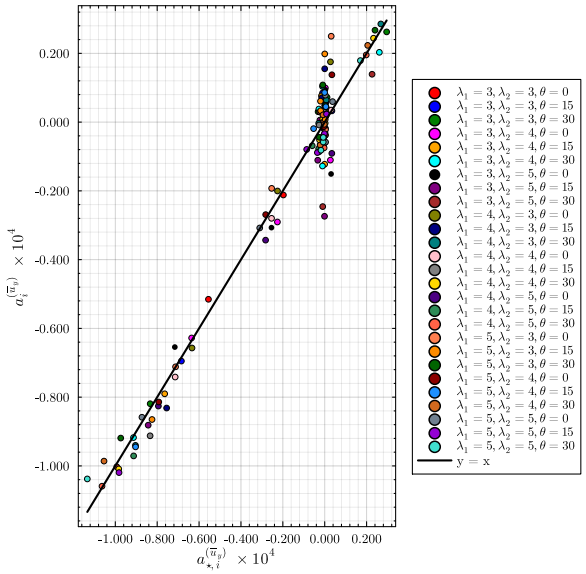

Figure 89: Parity plot of predicted and ground truth truncated POD coefficients for $q = \overline{u}_y$.

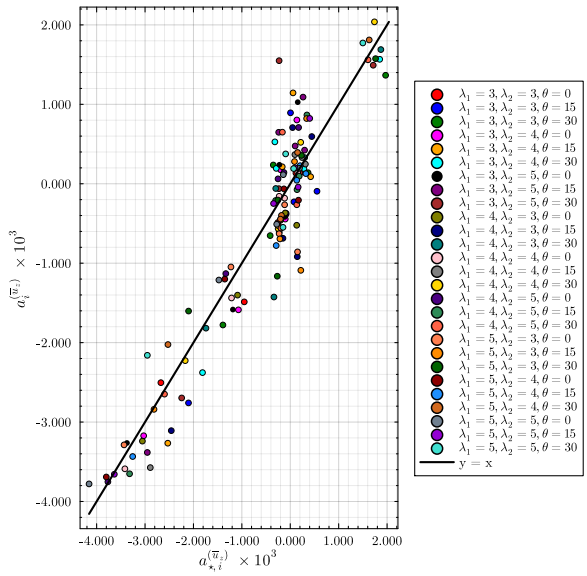

Figure 90: Parity plot of predicted and ground truth truncated POD coefficients for $q = \overline{u}_z$.

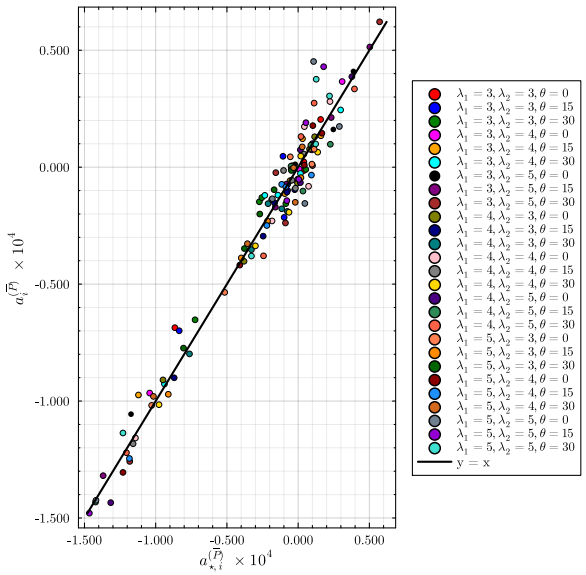

Figure 91: Parity plot of predicted and ground truth truncated POD coefficients for $q = \overline{P}$.

The best prediction is obtained for $q = \overline{P}$ as can be seen in Figure 91 as the scatter of the predicted coefficients is small. The parity plots for $q = \overline{u}_y$, $q = \overline{u}_y$ show that there is a bunching around the value of zero for the predicted coefficients, which indicates that the algorithm is not able to properly predict the relatively small changes in the POD coefficients and this results in a poor velocity field reconstruction. On the other hand, the algorithm performs relatively better for $q = \overline{u}_x$ where the bunching at the bottom and top parts of the parity plot presented in Figure 88 is a result of the ground truth POD coefficient values not the prediction.

As explained in Section 3.5, a probabilistic Bayesian regression (BR) algorithm is also considered in addition to the MLP-based neural network. The purpose of this regression model is identical to the neural network surrogate, namely to learn a functional mapping from the global parameters $(\lambda_1, \lambda_2, \theta)$ to the truncated set of POD coefficients. The same number of POD modes is retained ($r = 5$), and the training/validation split is kept consistent. The first and last two snapshots are always included in the training set, and 80% of all snapshots are used for training while the remaining 20% form the validation set.

The Bayesian regression approach provides an interpretable, uncertainty-aware alternative to the neural network, and is particularly suitable when the number of available snapshots is moderate. The surrogate model is formulated as a polynomial regression model embedded within a Bayesian framework. The input vector is the set of global rotor parameters. Before performing regression, the input vector is transformed using a polynomial feature expansion from scikit-learn library of Python. which generates all monomials of total degree up to d. This nonlinear basis significantly enriches the representational capacity of the model, enabling it to approximate complex dependencies between the inflow parameters and the corresponding POD coefficients introducing non-linearity in the regression and enabling the use of multi input/multi output regression. For each POD mode k, the regression model assumes the form given in Equation 4.28.

$$a_k = \mathbf{w}_k^\top \boldsymbol{\phi}(x) + \varepsilon_k, \qquad \varepsilon_k \sim \mathcal{N}(0, \sigma^2), \tag{4.28}$$

Here, $\mathbf{w}_k$ is the vector of regression weights to be inferred, ε_k are independent and identically normally distributed random variables and $\phi(x)$ is the input function with polynomial features obtained from the input array. For the prediction, Bayesian ridge regression with a multi level regressor is employed from the scikit-learn library. Bayesian ridge regression aims to compute the posterior distribution of the dataset and rather than estimating $\mathbf{w}_k$ via ordinary least squares (which is prone to overfitting), a Gaussian prior distribution is placed on the weights. This choice penalizes large weights and provides an automatic form of regularization. A sensitivity analysis is carried out on the degree of the input polynomial features. The best validation errors were obtained for polynomial features up to 4^{th} and by excluding the monomials obtained by multiplication of different global parameters. The parity plots for each physical quantity are given in Figure 92 through Figure 95. The prediction quality of the probabilistic algorithm is generally better for each physical quantity compared to the MLP algorithm as the scattering in the parity plots are significantly less.

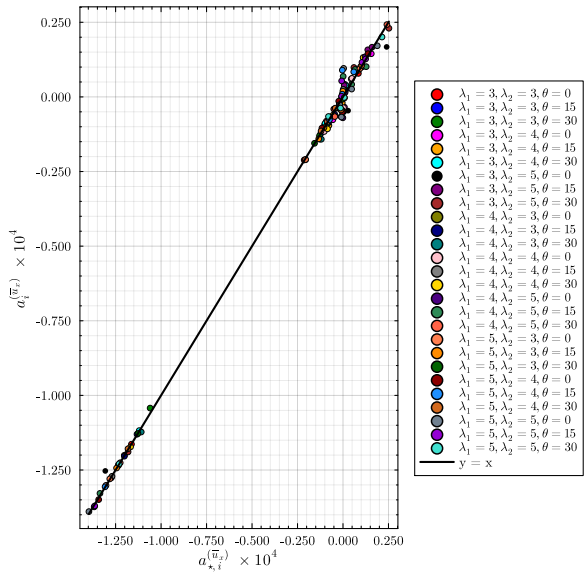

Figure 92: Parity plot of predicted and ground truth truncated POD coefficients for $q = \overline{u}_x$.

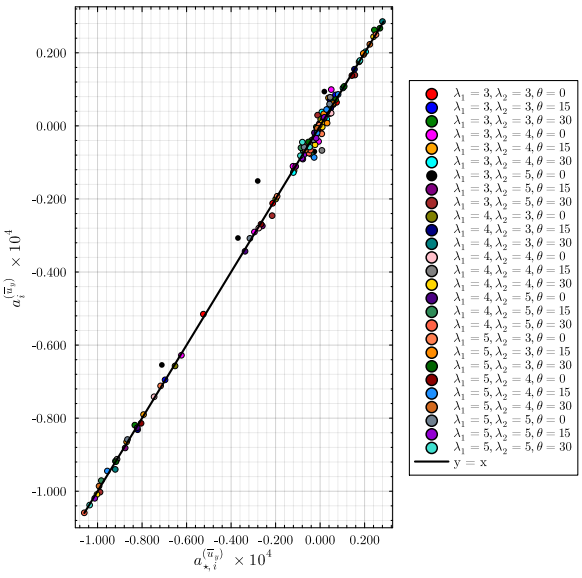

Figure 93: Parity plot of predicted and ground truth truncated POD coefficients for $q = \overline{u}_y$.

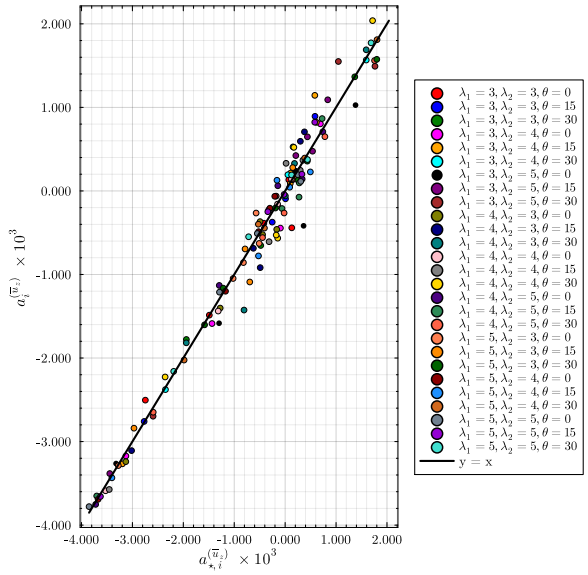

Figure 94: Parity plot of predicted and ground truth truncated POD coefficients for $q = \overline{u}_z$.

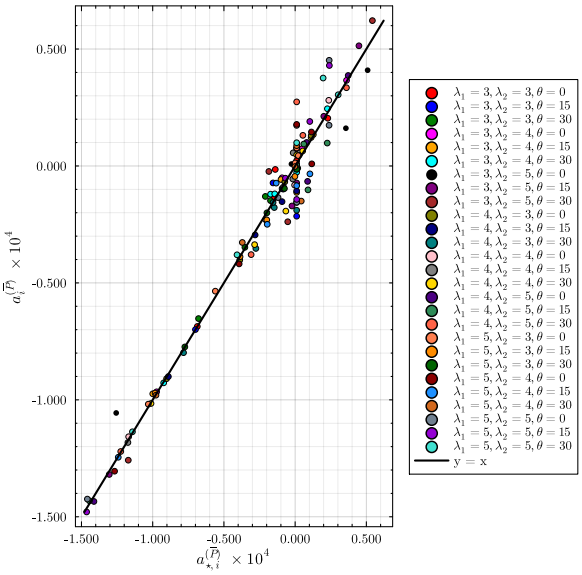

Figure 95: Parity plot of predicted and ground truth truncated POD coefficients for $q = \overline{P}$.

4.7 Flow field prediction

Once both surrogates are trained, predicting a full field for a global parameter set $p_\star$ takes two steps:

(i) Evaluate the networks to obtain the truncated coefficient vectors $a^{(q)}_{\star,i}(p_\star)$.

(ii) Form a linear combination of the precomputed spatial POD modes with the predicted POD coefficients.

The overall workflow of the POD-ML-based reduced-order model (ROM) is illustrated schematically in Figure 96, providing an overview of the steps undertaken in the preceding sections up to this point.

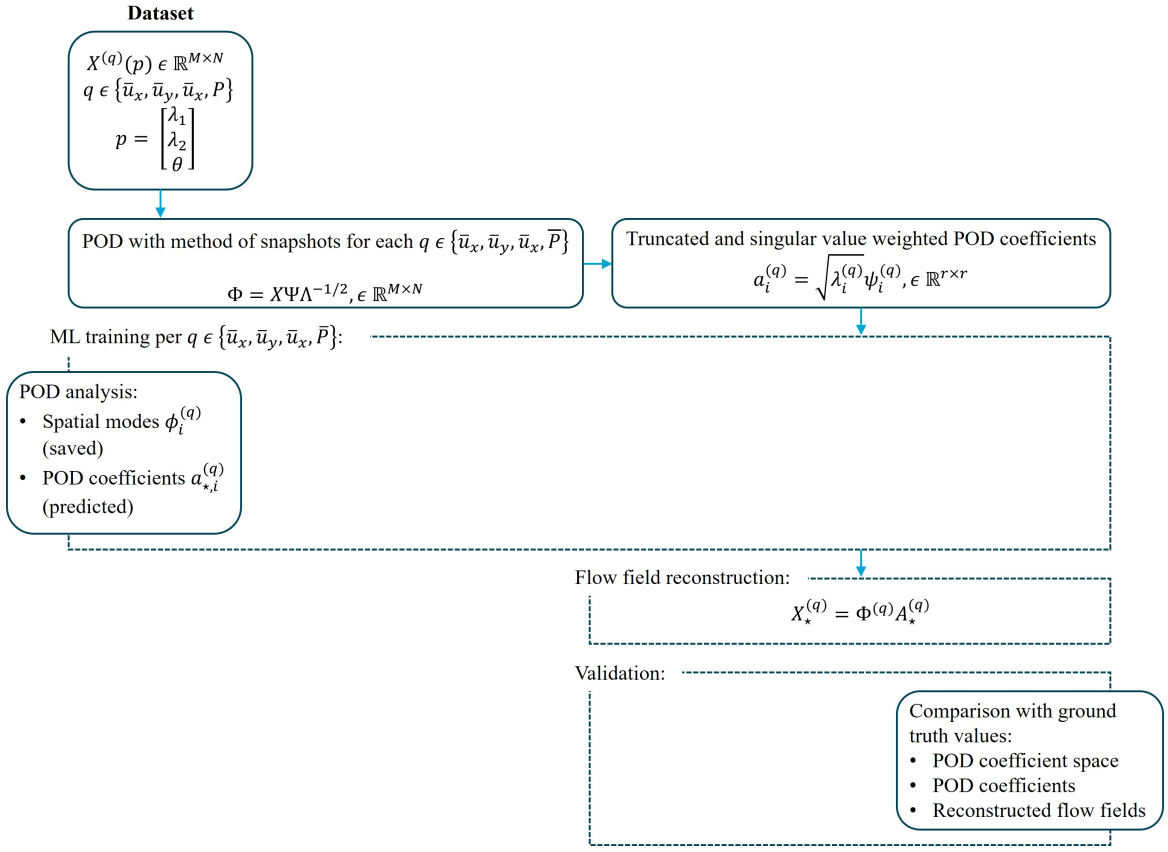

Figure 96: Workflow for the reduced order model (ROM).

For each physical quantity q the first $r = 5$ POD modes are retained. Each spatial POD mode for each $q \in \{\overline{u}_x, \overline{u}_y, \overline{u}_z, \overline{P}\}$ was saved to the disk after the POD analysis as vectors of length M (number of DOF in $3d$ computational grid). The modes are then read from the disk to reconstruct the full flow field with the predicted POD coefficients for global parameter array $p_\star$. Given $p_\star$. Then the full order flow field reconstruction can be done using the predicted POD coefficients and truncated spatial POD modes by multiplying the predicted coefficient array with the truncated spatial POD mode matrix as in Equation 4.29

$$x_{\star,i}^{(q)} = \phi_i^{(q)} a_{\star,i}^{(q)}, \quad X_\star^{(q)} \in \mathbb{R}^{M\times r}. \tag{4.29}$$

Finally the full order array of the predicted flow field in Equation 4.29 is reshaped to have the same dimensions as the $3d$ computational domain.

4.8 Truncation and prediction errors

For each parameter case the total error decomposes into the POD truncation error plus the coefficient-prediction error. By increasing the number of retained modes (r) reduces the truncation error by including more energy, but increases the regression difficulty and consequently increases the prediction error. In order to visualize the total error, the absolute error between the predicted and ground truth flow fields are calculated for each point in the computational

domain and presented as contour plots to assess the most problematic regions in the flow field for both algorithms. The mean square error for the whole domain is also indicated at the top of the contour plot for each physical quantity. The errors are given for a number of selected cases are presented at a slice at $z = 3D$ and for a selected case for various z locations in Appendix E. The absolute error can be calculated as the absolute value of the difference between the ground truth value and the predicted value as given in Equation 4.30.

$$AE = \left| x_i^{(q)} - \phi_i^{(q)} a_{\star,i}^{(q)} \right| \tag{4.30}$$

Then the mean squared error for the whole domain with M degrees of freedom (DOF) is calculated as in Equation 4.31

$$MSE = \frac{1}{M} \sum_{i=1}^{M} \left[x_i^{(q)} - \phi_i^{(q)} a_{\star,i}^{(q)} \right]^2 \tag{4.31}$$

It is clear from the figures in Appendix E that the most problematic flow region for both algorithms for any snapshot is the region immediately near the cylinders inside the low pressure region and the core of the low pressure region as well as the immediate wake of the cylinders.

In order to investigate the $3d$ flow field reconstruction quality of the POD-ML algorithm, $Q = 10^{-2}$ iso-surfaces are plotted for the cases with $\lambda_1, \lambda_2 \in [3]$. Figure 98 through Figure 102. Note that each reconstructed flow field uses the predicted POD coefficients from BR algorithm since it offers better prediction than the MLP. The quality of the reconstruction for each angle of incidence is generally quite high. The tip vortices from the end-plates are predicted rather well for all presented cases. The smaller vortical structured wrapping around the downstream cylinder as well as the so-called horse-shoe vortices at the bottom of both cylinders are predicted consistently well for each case. The biggest discrepancy between the reconstructed and ground truth flow fields is the absence of the vortical structures wrapping around the upstream cylinder in the reconstructed fields. Another discrepancy is the $\overline{\omega}_z$ values. They are consistently under-predicted through each case especially around the tip vortex from the end-plates. This is highly due to the fact that each velocity component being predicted by a separate algorithm and including independent errors. However, the overall velocity field prediction quality is still high since the reconstruction is able to capture the bigger scale vortical structures consistently.

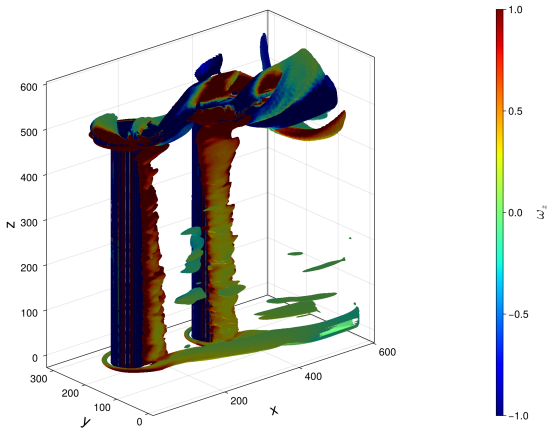

Figure 97: Q iso-surfaces ($Q = 10^{-2}$) colored by $\overline{\omega}_z$ for ground truth time-averaged velocity field for $\lambda_1 = 3$, $\lambda_2 = 3$, $\theta = 0°$.

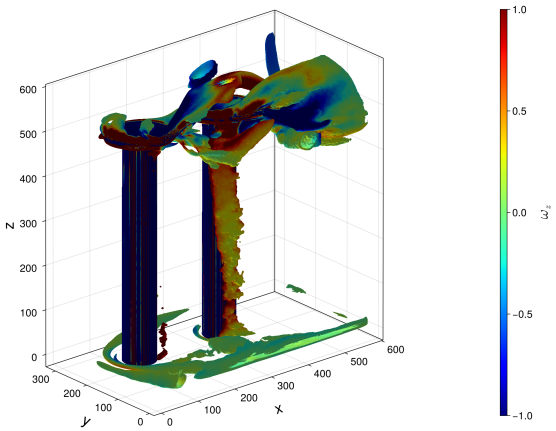

Figure 98: Q iso-surfaces ($Q = 10^{-2}$) colored by $\overline{\omega}_z$ for predicted time-averaged velocity field for $\lambda_1 = 3$, $\lambda_2 = 3$, $\theta = 0°$.

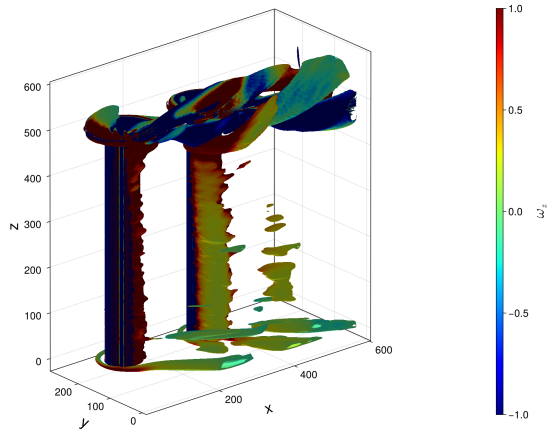

Figure 99: Q iso-surfaces ($Q = 10^{-2}$) colored by $\overline{\omega}_z$ for ground truth time-averaged velocity field for $\lambda_1 = 3$, $\lambda_2 = 3$, $\theta = 15°$.

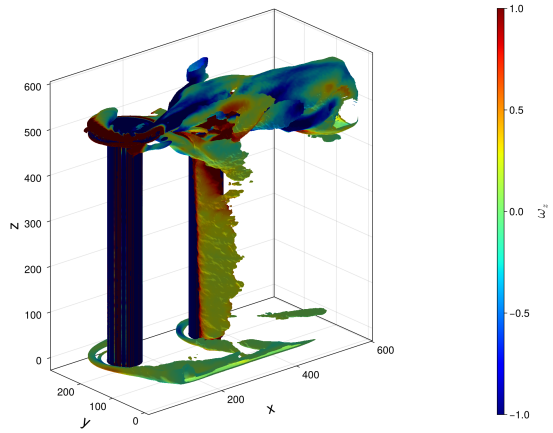

Figure 100: Q iso-surfaces ($Q = 10^{-2}$) colored by $\overline{\omega}_z$ for predicted time-averaged velocity field for $\lambda_1 = 3$, $\lambda_2 = 3$, $\theta = 15°$.

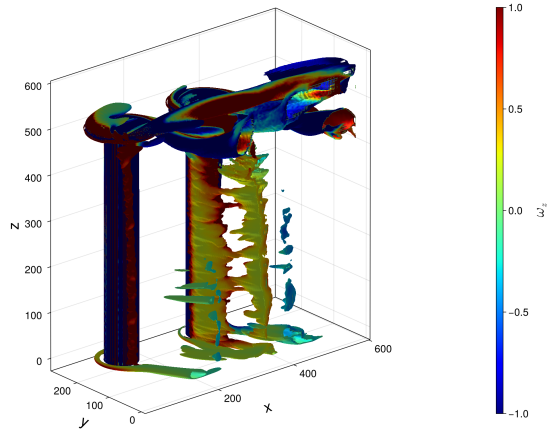

Figure 101: Q iso-surfaces ($Q = 10^{-2}$) colored by $\overline{\omega}_z$ for ground truth time-averaged velocity field for $\lambda_1 = 3$, $\lambda_2 = 3$, $\theta = 30°$.

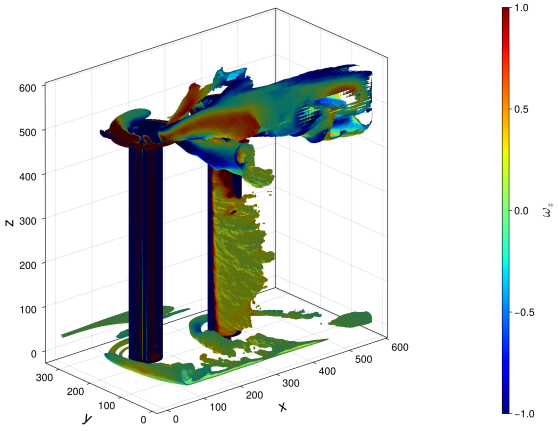

Figure 102: Q iso-surfaces ($Q = 10^{-2}$) colored by $\overline{\omega}_z$ for predicted time-averaged velocity field for $\lambda_1 = 3$, $\lambda_2 = 3$, $\theta = 30°$.

4.9 Force prediction

After the training is completed for both algorithms, being BR and MLP, the forces on the rotors are predicted by calculating the surface integrals on the rotors using the recovered flow field data. The force predictions from both algorithms are presented as parity plots against the ground truth force values in Figure 103 through Figure 106 for force predictions for the total force of the system. The parity plots for the individual rotor force coefficients can be found in Appendix F. The prediction quality on the lift and drag force coefficients is treated as the main assessment for the quality of the algorithm since it depends in the prediction quality of each physical quantity.

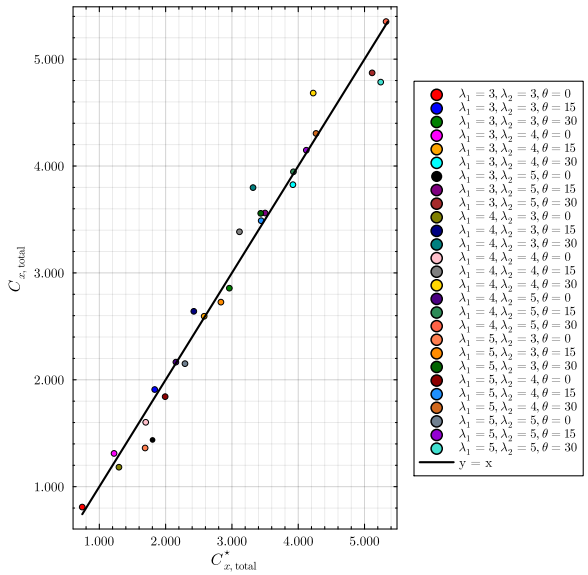

Figure 103: Parity plot of predicted and ground truth total $\overline{C}_x$ by BR.

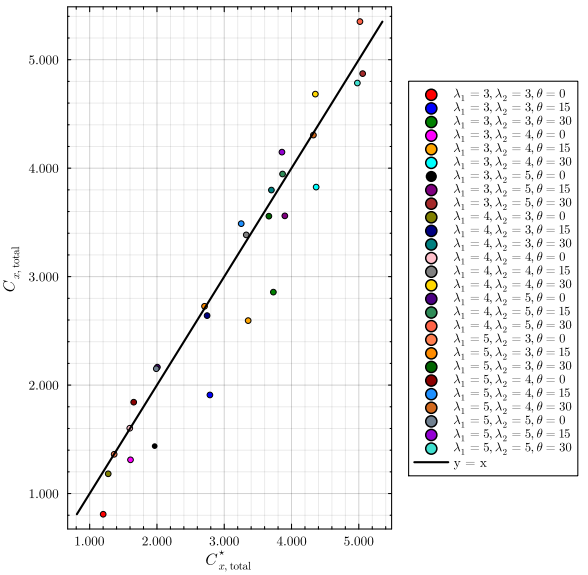

Figure 104: Parity plot of predicted and ground truth total $\overline{C}_x$ by MLP.

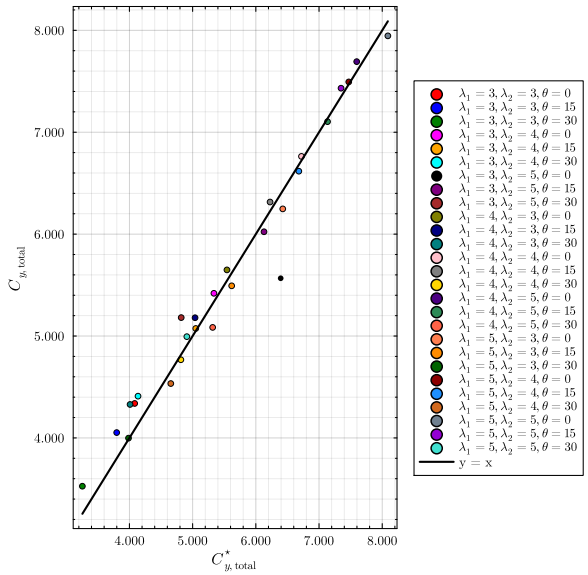

Figure 105: Parity plot of predicted and ground truth total $\overline{C}_y$ by BR.

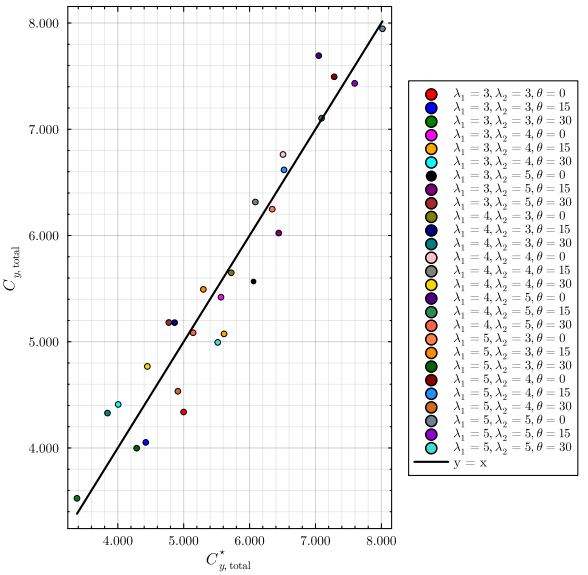

Figure 106: Parity plot of predicted and ground truth total $\overline{C}_y$ by MLP.

Overall, the parity plots show that the Bayesian ridge regression model exhibits noticeably less scattering around the one-to-one line compared to the MLP. This tighter clustering indicates that the BR predictions follow the ground-truth forces more consistently across the entire parameter space. The quantitative error metrics, namely MSE for force predictions for individual rotors and the total system, presented in Table 10 support this observation. The mean-squared errors for the BR model are generally lower for individual rotor force components. Furthermore, a particularly lower MSE is achieved for both total force coefficients of the system. Since these

total forces reflect the combined contribution of all recovered physical quantities, the improved performance of BR in predicting them demonstrates a more robust generalization capability, despite the model being significantly simpler than the MLP.

Table 10: MSE for force prediction for both algorithms.

	MLP	BR
$\overline{C}_{x_1}$	0.0424	0.0679
$\overline{C}_{x_2}$	0.0940	0.0546
$\overline{C}_{y_1}$	0.0816	0.0240
$\overline{C}_{y_2}$	0.0396	0.0514
$\overline{C}_{x}$	0.1337	0.0448
$\overline{C}_{y}$	0.1209	0.0526

5 Conclusion

This thesis has explored the wake-induced interactions of tandem Flettner rotors through a combination of high-fidelity CFD simulations, reduced-order modeling, and data-driven prediction techniques. The study aimed to deepen the understanding of the aerodynamic coupling mechanisms between rotating cylinders under varying operational and geometric conditions, and to develop an efficient framework capable of predicting these complex interactions. By integrating physical modeling, Proper Orthogonal Decomposition, and machine learning, the work provides both fundamental insights into the flow physics and practical tools for rapid flow field estimation. The following sections summarize the key findings, discuss their implications, and outline potential directions for future research.

5.1 Simulations

The simulation results presented in this thesis provided a comprehensive understanding of the aerodynamic interactions between tandem Flettner rotors under various operating conditions. The results closely reproduced the experimental observations of. In particular, the simulations revealed how changes in the spin ratios (λ_1, λ_2) and the relative incidence angle θ govern the flow regime transition and the wake-induced interactions between the two rotors. The cases examined at $\theta = 0^\circ$ demonstrated the fundamental mechanisms of wake interference, pressure distribution, and x-force modification resulting from the induced flow field of the rotors on one another.

A central finding of the simulations was the clear identification of the induced incidence angle mechanism acting between the rotors. When the incidence angle $\theta = 0^\circ$ the induced flow from the rotation of the cylinders to one another introduces a change in the x & y-force components on both cylinders. The presence of the downstream cylinder reduces the drag on the upstream cylinder and the up-wash is even able to tilt the total force vector enough to result in a thrust force. The same up-wash slightly reduces the lift on the upstream cylinder and this reduction in lift and drag is stronger when the rotation rate of the downstream cylinder is higher. The presence of the upstream cylinder on the other hand increases the drag force and reduces the lift of downstream cylinder since it introduces a down-wash. This behavior is also strengthened by the increase of the rotation rate of the upstream rotor. These change in force coefficients were presented in Section 4.4 in Figure 67. As for the cases with an actual

incidence, angle the induced incidence angle from the downstream cylinder works in favor of the actual incidence angle and increases the aerodynamic efficiency of the upstream rotor as can be seen form Figure 69. However, it is important to note that this up-wash mechanism does not significantly affect the total efficiency of the system, since the effect of the upstream cylinder on the downstream one, and vice versa, approximately cancel each other out. Also, the mechanism was explained in detail with a simplified potential flow approach in Section 4.2 and this approach was compared to the present study and previous works of Darvishyadegari and Hassanzadeh (2019), Rastan et al. (2021) and Siddiqui et al. (2024) in Figure 45. Finally, the flow fields presented in the same section illustrates how this induced motion alters both the flow topology and the aerodynamic forces. When a incidence angle of $\theta = 15°$ or $\theta = 30°$ is introduced as the inflow condition, the situation is markedly different. The circulation introduced by the upstream or downstream cylinder cannot overcome the incidence angle of the inflow condition and the force modifications become much harder to identify. In summary, the simulations confirmed that the aerodynamic coupling between tandem rotors is primarily governed by the competition between the up-wash and down-wash introduced by the rotation of each rotor onto one another.

5.2 Reduced order model

The Proper Orthogonal Decomposition (POD) approach employed in this work proved highly effective in capturing the dominant wake structures and their spatial organization around the tandem rotors. Even though the decomposition was performed using time-averaged flow fields across the parameter space a converged POD analysis could be obtained with as much as 27 snapshots as can be seen from Figure 82. The resulting modes successfully represented the coherent vortical patterns and the large-scale flow topology observed in the full CFD simulations. The low-dimensional reconstruction retained the higher portion of the energetic content of the flow with just the first few modes, demonstrating that the reduced basis extracted through POD provides a compact yet physically meaningful description of the wake dynamics. This confirms that the most energetic modes are sufficient to reproduce the overall wake deflection, and velocity deficit between the rotors with high fidelity, validating the suitability of POD for parametric analysis of complex rotor interactions.

For the machine-learning component, the multilayer perceptron (MLP) model trained on the POD coefficients was able to capture the underlying mapping between the global parameters $(\lambda_1, \lambda_2, \theta)$ and the modal amplitudes. The parity plots and coefficient-space comparisons against the ground truth and predicted values presented in Section 4.6 demonstrate that the network is able to learn the nonlinear structure of the prediction space and reproduce the general trends of the target data. However, small deviations and bunching around zero value for predicted POD coefficients for $q = \overline{u}_y$ and $q = \overline{u}_z$ indicates that the model performance is still limited. The probability based Bayesian regression (BR) model on the other hand offer much better prediction quality across all physical quantities. The model is able to achieve less reconstruction error for almost all snapshots and consequently, is able to produce better force prediction as explained in Section 4.9. Furthermore, as explained in Section 4.8, the BR algorithm is able to successfully reconstruct the $3d$ flow field consistently capturing the dominant, larger scale vortex structures around the rotors across all parameter space.

5.3 Recommendation for future work

While the present work provides valuable insight into the wake-induced interactions of tandem Flettner rotors and demonstrates the potential of reduced-order and data-driven modeling frameworks, several avenues remain open for further exploration and refinement. These are summarized below as recommendations for future studies.

The machine learning framework developed in this thesis can be further enhanced by embedding physical constraints into the neural network training process. Physics-Informed Neural Networks (PINNs) can enforce the Navier–Stokes equations as soft constraints during training, ensuring that the predicted flow fields satisfy mass and momentum conservation. Integrating PINNs with the POD representation could improve the physical consistency of the predicted flow fields, reduce the need for large datasets, and increase robustness when extrapolating to new operating conditions. Such hybrid models would be especially powerful for real-time flow prediction or control-oriented applications. In addition, if Physics-Informed Neural Networks (PINNs) are incorporated into the reduced-order modeling framework, an important advantage would be the possibility of reliably recovering the pressure field directly from the predicted velocity fields. Because PINNs embed the governing equations, including incompressibility and the momentum balance, into the learning process, the reconstructed flow fields inherently producing a divergence free velocity field. This would significantly reduce the numerical errors typically introduced when solving the Poisson equation for pressure recovery in post-processing. As a result, the pressure distribution and consequently the aerodynamic force coefficients could be predicted more accurately. Such an approach would further increase the fidelity and physical reliability of the surrogate model.

The present simulations were conducted at moderate Reynolds numbers to maintain numerical stability and reduce computational cost. Future work should explore higher and more realistic Reynolds number regimes that better represent full-scale rotor operation. At such conditions, the wake dynamics become more turbulent and three-dimensional. Expanding the dataset to these regimes would also enable more representative training of the reduced-order machine learning models.

The current study focused on a fixed gap ratio between the rotors. Investigating a wider range of spacing configurations would allow for a better understanding of the sensitivity of wake interactions to rotor proximity. Particularly, studying both smaller and larger gap ratios could help identify thresholds for aerodynamic coupling and performance degradation. In addition, incorporating different geometric features such as aspect ratio variations, could provide insight into design optimization for multi-rotor systems.

Another promising direction is to extend the framework toward fully coupled fluid-structure interaction (FSI) simulations, where the structural flexibility or vibration of the rotor system interacts with the flow field. Such simulations would provide a more comprehensive understanding of aero-elastic behavior and help assess the structural response of rotor systems under unsteady aerodynamic loading.

Finally, the machine learning models developed here could be integrated into optimization and control frameworks to actively tune the spin rates of the rotors for performance maximization. Combining the reduced-order modeling approach with reinforcement learning or optimal control strategies could enable real-time adjustments of operating parameters to achieve desired thrust or efficiency targets under varying inflow conditions.

In summary, future work should focus on expanding the physical scope of the current modeling framework, integrating physics-based learning approaches, and exploring more realistic flow conditions and different geometric configurations. These steps would not only strengthen the predictive capability of the proposed methodology but also bridge the gap between simulation-based research and practical multi-rotor applications.

Appendix A (Placeholder) paper draft

A placeholder is included in this appendix for the draft manuscript concerning the up-wash mechanism identified in the preliminary rotor-simulation results (Section 4.2). This mechanism emerged as an unexpected and potentially significant flow feature during the early stages of the study, prompting a separate, more detailed investigation. The forthcoming paper will document the characterization of this up-wash behavior, its physical origin, and its implications for tandem-rotor wake dynamics. The current placeholder indicates where the full draft will be inserted once the analysis and manuscript preparation are completed.

Appendix B Probe statistics

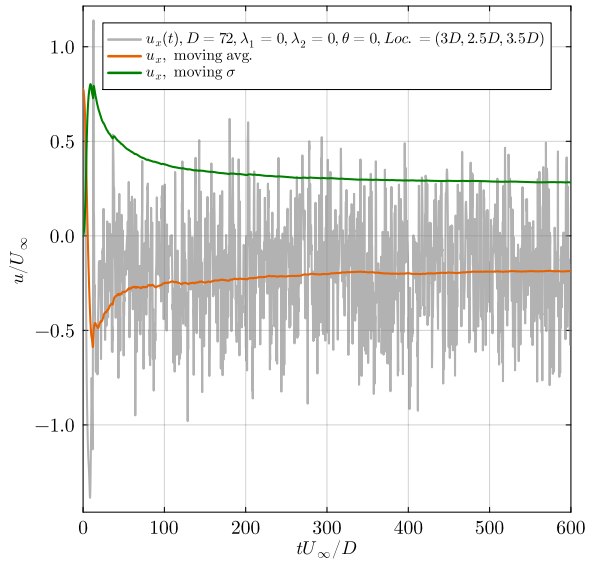

Figure 107: Streamwise velocity component recorded by the probe and its moving average and standard deviation (σ) for TC1.

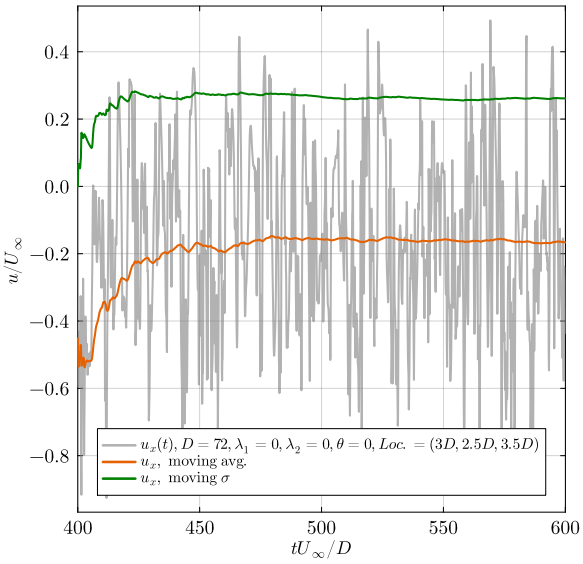

Figure 108: Streamwise velocity component recorded by the probe and its moving average and standard deviation (σ) in the time-averaging window for TC1.

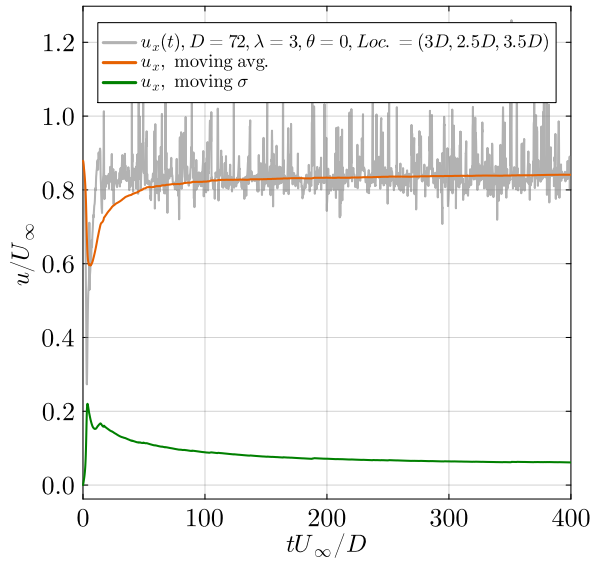

Figure 109: Streamwise velocity component recorded by the probe and its moving average and standard deviation (σ) for TC2.

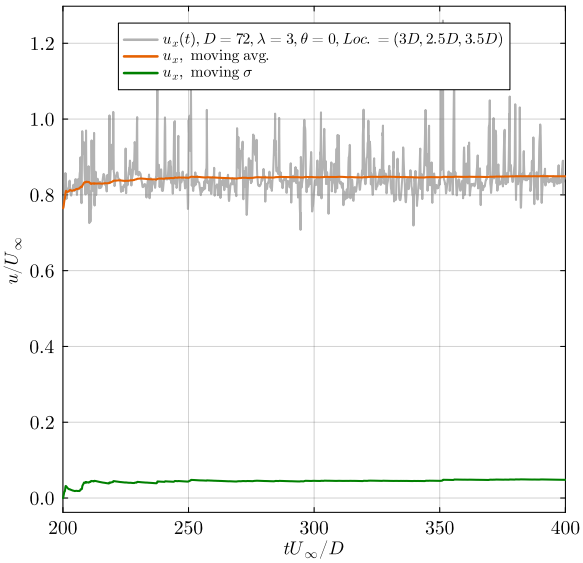

Figure 110: Streamwise velocity component recorded by the probe and its moving average and standard deviation (σ) in the time-averaging window for TC2.

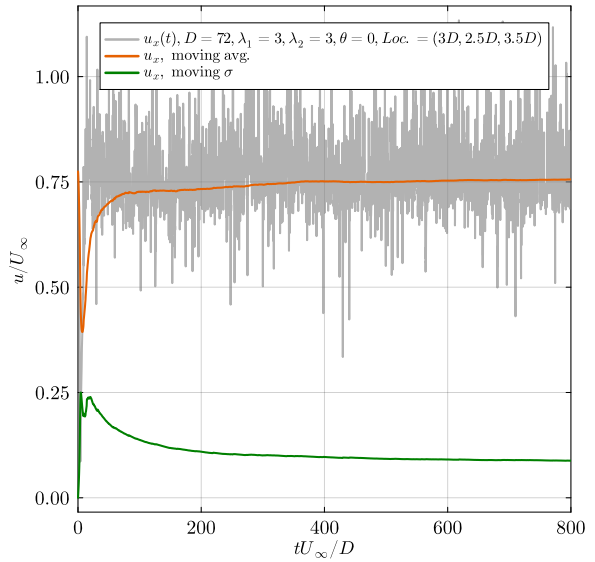

Figure 111: Streamwise velocity component recorded by the probe and its moving average and standard deviation (σ) for $\lambda_1 = 3$, $\lambda_2 = 3$, $\theta = 0°$.

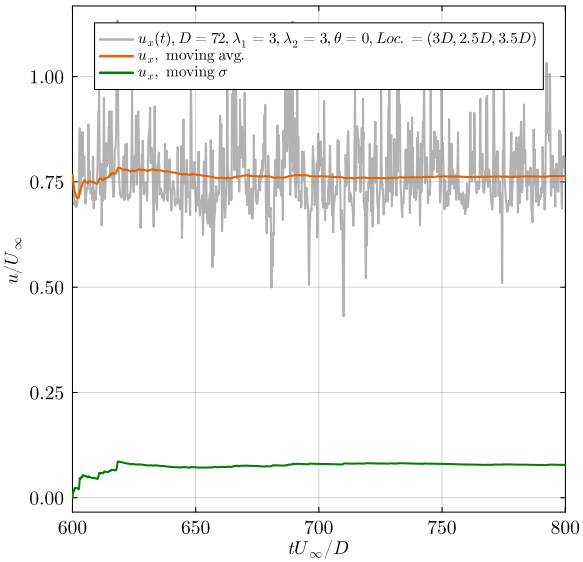

Figure 112: Streamwise velocity component recorded by the probe and its moving average and standard deviation (σ) in the time-averaging window for $\lambda_1 = 3$, $\lambda_2 = 3$, $\theta = 0°$.

Appendix C Sensitivity analysis for MLP

Note that the MLP structure is indicated with the number of hidden layers (HL), hidden layer width and the activation function name. For instance a MLP structure with two hidden

layers including the input layer, layer width of 16 and ReLU activation function is indicated as 2HL16ReLU.

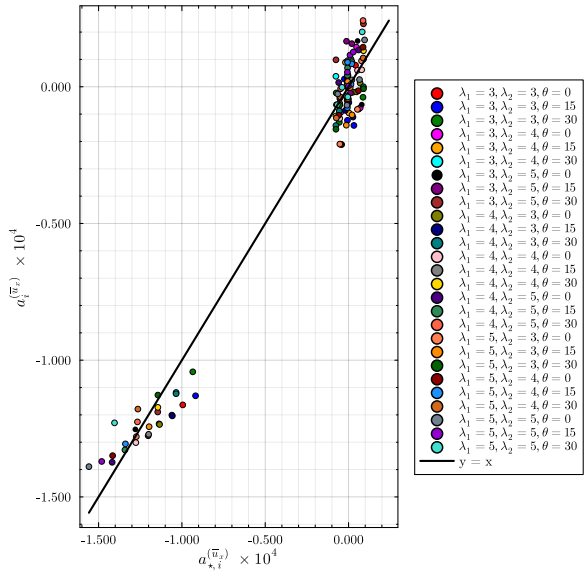

Figure 113: 2HL32ReLU: Parity $q = \overline{u}_x$.

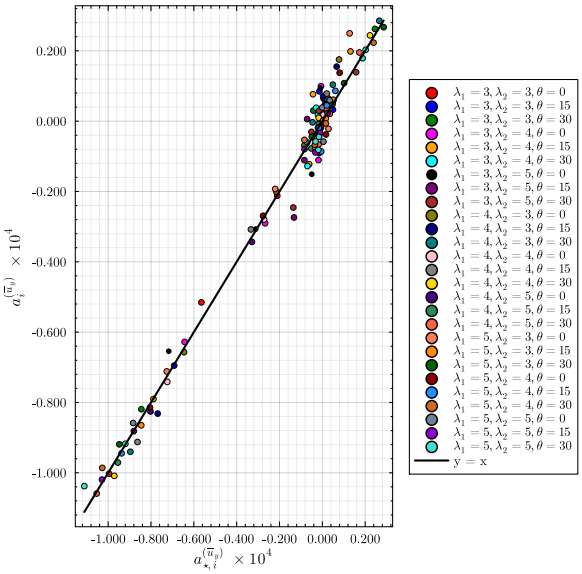

Figure 114: 2HL32ReLU: Parity $q = \overline{u}_y$.

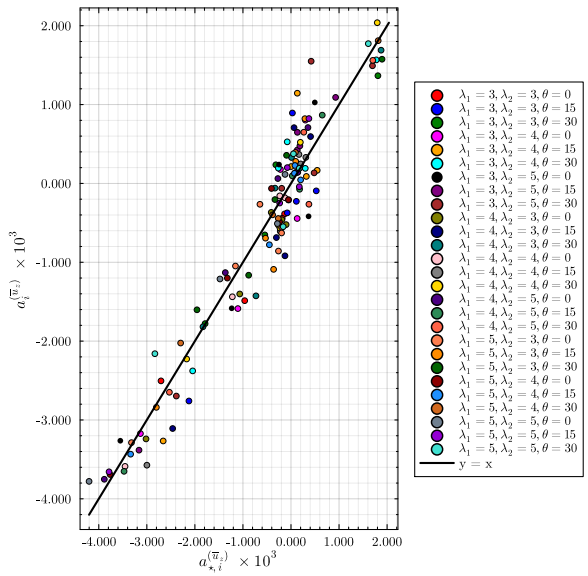

Figure 115: 2HL32ReLU: Parity $q = \overline{u}_z$.

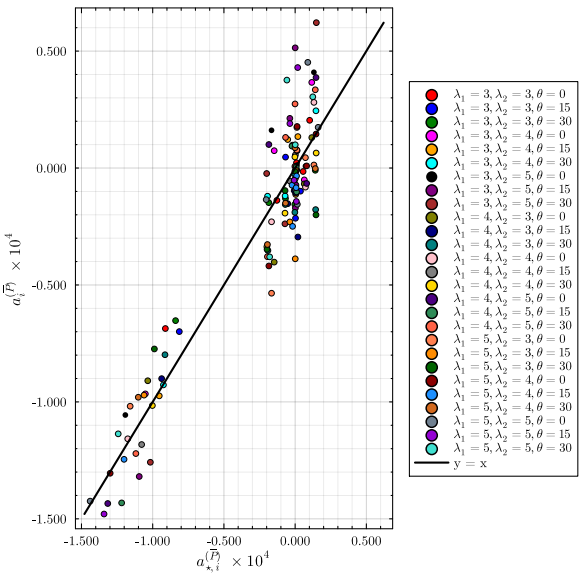

Figure 116: 2HL32ReLU: Parity $q = \overline{P}$.

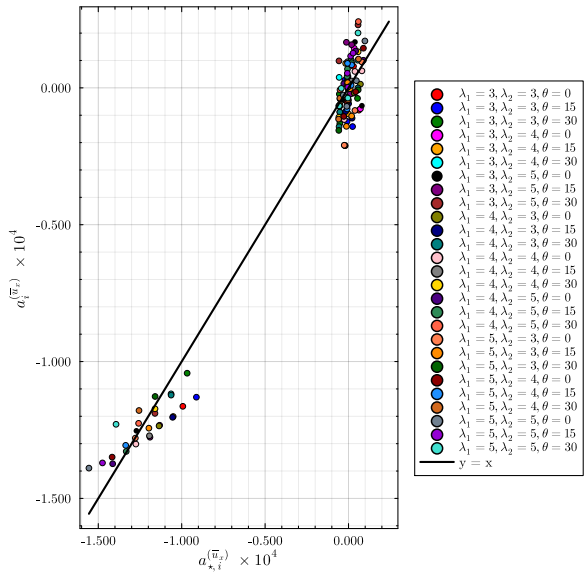

Figure 117: 2HL64ReLU: Parity $q = \overline{u}_x$.

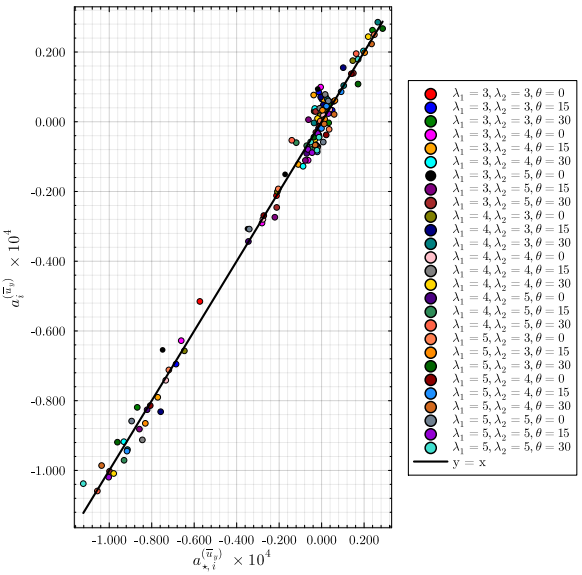

Figure 118: 2HL64ReLU: Parity $q = \overline{u}_y$.

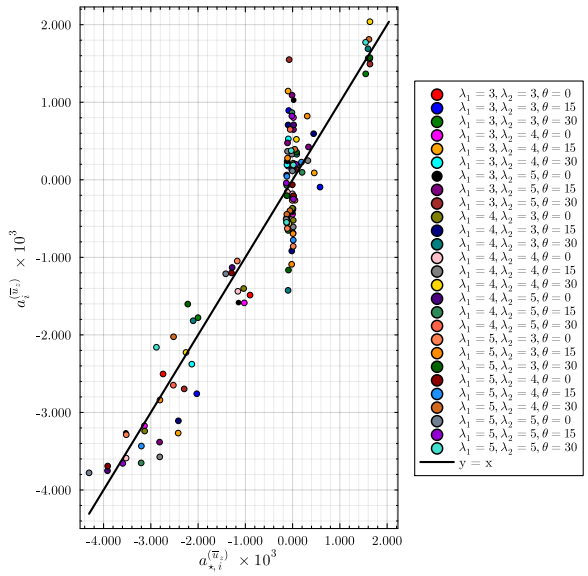

Figure 119: 2HL64ReLU: Parity $q = \overline{u}_z$.

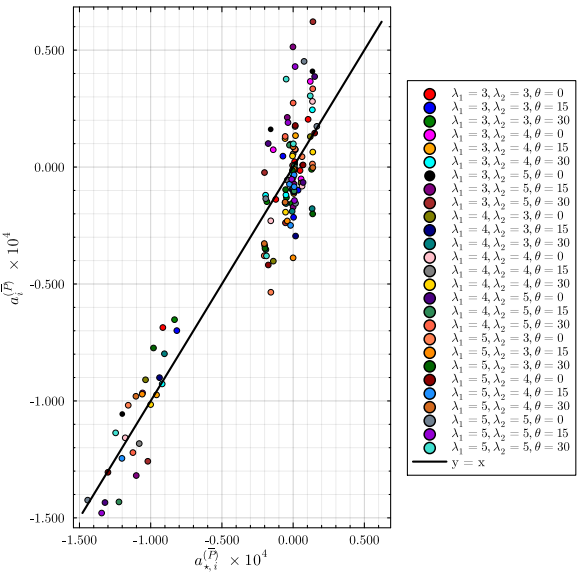

Figure 120: 2HL64ReLU: Parity $q = \overline{P}$.

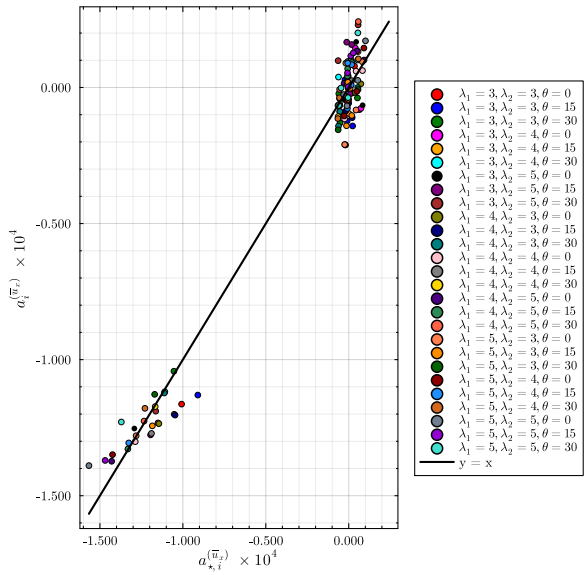

Figure 121: 3HL32ReLU: Parity $q = \overline{u}_x$.

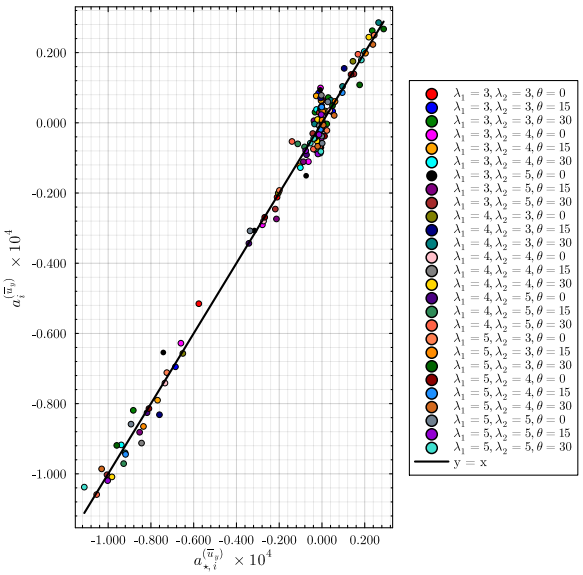

Figure 122: 3HL32ReLU: Parity $q = \overline{u}_y$.

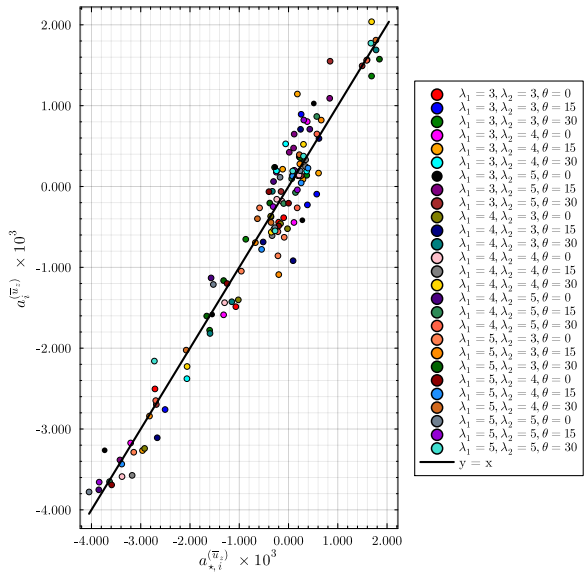

Figure 123: 3HL32ReLU: Parity $q = \overline{u}_z$.

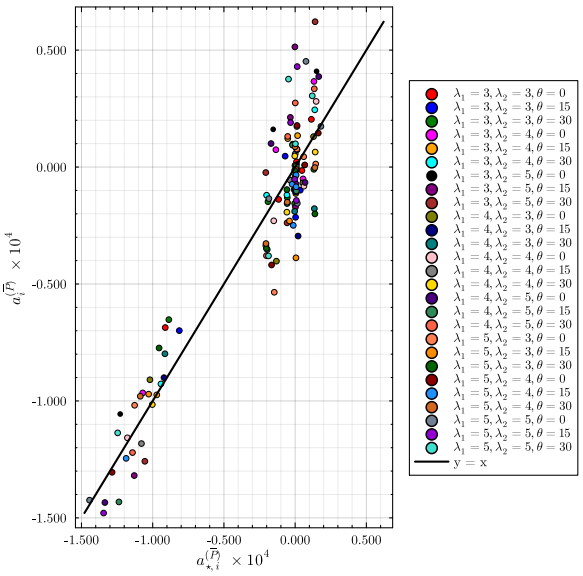

Figure 124: 3HL32ReLU: Parity $q = \overline{P}$.

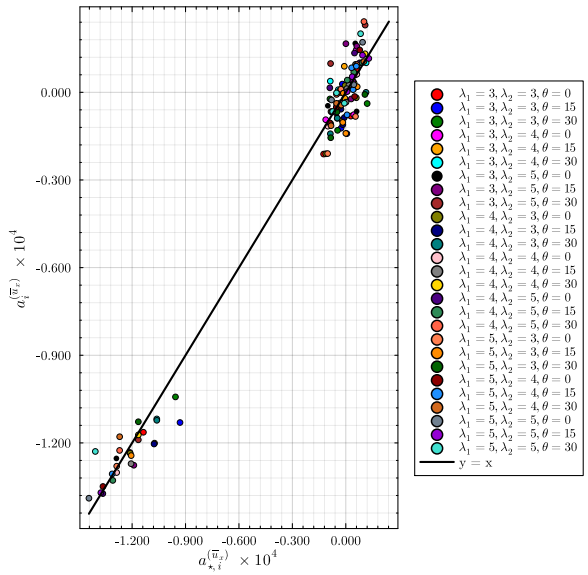

Figure 125: 2HL32Swish: Parity $q = \overline{u}_x$.

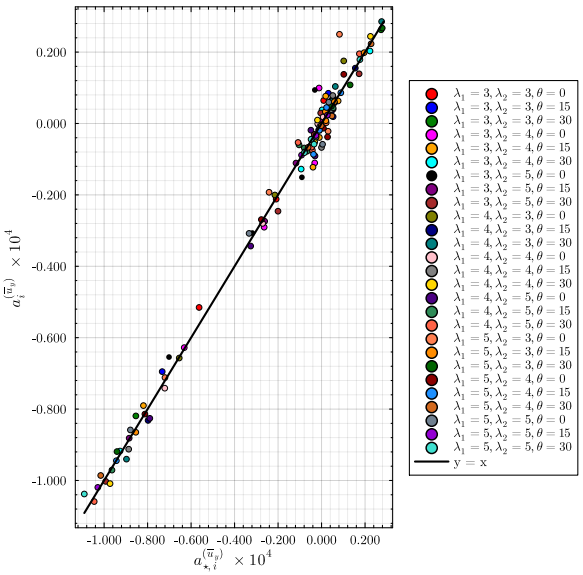

Figure 126: 2HL32Swish: Parity $q = \overline{u}_y$.

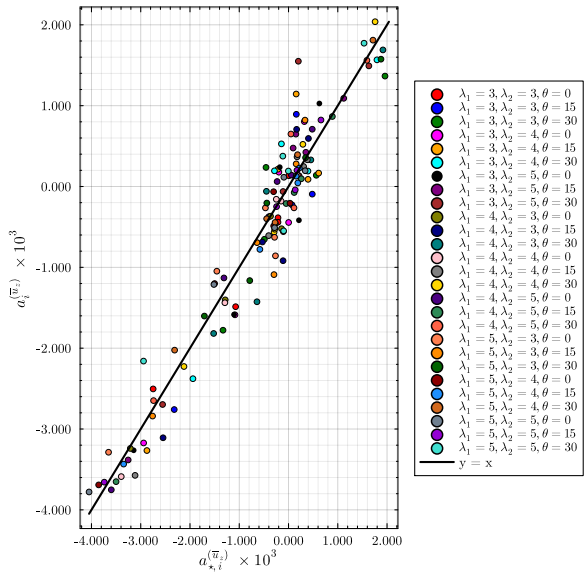

Figure 127: 2HL32Swish: Parity $q = \overline{u}_z$.

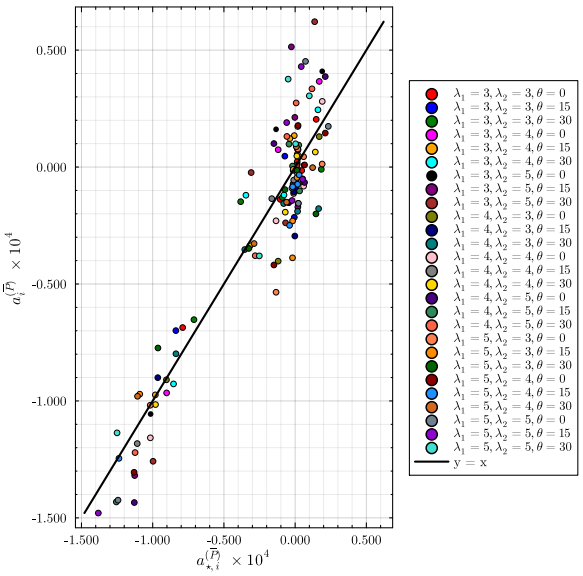

Figure 128: 2HL32Swish: Parity $q = \overline{P}$.

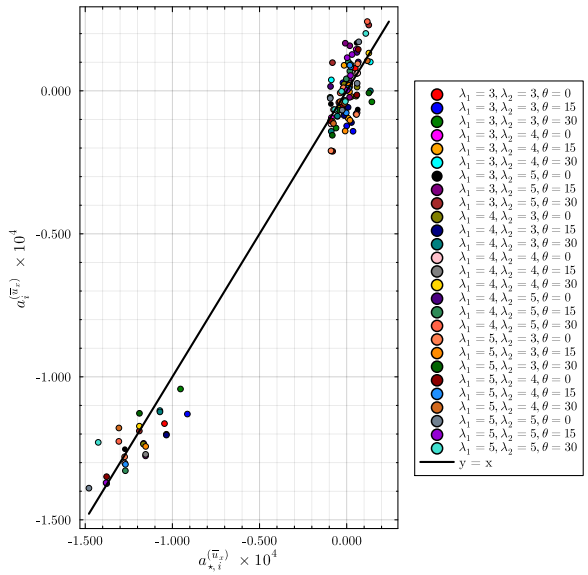

Figure 129: 2HL64Swish: Parity $q = \overline{u}_x$.

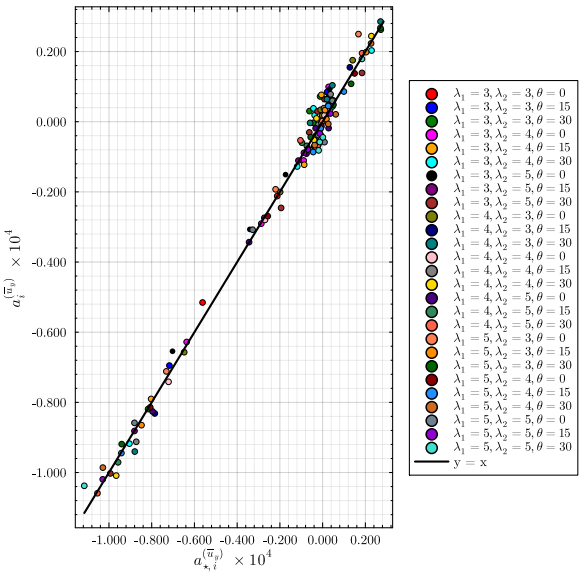

Figure 130: 2HL64Swish: Parity $q = \overline{u}_y$.

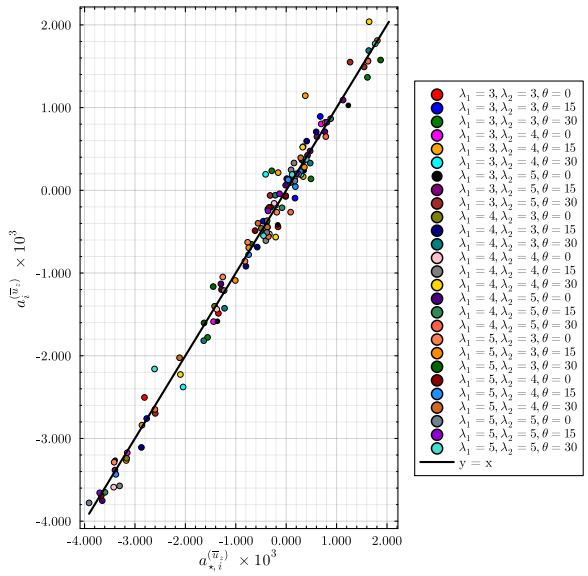

Figure 131: 2HL64Swish: Parity $q = \overline{u}_z$.

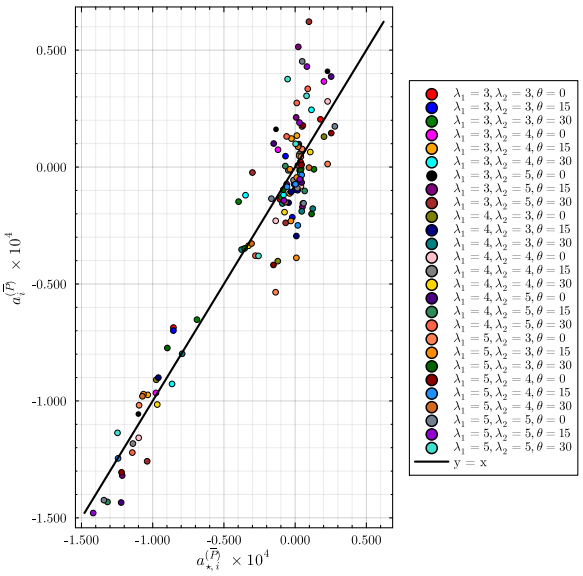

Figure 132: 2HL64Swish: Parity $q = \overline{P}$.

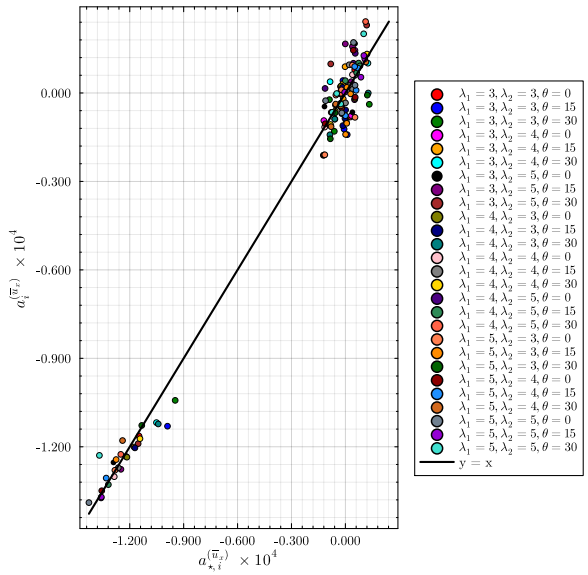

Figure 133: 3HL32Swish: Parity $q = \overline{u}_x$.

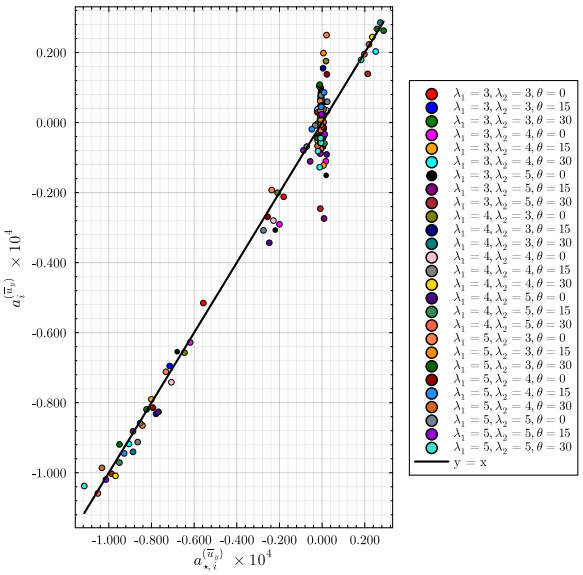

Figure 134: 3HL32Swish: Parity $q = \overline{u}_y$.

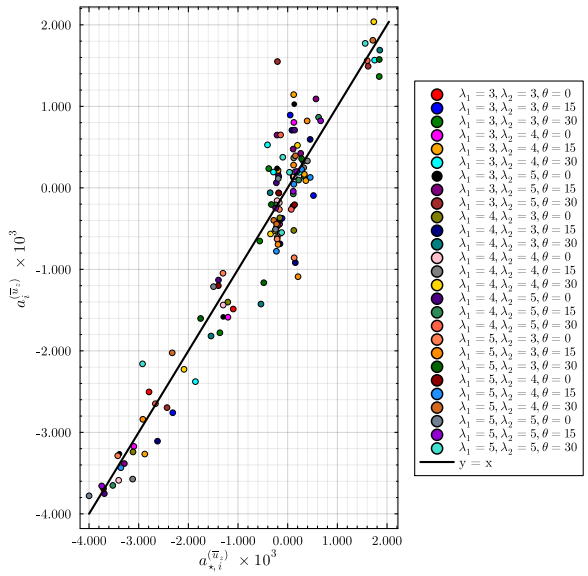

Figure 135: 3HL32Swish: Parity $q = \overline{u}_z$.

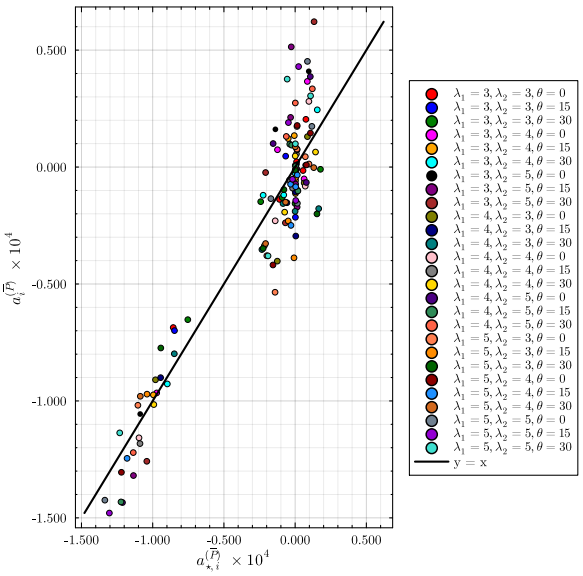

Figure 136: 3HL32Swish: Parity $q = \overline{P}$.

Appendix D Predicted POD coefficient space

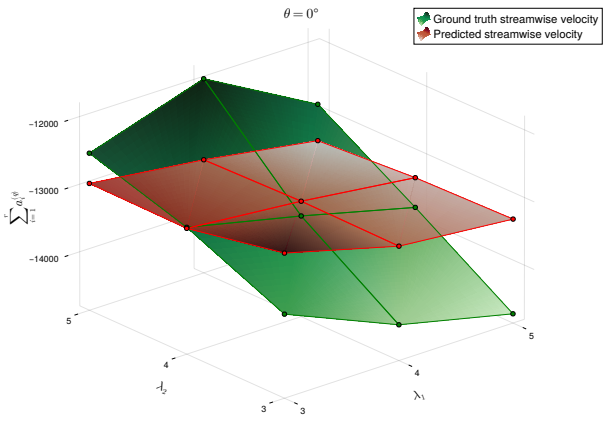

Figure 137: Predicted and ground truth truncated POD coefficient surface for $q = \overline{u}_x$ for $\theta = 0°$.

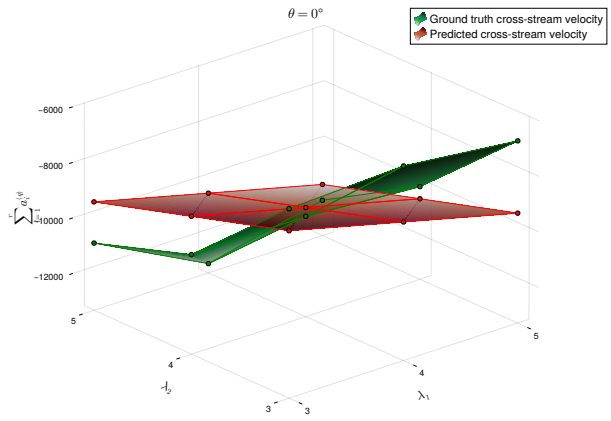

Figure 138: Predicted and ground truth truncated POD coefficient surface for $q = \overline{u}_y$ for $\theta = 0°$.

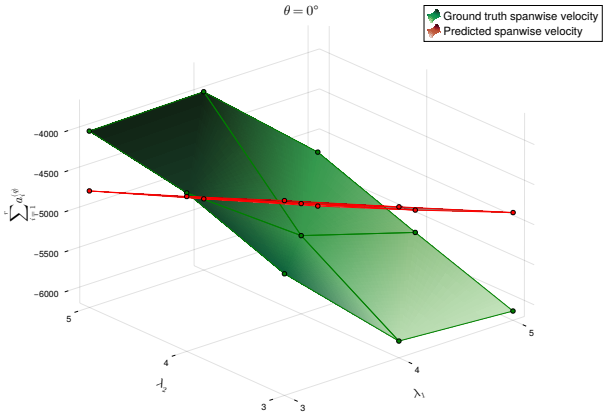

Figure 139: Predicted and ground truth truncated POD coefficient surface for $q = \overline{u}_z$ for $\theta = 0°$.

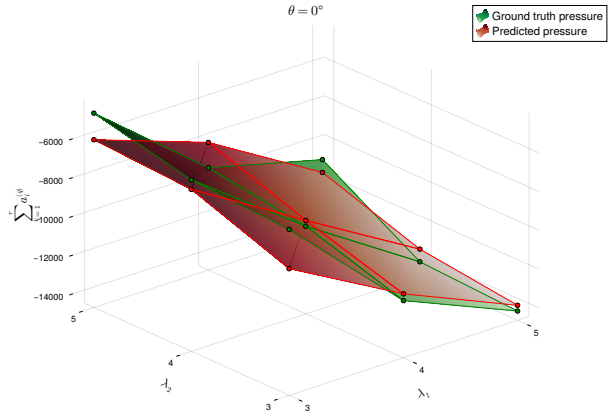

Figure 140: Predicted and ground truth truncated POD coefficient surface for $q = \overline{P}$ for $\theta = 0°$.

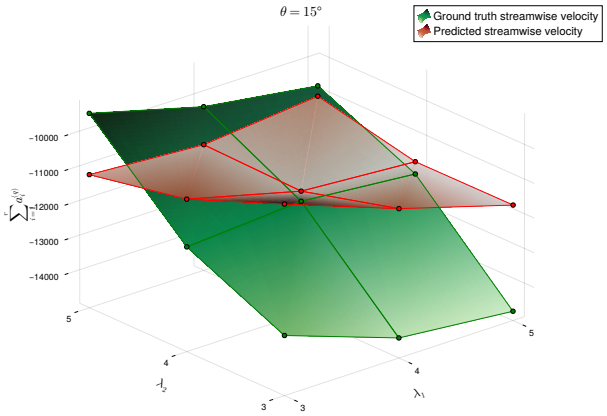

Figure 141: Predicted and ground truth truncated POD coefficient surface for $q = \overline{u}_x$ for $\theta = 15°$.

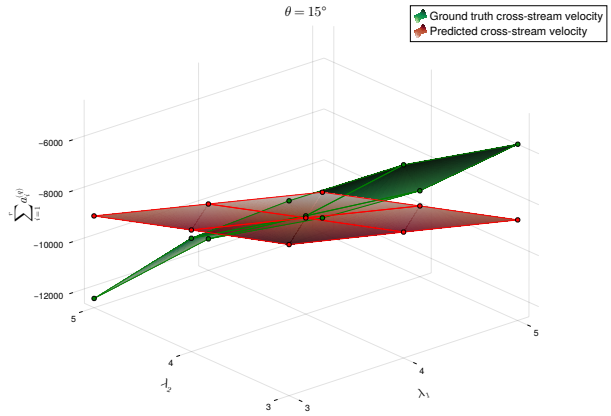

Figure 142: Predicted and ground truth truncated POD coefficient surface for $q = \overline{u}_y$ for $\theta = 15°$.

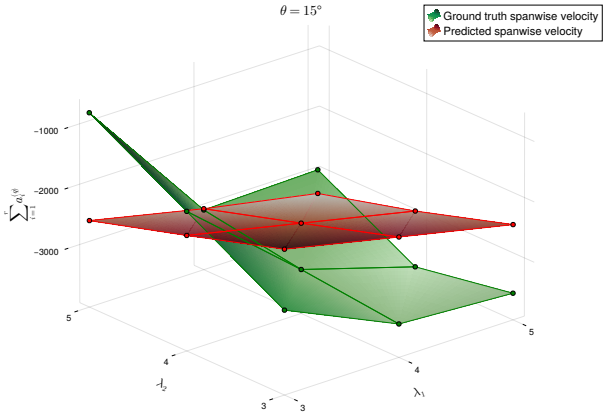

Figure 143: Predicted and ground truth truncated POD coefficient surface for $q = \overline{u}_z$ for $\theta = 15°$.

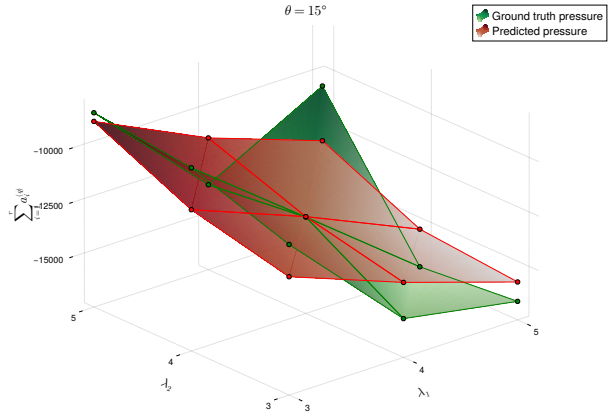

Figure 144: Predicted and ground truth truncated POD coefficient surface for $q = \overline{P}$ for $\theta = 15°$.

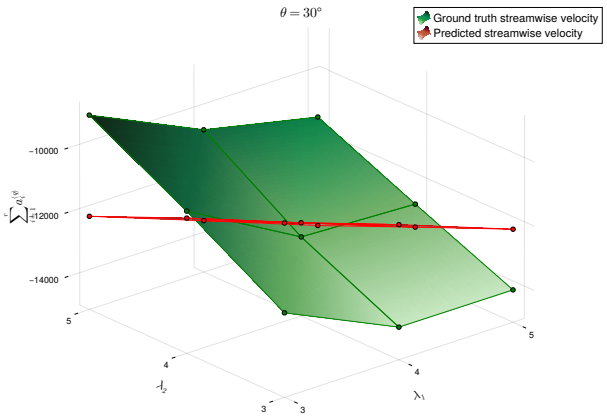

Figure 145: Predicted and ground truth truncated POD coefficient surface for $q = \overline{u}_x$ for $\theta = 30°$.

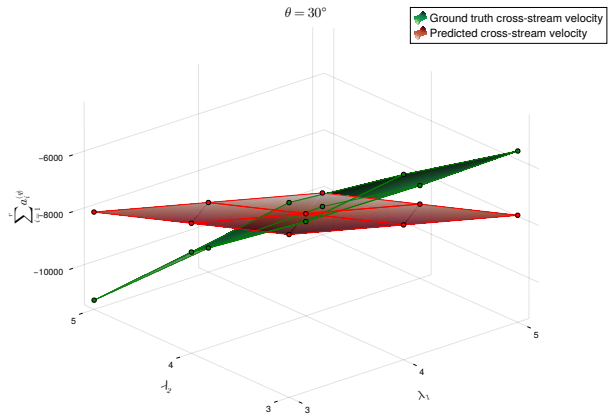

Figure 146: Predicted and ground truth truncated POD coefficient surface for $q = \overline{u}_y$ for $\theta = 30°$.

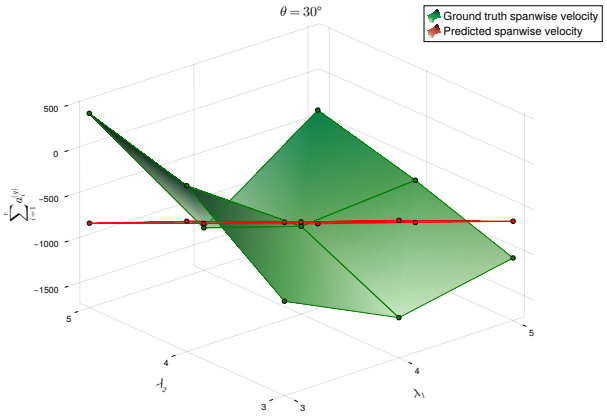

Figure 147: Predicted and ground truth truncated POD coefficient surface for $q = \overline{u}_z$ for $\theta = 30°$.

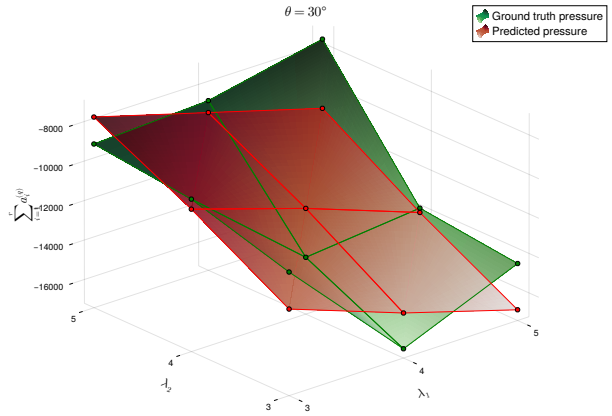

Figure 148: Predicted and ground truth truncated POD coefficient surface for $q = \overline{P}$ for $\theta = 30°$.

Appendix E Field errors for both algorithms

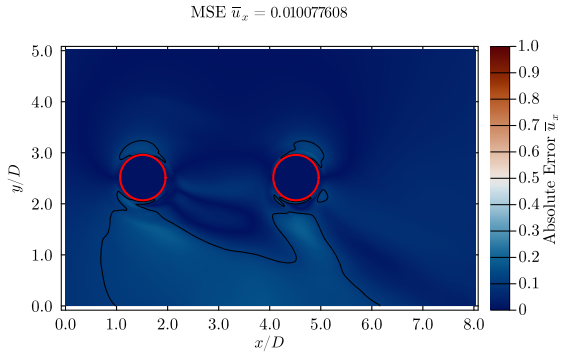

Figure 149: Squared error contours for time-averaged streamwise velocity for $\lambda_1 = 3$, $\lambda_2 = 3$, $\theta = 0°$ at $z = 3.0D$ by MLP.

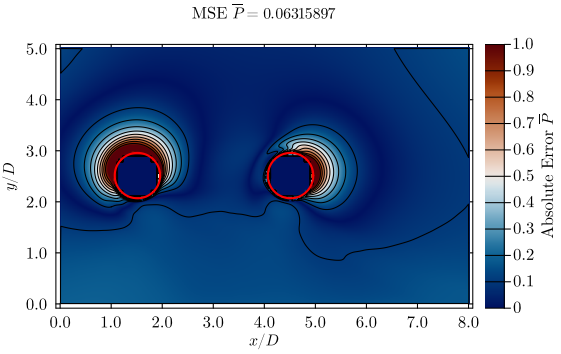

Figure 150: Squared error contours for time-averaged pressure for $\lambda_1 = 3$, $\lambda_2 = 3$, $\theta = 0°$ at $z = 3.0D$ by MLP.

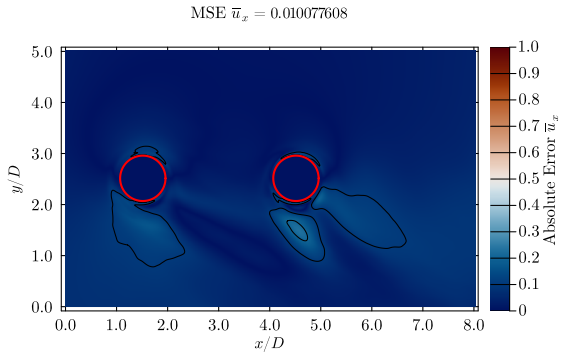

Figure 151: Squared error contours for time-averaged streamwise velocity for $\lambda_1 = 3$, $\lambda_2 = 3$, $\theta = 0°$ at $z = 5.0D$ by MLP.

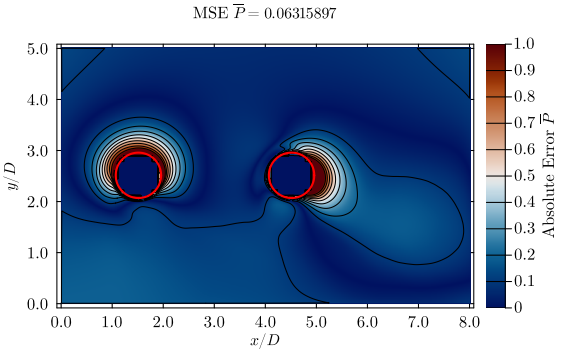

Figure 152: Squared error contours for time-averaged pressure for $\lambda_1 = 3$, $\lambda_2 = 3$, $\theta = 0°$ at $z = 5.0D$ by MLP.

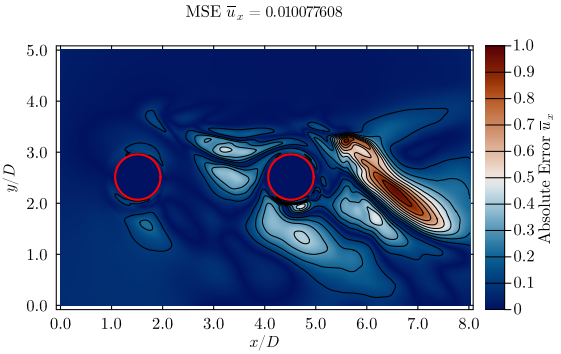

Figure 153: Squared error contours for time-averaged streamwise velocity for $\lambda_1 = 3$, $\lambda_2 = 3$, $\theta = 0°$ at $z = 6.5D$ by MLP.

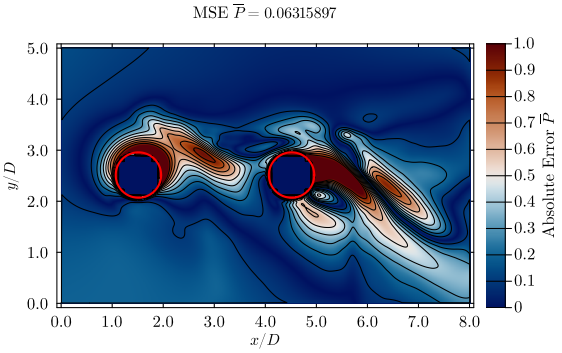

Figure 154: Squared error contours for time-averaged pressure for $\lambda_1 = 3$, $\lambda_2 = 3$, $\theta = 0°$ at $z = 6.5D$ by MLP.

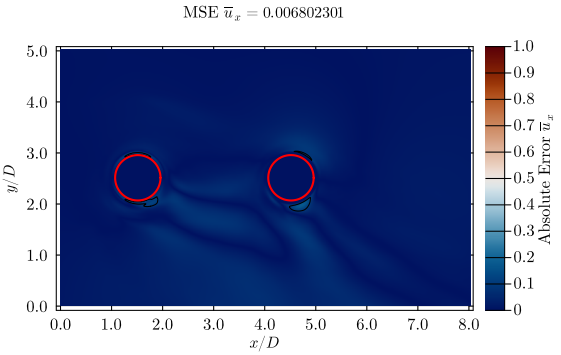

Figure 155: Squared error contours for time-averaged streamwise velocity for $\lambda_1 = 3$, $\lambda_2 = 3$, $\theta = 0°$ at $z = 3.0D$ by BR.

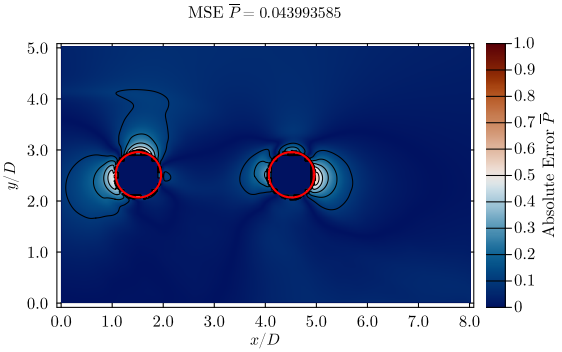

Figure 156: Squared error contours for time-averaged pressure for $\lambda_1 = 3$, $\lambda_2 = 3$, $\theta = 0°$ at $z = 3.0D$ by BR.

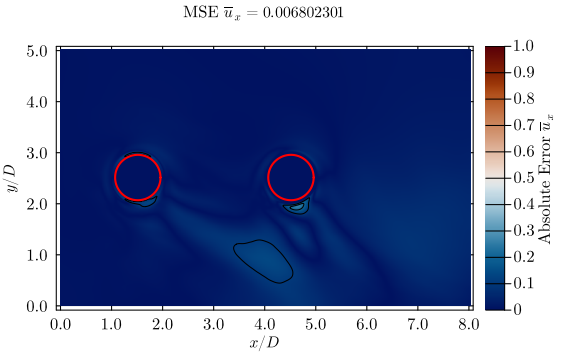

Figure 157: Squared error contours for time-averaged streamwise velocity for $\lambda_1 = 3$, $\lambda_2 = 3$, $\theta = 0°$ at $z = 5.0D$ by BR.

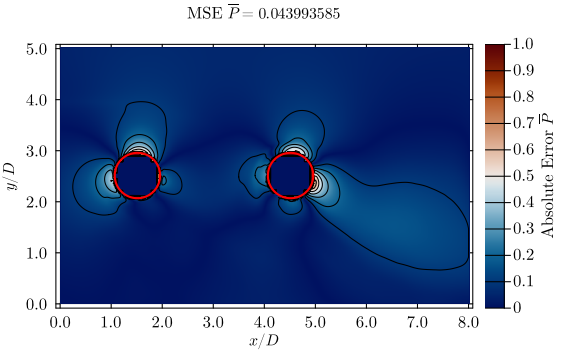

Figure 158: Squared error contours for time-averaged pressure for $\lambda_1 = 3$, $\lambda_2 = 3$, $\theta = 0°$ at $z = 5.0D$ by BR.

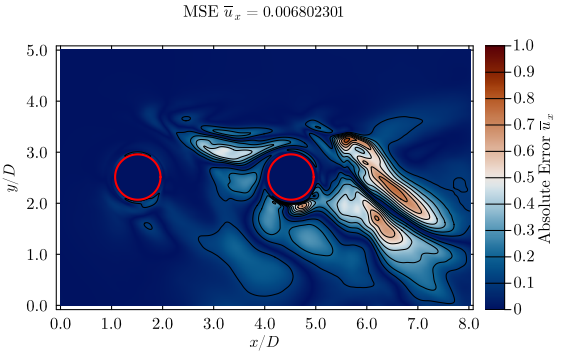

Figure 159: Squared error contours for time-averaged streamwise velocity for $\lambda_1 = 3$, $\lambda_2 = 3$, $\theta = 0°$ at $z = 6.5D$ by BR.

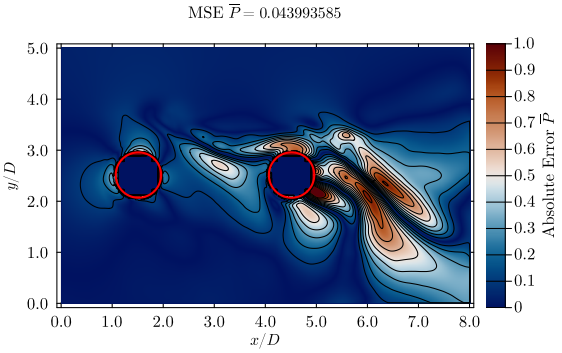

Figure 160: Squared error contours for time-averaged pressure for $\lambda_1 = 3$, $\lambda_2 = 3$, $\theta = 0°$ at $z = 6.5D$ by BR.

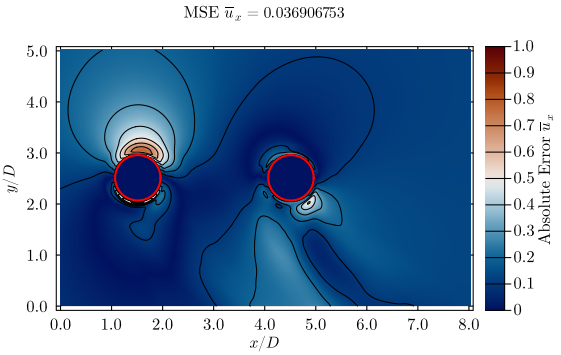

Figure 161: Squared error contours for time-averaged streamwise velocity for $\lambda_1 = 4$, $\lambda_2 = 3$, $\theta = 15°$ at $z = 3.0D$ by MLP.

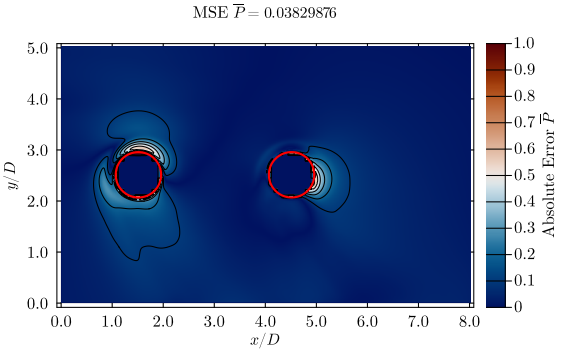

Figure 162: Squared error contours for time-averaged pressure for $\lambda_1 = 4$, $\lambda_2 = 3$, $\theta = 15°$ at $z = 3.0D$ by MLP.

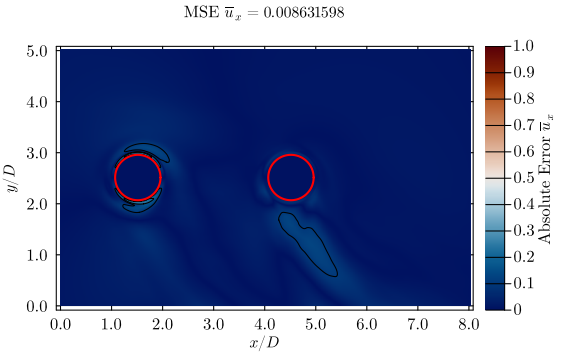

Figure 163: Squared error contours for time-averaged streamwise velocity for $\lambda_1 = 4$, $\lambda_2 = 3$, $\theta = 15°$ at $z = 3.0D$ by BR.

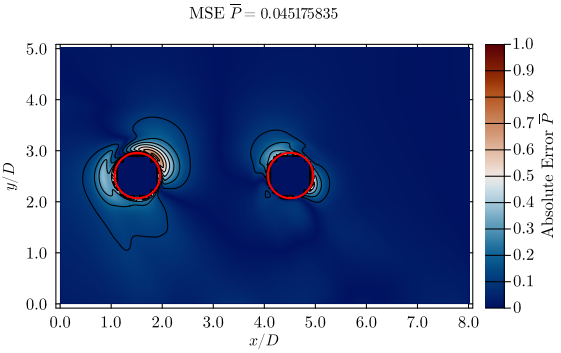

Figure 164: Squared error contours for time-averaged pressure for $\lambda_1 = 4$, $\lambda_2 = 3$, $\theta = 15°$ at $z = 3.0D$ by BR.

Appendix F Force prediction

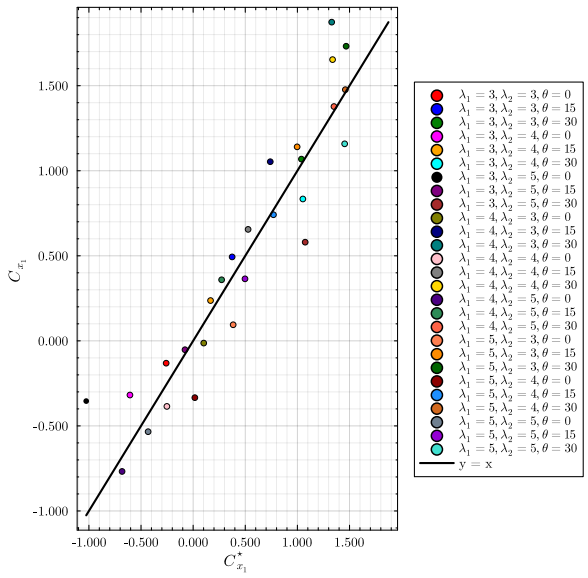

Figure 165: Parity plot of predicted and ground truth $\overline{C}_{x_1}$ by BR.

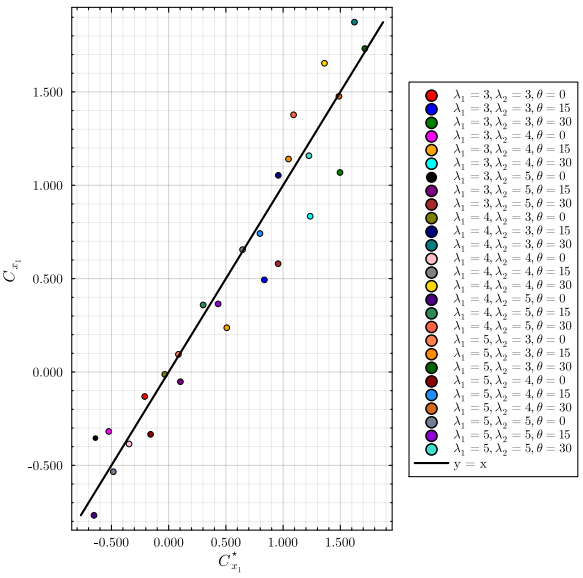

Figure 166: Parity plot of predicted and ground truth $\overline{C}_{x_1}$ by MLP.

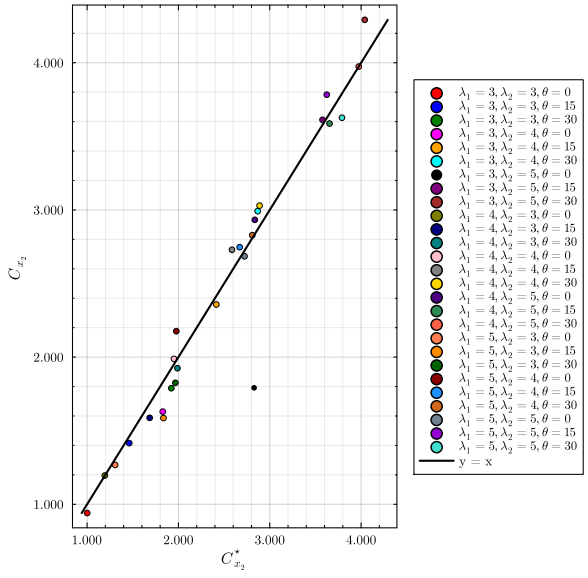

Figure 167: Parity plot of predicted and ground truth $\overline{C}_{x_2}$ by BR.

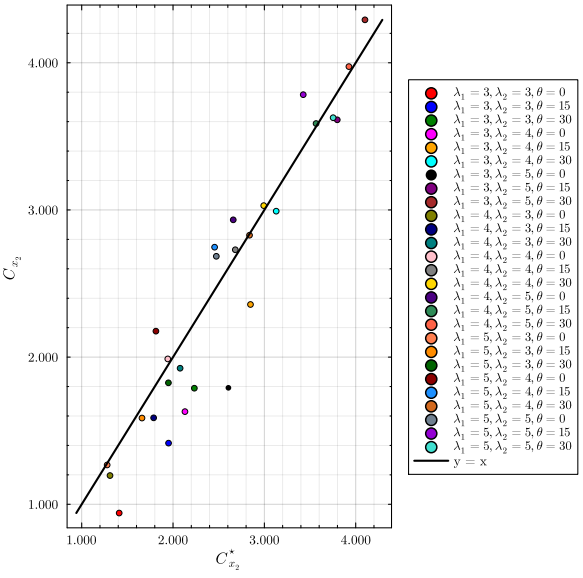

Figure 168: Parity plot of predicted and ground truth $\overline{C}_{x_2}$ by MLP.

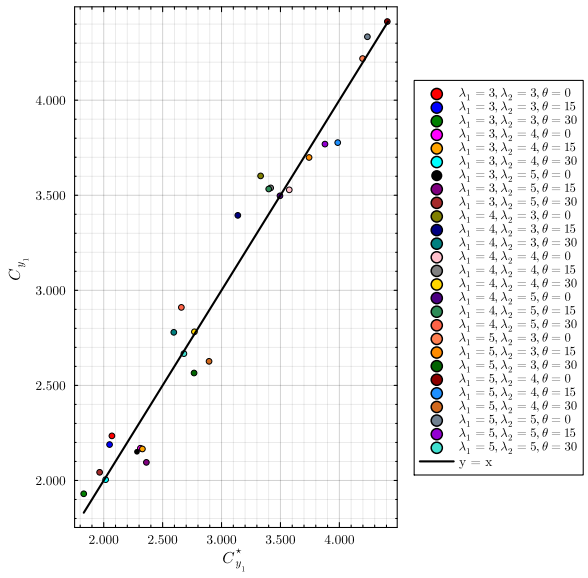

Figure 169: Parity plot of predicted and ground truth $\overline{C}_{y_1}$ by BR.

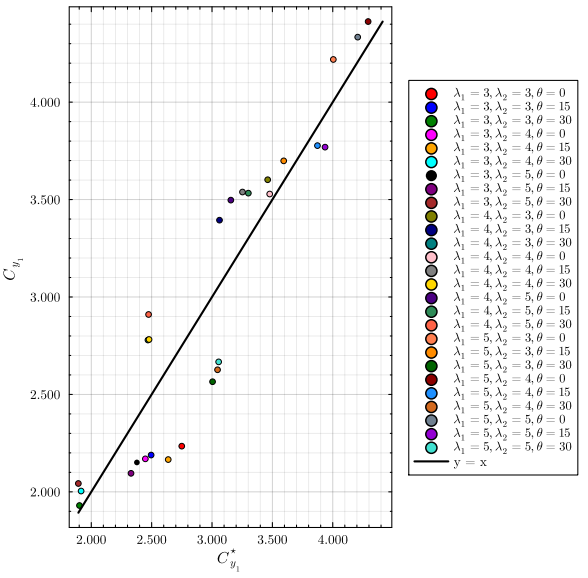

Figure 170: Parity plot of predicted and ground truth $\overline{C}_{y_1}$ by MLP.

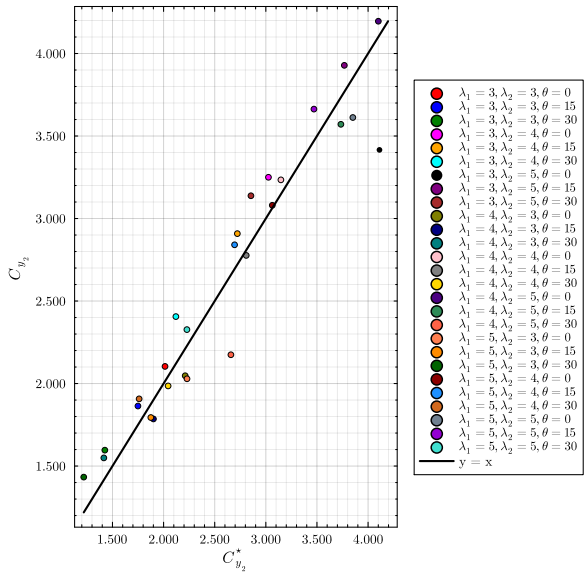

Figure 171: Parity plot of predicted and ground truth $\overline{C}_{y_2}$ by BR.

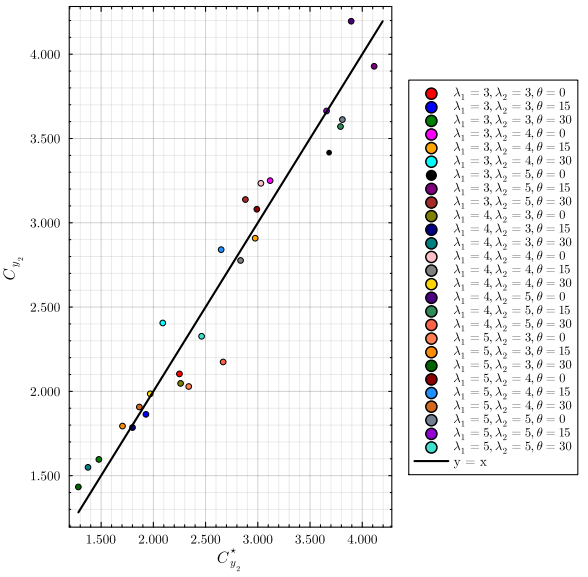

Figure 172: Parity plot of predicted and ground truth $\overline{C}_{y_2}$ by MLP.

References

Abadía-Heredia, R., López-Martín, M., Carro, B., Arribas, J. I., Pérez, J. M., and Le Clainche, S. (2022). A predictive hybrid reduced order model based on proper orthogonal decomposition combined with deep learning architectures. *Expert Systems with Applications*, 187:115910.

Adaramola, M., Akinlade, O., Sumner, D., Bergstrom, D., and Schenstead, A. (2006). Turbulent wake of a finite circular cylinder of small aspect ratio. *Journal of Fluids and Structures*, 22(6-7):919–928.

Afgan, I., Kahil, Y., Benhamadouche, S., and Sagaut, P. (2011). Large eddy simulation of the flow around single and two side-by-side cylinders at subcritical reynolds numbers. *Physics of Fluids*, 23(7).

Afgan, I., Moulinec, C., Prosser, R., and Laurence, D. (2007). Large eddy simulation of turbulent flow for wall mounted cantilever cylinders of aspect ratio 6 and 10. *International Journal of Heat and Fluid Flow*, 28(4):561–574.

Ahmadi-Baloutaki, M., Carriveau, R., and Ting, D. S. (2016). A wind tunnel study on the aerodynamic interaction of vertical axis wind turbines in array configurations. *Renewable energy*, 96:904–913.

Aksoy, M. H., Yagmur, S., Dogan, S., Goktepeli, I., and Ispir, M. (2024). Experimental study on cylinder wake control using forced rotation. *Journal of Wind Engineering and Industrial Aerodynamics*, 246:105662.

Alam, M. M. (2014). The aerodynamics of a cylinder submerged in the wake of another. *Journal of Fluids and Structures*, 51:393–400.

Alam, M. M. and Meyer, J. P. (2011). Two interacting cylinders in cross flow. *Physical Review E—Statistical, Nonlinear, and Soft Matter Physics*, 84(5):056304.

Alam, M. M., Moriya, M., and Sakamoto, H. (2003a). Aerodynamic characteristics of two side-by-side circular cylinders and application of wavelet analysis on the switching phenomenon. *Journal of Fluids and Structures*, 18(3-4):325–346.

Alam, M. M., Moriya, M., Takai, K., and Sakamoto, H. (2003b). Fluctuating fluid forces acting on two circular cylinders in a tandem arrangement at a subcritical reynolds number. *Journal of Wind Engineering and Industrial Aerodynamics*, 91(1-2):139–154.

Aljure, D., Lehmkhul, O., Rodríguez, I., and Oliva, A. (2017). Three dimensionality in the wake of the flow around a circular cylinder at reynolds number 5000. *Computers & Fluids*, 147:102–118.

Aljure, D., Rodríguez, I., Lehmkuhl, O., Pérez-Segarra, C. D., and Oliva, A. (2015). Influence of rotation on the flow over a cylinder at re= 5000. *International Journal of Heat and Fluid Flow*, 55:76–90.

Alkhaledi, A. N., Sampath, S., and Pilidis, P. (2023). Techno environmental assessment of flettner rotor as assistance propulsion system for lh2 tanker ship fuelled by hydrogen. *Sustainable Energy Technologies and Assessments*, 55:102935.

Alonso, D., Vega, J. M., Velázquez, Á., and de Pablo, V. (2012). Reduced-order modeling of three-dimensional external aerodynamic flows. *Journal of Aerospace Engineering*, 25(4):588–599.

Anemoi (2025). Anemoi rotor sails: Setting the world in motion with wind. `https://anemoimarine.com/rotor-sail-technology/#technical-equipment`, London, Lloyds Avenue.

Anemoi (n.d.). Anemoi. `https://anemoimarine.com/`, Accessed: 2024-12-20.

Atlar, M., Gören, Ö., et al. (2010). Effect of turbulence modelling on the computation of the near-wake flow of a circular cylinder. *Ocean engineering*, 37(4):387–399.

Azadani, L. (2023). Vertical axis wind turbines in cluster configurations. *Ocean Engineering*, 272:113855.

Badalamenti, C. and Prince, S. (2008). Effects of endplates on a rotating cylinder in crossflow. In *26th AIAA Applied Aerodynamics Conference*, page 7063.

Bai, H., Alam, M. M., Gao, N., and Lin, Y. (2019). The near wake of sinusoidal wavy cylinders: Three-dimensional pod analyses. *International Journal of Heat and Fluid Flow*, 75:256–277.

Behara, S., Chandra, V., and Prashanth, N. (2022). Three-dimensional transition in the wake of two tandem rotating cylinders. *Journal of Fluid Mechanics*, 951:A29.

Bordogna, G., Muggiasca, S., Giappino, S., Belloli, M., Keuning, J., and Huijsmans, R. (2020). The effects of the aerodynamic interaction on the performance of two flettner rotors. *Journal of Wind Engineering and Industrial Aerodynamics*, 196:104024.

Bordogna, G., Muggiasca, S., Giappino, S., Belloli, M., Keuning, J., Huijsmans, R., and Van't Veer, A. (2019). Experiments on a flettner rotor at critical and supercritical reynolds numbers. *Journal of Wind Engineering and Industrial Aerodynamics*, 188:19–29.

Braconnier, T., Ferrier, M., Jouhaud, J.-C., Montagnac, M., and Sagaut, P. (2011). Towards an adaptive pod/svd surrogate model for aeronautic design. *Computers & Fluids*, 40(1):195–209.

Breuer, M. (1998). Numerical and modeling influences on large eddy simulations for the flow past a circular cylinder. *International Journal of Heat and Fluid Flow*, 19(5):512–521.

Breuer, M. (2000). A challenging test case for large eddy simulation: high reynolds number circular cylinder flow. *International journal of heat and fluid flow*, 21(5):648–654.

Cantwell, B. and Coles, D. (1983). An experimental study of entrainment and transport in the turbulent near wake of a circular cylinder. *Journal of fluid mechanics*, 136:321–374.

Catalano, P., Wang, M., Iaccarino, G., and Moin, P. (2003). Numerical simulation of the flow around a circular cylinder at high reynolds numbers. *International journal of heat and fluid flow*, 24(4):463–469.

Cengel, Y. and Cimbala, J. (2013). *Ebook: Fluid mechanics fundamentals and applications (si units)*. McGraw Hill.

Chang, C., Zhang, W., and Huang, Z. (2024). Numerical analysis of flow interference passing through tandem cylinders at re= 3900. *Ocean Engineering*, 313:119546.

Chen, W., Wang, H., and Liu, X. (2023). Experimental investigation of the aerodynamic performance of flettner rotors for marine applications. *Ocean Engineering*, 281:115006.

Cheng, W., Pullin, D., and Samtaney, R. (2018). Large-eddy simulation of flow over a rotating cylinder: The lift crisis at. *Journal of Fluid Mechanics*, 855:371–407.

Craig, A. E., Dabiri, J. O., and Koseff, J. R. (2016). A kinematic description of the key flow characteristics in an array of finite-height rotating cylinders. *Journal of Fluids Engineering*, 138(7):070906.

Dargahi, B. (1989). The turbulent flow field around a circular cylinder. *Experiments in fluids*, 8:1–12.

Darvishyadegari, M. and Hassanzadeh, R. (2019). Heat and fluid flow around two co-rotating cylinders in tandem arrangement. *International Journal of Thermal Sciences*, 135:206–220.

Deep, D., Sahasranaman, A., and Senthilkumar, S. (2022). Pod analysis of the wake behind a circular cylinder with splitter plate. *European Journal of Mechanics-B/Fluids*, 93:1–12.

Delft High Performance Computing Centre (DHPC) (2024). DelftBlue Supercomputer (Phase 2). `https://www.tudelft.nl/dhpc/ark:/44463/DelftBluePhase2`.

Diaz, F., Gavaldà, J., Kawall, J., Keffer, J., and Giralt, F. (1983). Vortex shedding from a spinning cylinder. *The Physics of fluids*, 26(12):3454–3460.

Dol, S. S., Kopp, G. A., and Martinuzzi, R. J. (2008). The suppression of periodic vortex shedding from a rotating circular cylinder. *Journal of Wind Engineering and Industrial Aerodynamics*, 96(6-7):1164–1184.

Dong, S., Karniadakis, G., Ekmekci, A., and Rockwell, D. (2006). A combined direct numerical simulation–particle image velocimetry study of the turbulent near wake. *Journal of Fluid Mechanics*, 569:185–207.

Dong, S. and Karniadakis, G. E. (2005). Dns of flow past a stationary and oscillating cylinder at re= 10000. *Journal of fluids and structures*, 20(4):519–531.

Eco-Flettner (n.d.). Eco flettner rotor. `https://ecoflettner.de/`, Accessed: 2024-12-20.

Eivazi, H., Veisi, H., Naderi, M. H., and Esfahanian, V. (2020). Deep neural networks for nonlinear model order reduction of unsteady flows. *Physics of Fluids*, 32(10).

Fan, G., Liu, Y., Zhao, W., and Wan, D. (2024). Effect of wall stress models and subgrid-scale models for flow past a cylinder at reynolds number 3900. *Physics of Fluids*, 36(1).

Fox, T. A. and West, G. (1993). Fluid-induced loading of cantilevered circular cylinders in a low-turbulence uniform flow. part 1: mean loading with aspect ratios in the range 4 to 30. *Journal of Fluids and Structures*, 7(1):1–14.

Franke, J. and Frank, W. (2002). Large eddy simulation of the flow past a circular cylinder at red= 3900. *Journal of wind engineering and industrial aerodynamics*, 90(10):1191–1206.

Fröhlich, J. and Rodi, W. (2004). Les of the flow around a circular cylinder of finite height. *International journal of heat and fluid flow*, 25(3):537–548.

Gopalan, H. and Jaiman, R. (2015). Numerical study of the flow interference between tandem cylinders employing non-linear hybrid urans–les methods. *Journal of Wind Engineering and Industrial Aerodynamics*, 142:111–129.

Gully, B. H., Webber, M. E., and Seepersad, C. C. (2010). A comparative analysis of wind propulsion systems for ocean-going vessels. In *ASME International Mechanical Engineering Congress and Exposition*, volume 44298, pages 1077–1085.

He, J. (1998). Approximate analytical solution of blasius' equation. *Communications in Nonlinear Science and Numerical Simulation*, 3(4):260–263.

Higuchi, H., Kim, H.-J., and Farell, C. (1989). On flow separation and reattachment around a circular cylinder at critical reynolds numbers. *Journal of Fluid Mechanics*, 200:149–171.

HRMM (n.d.). Sail freighter friday: Rotor ship buckau (1925). `https://www.hrmm.org/history-blog/sail-freighter-friday-rotor-ship-buckau-1925`, Accessed 2024-12-20.

Jester, W. and Kallinderis, Y. (2003). Numerical study of incompressible flow about fixed cylinder pairs. *journal of Fluids and Structures*, 17(4):561–577.

Jordan, S. A. and Ragab, S. A. (1998). A large-eddy simulation of the near wake of a circular cylinder. *Journal of Fluids Engineering*, 120(2):243–252.

Karabelas, S. (2010). Large eddy simulation of high-reynolds number flow past a rotating cylinder. *International journal of heat and fluid flow*, 31(4):518–527.

Karabelas, S., Koumroglou, B., Argyropoulos, C., and Markatos, N. (2012). High reynolds number turbulent flow past a rotating cylinder. *Applied mathematical modelling*, 36(1):379–398.

Kingma, D. P. and Ba, J. (2014). Adam: A method for stochastic optimization. *arXiv preprint arXiv:1412.6980*.

Kitagawa, T. and Ohta, H. (2008). Numerical investigation on flow around circular cylinders in tandem arrangement at a subcritical reynolds number. *Journal of Fluids and Structures*, 24(5):680–699.

Kourta, A., Boisson, H., Chassaing, P., and Minh, H. H. (1987). Nonlinear interaction and the transition to turbulence in the wake of a circular cylinder. *Journal of Fluid Mechanics*, 181:141–161.

Krajnović, S. (2011). Flow around a tall finite cylinder explored by large eddy simulation. *Journal of Fluid Mechanics*, 676:294–317.

Kravchenko, A. G. and Moin, P. (2000). Numerical studies of flow over a circular cylinder at re d= 3900. *Physics of fluids*, 12(2):403–417.

Kumar, S., Gonzalez, B., and Probst, O. (2011). Flow past two rotating cylinders. *Physics of Fluids*, 23(1).

Kume, K., Hamada, T., Kobayashi, H., and Yamanaka, S. (2022). Evaluation of aerodynamic characteristics of a ship with flettner rotors by wind tunnel tests and rans-based cfd. *Ocean Engineering*, 254:111345.

Kuroda, M. and Sugimoto, Y. (2022). Evaluation of ship performance in terms of shipping route and weather condition. *Ocean Engineering*, 254:111335.

Lam, K. M. (2009). Vortex shedding flow behind a slowly rotating circular cylinder. *Journal of Fluids and Structures*, 25(2):245–262.

Lee, S. and You, D. (2019). Data-driven prediction of unsteady flow over a circular cylinder using deep learning. *Journal of Fluid Mechanics*, 879:217–254.

Lehmkuhl, O., Rodríguez, I., Borrell, R., Chiva, J., and Oliva, A. (2014). Unsteady forces on a circular cylinder at critical reynolds numbers. *Physics of Fluids*, 26(12).

Li, H. and Sumner, D. (2009). Vortex shedding from two finite circular cylinders in a staggered configuration. *Journal of Fluids and Structures*, 25(3):479–505.

Li, S., Li, W., and Noack, B. R. (2022). Machine-learned control-oriented flow estimation for multi-actuator multi-sensor systems exemplified for the fluidic pinball. *Journal of Fluid Mechanics*, 952:A36.

Li, S., Yang, J., and He, X. (2024). Modeling transient flow dynamics around a bluff body using deep learning techniques. *Ocean Engineering*, 295:116880.

Lin, J.-C., Towfighi, J., and Rockwell, D. (1995). Instantaneous structure of the near-wake of a circular cylinder: on the effect of reynolds number. *Journal of Fluids and Structures*, 9(4):409–418.

Lindstad, E., Polić, D., Rialland, A., Sandaas, I., and Stokke, T. (2022). Decarbonizing bulk shipping combining ship design and alternative power. *Ocean Engineering*, 266:112798.

Liu, J., Ma, W., Jin, L., Liu, X., and Li, T. (2023). Experimental and numerical investigation on the wake flow and vortex shedding of a rotating circular cylinder. *Physics of Fluids*, 35(7).

Liu, Q. (2024). Wall-mounted circular cylinder flows. *Physics of Fluids*, 36(11).

Liu, Q., Gong, S., Lu, H., Tang, F., and Liang, Z. (2025). A computational fluid dynamics study of the impact of end effects on the magnus effect and wake transition in the flow around a circular rotating cylinder with two free ends. *Physics of Fluids*, 37(1).

Liu, Q., Gong, S., Lu, H., Xie, G., and Zuo, Z. (2024). Numerical investigation on the end effects of the flow past a finite rotating circular cylinder with two free ends. *Computers & Fluids*, 285:106475.

Lorente, L., Vega, J., and Velazquez, A. (2013). Efficient computation of the pod manifold containing the information required to generate a multi-parameter aerodynamic database. *Aerospace Science and Technology*, 25(1):152–160.

Luo, S., Gan, T., and Chew, Y. (1996). Uniform flow past one (or two in tandem) finite length circular cylinder (s). *Journal of wind engineering and industrial aerodynamics*, 59(1):69–93.

Ma, W., Liu, J., Jia, Y., Jin, L., and Ma, X. (2022). The aerodynamic forces and wake flow of a rotating circular cylinder under various flow regimes. *Journal of Wind Engineering and Industrial Aerodynamics*, 224:104977.

Ma, X., Karamanos, G.-S., and Karniadakis, G. (2000). Dynamics and low-dimensionality of a turbulent near wake. *Journal of fluid mechanics*, 410:29–65.

Maryami, R., Ali, S. A. S., Azarpeyvand, M., Dehghan, A. A., and Afshari, A. (2022). The influence of cylinders in tandem arrangement on unsteady aerodynamic loads. *Experimental Thermal and Fluid Science*, 139:110709.

Mason, J., Larkin, A., Bullock, S., van der Kolk, N., and Broderick, J. F. (2023). Quantifying voyage optimisation with wind propulsion for short-term co2 mitigation in shipping. *Ocean Engineering*, 289:116065.

Massaro, D., Karp, M., Jansson, N., Markidis, S., and Schlatter, P. (2024). Direct numerical simulation of the turbulent flow around a flettner rotor. *Scientific Reports*, 14(1):3004.

MetOffice (n.d.). Beaufort wind force scale. `https://www.metoffice.gov.uk/weather/guides/coast-and-sea/beaufort-scale`, Accessed 2025-01-05.

Min, G. and Jiang, N. (2024). Flow fields prediction for data-driven model of parallel twin cylinders based on pod-rbfnn and pod-bpnn surrogate models. *Annals of Nuclear Energy*, 199:110342.

Mittal, S., Kumar, V., and Raghuvanshi, A. (1997). Unsteady incompressible flows past two cylinders in tandem and staggered arrangements. *International journal for numerical methods in fluids*, 25(11):1315–1344.

Morton, C., Martinuzzi, R. J., Kindree, M., Shahroodi, M., and Saeedi, M. (2018). Wake dynamics of a cantilevered circular cylinder of aspect ratio 4. *International Journal of Heat and Fluid Flow*, 72:109–122.

Murata, T., Fukami, K., and Fukagata, K. (2020). Nonlinear mode decomposition with convolutional neural networks for fluid dynamics. *Journal of Fluid Mechanics*, 882:A13.

Norberg, C. (1994). An experimental investigation of the flow around a circular cylinder: influence of aspect ratio. *Journal of Fluid Mechanics*, 258:287–316.

Norsepower (n.d.). Norsepower. `https://www.norsepower.com/`, Accessed: 2024-12-20.

Ong, L. and Wallace, J. (1996). The velocity field of the turbulent very near wake of a circular cylinder. *Experiments in fluids*, 20(6):441–453.

Padrino, J. and Joseph, D. (2006). Numerical study of the steady-state uniform flow past a rotating cylinder. *Journal of fluid mechanics*, 557:191–223.

Palau-Salvador, G., Stoesser, T., and Rodi, W. (2008). Les of the flow around two cylinders in tandem. *Journal of Fluids and Structures*, 24(8):1304–1312.

Park, C.-W. and Lee, S.-J. (2000). Free end effects on the near wake flow structure behind a finite circular cylinder. *Journal of Wind Engineering and Industrial Aerodynamics*, 88(2-3):231–246.

Parker, C. M. and Leftwich, M. C. (2016). The effect of tip speed ratio on a vertical axis wind turbine at high reynolds numbers. *Experiments in Fluids*, 57:1–11.

Ping, H., Zhu, H., Zhang, K., Wang, R., Zhou, D., Bao, Y., and Han, Z. (2020). Wake dynamics behind a rotary oscillating cylinder analyzed with proper orthogonal decomposition. *Ocean Engineering*, 218:108185.

Prasad, A. and Williamson, C. H. (1997). The instability of the shear layer separating from a bluff body. *Journal of fluid mechanics*, 333:375–402.

Prsic, M. A., Ong, M. C., Pettersen, B., and Myrhaug, D. (2014). Large eddy simulations of flow around a smooth circular cylinder in a uniform current in the subcritical flow regime. *Ocean engineering*, 77:61–73.

Rastan, M., Sohankar, A., and Alam, M. M. (2021). Flow and heat transfer across two inline rotating cylinders: Effects of blockage, gap spacing, reynolds number, and rotation direction. *International Journal of Heat and Mass Transfer*, 174:121324.

Renganathan, S. A., Maulik, R., and Rao, V. (2020). Machine learning for nonintrusive model order reduction of the parametric inviscid transonic flow past an airfoil. *Physics of Fluids*, 32(4).

Roshko, A. (1961). Experiments on the flow past a circular cylinder at very high reynolds number. *Journal of fluid mechanics*, 10(3):345–356.

Rostamy, N., Sumner, D., Bergstrom, D., and Bugg, J. (2012). Local flow field of a surface-mounted finite circular cylinder. *Journal of Fluids and Structures*, 34:105–122.

Sahebzadeh, S., Rezaeiha, A., and Montazeri, H. (2022). Vertical-axis wind-turbine farm design: Impact of rotor setting and relative arrangement on aerodynamic performance of double rotor arrays. *Energy Reports*, 8:5793–5819.

Schewe, G. and Jacobs, M. (2019). Experiments on the flow around two tandem circular cylinders from sub-up to transcritical reynolds numbers. *Journal of Fluids and Structures*, 88:148–166.

Seddiek, I. S. and Ammar, N. R. (2021). Harnessing wind energy on merchant ships: case study flettner rotors onboard bulk carriers. *Environmental Science and Pollution Research*, 28:32695–32707.

Shehata, H. M. and Medina, A. (2021). The wake structure of a stationary and a rotary wall-mounted low-aspect-ratio cylinder. *AIAA Journal*, 59(12):4815–4823.

Shehata, H. M. and Medina, A. (2022). On the flow dynamics of wall-mounted low-aspect-ratio rotating cylinders. *Physics of Fluids*, 34(12).

Siddiqui, M. A., Munir, A., Ali, M. H., Zhao, M., Duan, P., and Qadri, M. N. M. (2024). Numerical study of wake flow across two circular cylinders in tandem arrangement with high rotation speed. *Physics of Fluids*, 36(12).

Sirovich, L. (1987). Turbulence and the dynamics of coherent structures. i–iii. *Quarterly of Applied Mathematics*, 45(3):561–590.

Stankiewicz, W. (2022). Recursive dynamic mode decomposition for the flow around two square cylinders in tandem configuration. *Journal of Fluids and Structures*, 110:103515.

Stringer, R., Zang, J., and Hillis, A. (2014). Unsteady rans computations of flow around a circular cylinder for a wide range of reynolds numbers. *Ocean Engineering*, 87:1–9.

Sumner, D., Heseltine, J., and Dansereau, O. (2004). Wake structure of a finite circular cylinder of small aspect ratio. *Experiments in Fluids*, 37:720–730.

Sumner, D., Rostamy, N., Bergstrom, D., and Bugg, J. (2015). Influence of aspect ratio on the flow above the free end of a surface-mounted finite cylinder. *International Journal of Heat and Fluid Flow*, 56:290–304.

Taira, K., Brunton, S. L., Dawson, S. T., Rowley, C. W., Colonius, T., McKeon, B. J., Schmidt, O. T., Gordeyev, S., Theofilis, V., and Ukeiley, L. S. (2017). Modal analysis of fluid flows: An overview. *AIAA journal*, 55(12):4013–4041.

Taira, K., Hemati, M. S., Brunton, S. L., Sun, Y., Duraisamy, K., Bagheri, S., Dawson, S. T., and Yeh, C.-A. (2020). Modal analysis of fluid flows: Applications and outlook. *AIAA journal*, 58(3):998–1022.

Talluri, L., Nalianda, D., and Giuliani, E. (2018). Techno economic and environmental assessment of flettner rotors for marine propulsion. *Ocean engineering*, 154:1–15.

Thouault, N., Breitsamter, C., Adams, N. A., Seifert, J., Badalamenti, C., and Prince, S. A. (2012). Numerical analysis of a rotating cylinder with spanwise disks. *AIAA journal*, 50(2):271–283.

Tillig, F. and Ringsberg, J. W. (2020). Design, operation and analysis of wind-assisted cargo ships. *Ocean engineering*, 211:107603.

Tsutsui, T. (2012). Experimental study on the instantaneous fluid force acting on two circular cylinders closely arranged in tandem. *Journal of wind engineering and industrial aerodynamics*, 109:46–54.

UoS (n.d.). History of flettner rotors. `https://www.esru.strath.ac.uk/EandE/Web_sites/18-19/Flettner/strathflettner.wixsite.com/flettnerrotor/history-of-flettner-rotors.html`, Accessed: 2024-12-20.

Uzun, A. and Hussaini, M. Y. (2012). An application of delayed detached eddy simulation to tandem cylinder flow field prediction. *Computers & Fluids*, 60:71–85.

VesselFinder (n.d.). Eship-1. `https://www.vesselfinder.com/vessels/details/9417141`, Accessed 2025-01-04.

Wang, H., Cao, H., and Zhou, Y. (2014). Pod analysis of a finite-length cylinder near wake. *Experiments in fluids*, 55:1–15.

Wei, T. and Smith, C. (1986). Secondary vortices in the wake of circular cylinders. *Journal of Fluid Mechanics*, 169:513–533.

West, G. and Apelt, C. (1982). The effects of tunnel blockage and aspect ratio on the mean flow past a circular cylinder with reynolds numbers between 104 and 105. *Journal of Fluid mechanics*, 114:361–377.

West, G. and Apelt, C. (1993). Measurements of fluctuating pressures and forces on a circular cylinder in the reynolds number range 104 to 2 · 5× 105. *Journal of fluids and structures*, 7(3):227–244.

Weymouth, G. D. and Font, B. (2025). Waterlily. jl: A differentiable and backend-agnostic julia solver for incompressible viscous flow around dynamic bodies. *Computer Physics Communications*, page 109748.

Weymouth, G. D. and Lauber, M. (2024). Using biot-savart boundary conditions for unbounded external flow on eulerian meshes. *arXiv preprint arXiv:2404.09034*.

Woyciekoski, M. L., Endres, L. A. M., de Paula, A. V., and Möller, S. V. (2020). Influence of the free end flow on the bistability phenomenon after two side by side finite height cylinders with aspect ratios of 3 and 4 and high blockage. *Ocean Engineering*, 195:106658.

Wu, G., Du, X., and Wang, Y. (2020). Les of flow around two staggered circular cylinders at a high subcritical reynolds number of 1.4× 105. *Journal of Wind Engineering and Industrial Aerodynamics*, 196:104044.

Wu, X., Zhang, W., Peng, X., and Wang, Z. (2019). Benchmark aerodynamic shape optimization with the pod-based cst airfoil parametric method. *Aerospace Science and Technology*, 84:632–640.

Xu, G. and Zhou, Y. (2004). Strouhal numbers in the wake of two inline cylinders. *Experiments in Fluids*, 37:248–256.

Xu, Y., Sha, Y., Wang, C., Cao, W., and Wei, Y. (2023). Comparative studies of predictive models for unsteady flow fields based on deep learning and proper orthogonal decomposition. *Ocean Engineering*, 272:113935.

Yousif, M. Z. and Lim, H. (2021). Improved delayed detached-eddy simulation and proper orthogonal decomposition analysis of turbulent wake behind a wall-mounted square cylinder. *AIP Advances*, 11(4).

Yousif, M. Z. and Lim, H.-C. (2022). Reduced-order modeling for turbulent wake of a finite wall-mounted square cylinder based on artificial neural network. *Physics of Fluids*, 34(1).

Zhang, H. and Melbourne, W. (1992). Interference between two circular cylinders in tandem in turbulent flow. *Journal of Wind Engineering and Industrial Aerodynamics*, 41(1-3):589–600.